



**HAL**  
open science

# Study on nonlinear multi-dimensional direct laser writing by using ultrashort high power laser

Chang-Hyun Park

► **To cite this version:**

Chang-Hyun Park. Study on nonlinear multi-dimensional direct laser writing by using ultrashort high power laser. Physics [physics]. Université de Bordeaux; Yonse Taehakkyo, 2020. English. NNT : 2020BORD0046 . tel-02945362

**HAL Id: tel-02945362**

**<https://theses.hal.science/tel-02945362>**

Submitted on 22 Sep 2020

**HAL** is a multi-disciplinary open access archive for the deposit and dissemination of scientific research documents, whether they are published or not. The documents may come from teaching and research institutions in France or abroad, or from public or private research centers.

L'archive ouverte pluridisciplinaire **HAL**, est destinée au dépôt et à la diffusion de documents scientifiques de niveau recherche, publiés ou non, émanant des établissements d'enseignement et de recherche français ou étrangers, des laboratoires publics ou privés.

**THÈSE EN COTUTELLE PRÉSENTÉE**

**POUR OBTENIR LE GRADE DE**

**DOCTEUR DE L'UNIVERSITÉ DE BORDEAUX**

**ET DE L'UNIVERSITÉ DE YONSEI**

**ÉCOLE DOCTORALE DES SCIENCES PHYSIQUES ET DE L'INGÉNIEUR**

**SPÉCIALITÉ: LASERS, MATIÈRE ET NANOSCIENCES**

Par Chang-Hyun PARK

**Study on Nonlinear Multi-dimensional  
Direct Laser Writing by using Ultrashort High Power Laser**

Sous la direction de Lionel CANIONI et de Seung-Han PARK

Soutenue le 8 Juin 2020

Membres du jury :

M. SHIN, Dong-Soo, Professeur à l'Université de Hanyang (Président, Rapporteur)

M. JANG, Joon Ik, Professeur à l'Université de Sogang (Rapporteur)

M. PARK, Seung-Han, Professeur à l'Université de Yonsei (Co-Directeur)

M. CANIONI, Lionel, Professeur à l'Université de Bordeaux (Directeur)

M. PETIT, Yannick, Professeur à l'Université de Bordeaux (Invité)



# Table of Contents

Acknowledgment.....	vii
감사의 글(Acknowledgment in Korean).....	ix
Abstract.....	xiii
List of Figures.....	xvii
List of Tables.....	xxiii
Chapter 1. Introduction.....	1
1.1 Direct Laser Writing with ultrashort pulse lasers.....	1
1.2 Applications using direct laser writing .....	2
1.3 The scope of this manuscript .....	4
Chapter 2. Direct Laser Writing Experimental System .....	8
2.1 Interaction between fs pulse Laser and Materials .....	8
2.2 Silver-containing glass sample.....	1 0
2.2.1 General formation process for metallic cluster .....	1 0
2.2.2 The formation process for Silver-doped Zinc Phosphate glasses ...	1 1
2.2.3 Modeling for cluster formation of metallic cluster .....	1 4
2.2.4 Optical properties of silver containing glass.....	2 5
2.3 Experimental set-up: fs-Laser, AOM and SLM .....	3 0
2.3.1 femtosecond laser and Experimental set-up.....	3 0
2.3.2 Acousto-Optic Modulator .....	3 1
2.3.3 Spatial Light Modulator.....	3 2

Chapter 3. 1-dimensional DLW and its spatial redistribution of Silver species	3 5
3.1 Introduction .....	3 5
3.2 Experimental Methods: used glass sample, laser irradiance, and analyses .....	3 6
3.3 NSOM Results and discussion .....	3 8
3.4 Simulation and result .....	4 1
3.5 Conclusion .....	4 5
Chapter 4. 2-dimensional DLW and application .....	4 8
4.1 Introduction .....	4 8
4.2 Experimental Methods .....	5 0
4.2.1 Type A DLW for waveguide .....	5 0
4.2.2 Preparation of samples .....	5 3
4.2.3 Fabrication of Y-junction .....	5 3
4.2.4 Measurement of output and optical path difference .....	5 6
4.3 Result and discussion .....	5 7
4.3.1 Symmetric Y-junction .....	5 7
4.3.2 Asymmetric Y-junction .....	5 9
4.3.3 Modified asymmetric Y-junction .....	6 4
4.3.4 Near field injection with NSOM fiber tip .....	6 7
4.4 Conclusion .....	6 9
Chapter 5. 5-dimensional Optical Data Storage .....	7 1

5.1 Introduction.....	7 1
5.2 Experimental Methods .....	7 7
5.2.1 Preparation of sample .....	7 7
5.2.2 First parameter for expansion of dimension: orientation of ellipse...	7 7
5.2.3 Second parameter for expansion of dimension: Intensity of fluorescence.....	8 2
5.2.4 Fluorescence calibration matrix with 16 intensity levels and 16 orientations of ellipse.....	8 5
5. 3 Outline of writing and reading process of optical data storage using two additional parameters with type A DLW .....	8 6
5. 4 Writing process with 256 levels: 16 levels for fluorescence intensity and 16 levels for orientation of elliptical pattern .....	8 8
5. 5 Reading process with 256 levels: 16 levels for fluorescence intensity and 16 levels for orientation of ellipse.....	9 1
5. 6 Reading process with 64 levels: 8 levels for fluorescence intensity and 8 levels for orientation of ellipse.....	105
5. 7 Calculation for optical data storage density.....	114
5. 8 Conclusion.....	116
Chapter 6. Conclusion.....	119
Bibliography .....	123
Résumé.....	131
국 문 요 약 (Abstract in Korean) .....	135



## Acknowledgment

As I stood at the end of the short and long Ph.D. course and looked back at the time of the past 7 years and 6 months, I seemed unable to express all my gratitude for the grace I received. I would like to take this opportunity to express my sincere gratitude.

I sincerely appreciate Prof. PARK accepting me as a disciple in 2013 and for direct and indirect teaching of human aspects, researcher attitude, member roles, and leader qualities. During my Ph.D. the teaching I learned from my professor has not only stayed at that time, but has also been exercised in society, which is driving many seniors, colleagues, and juniors, including myself, to faithfully fulfill their roles in their respective positions. I think, I have a selfish wish for him to be healthy for a long time and to continue this teaching. And it was great opportunity to collaborate with Bordeaux University in France, so I could take a broader view of the world. I will continue to learn and learn the wisdom of life I learned during my master's and doctorate degrees and do my best to fulfill my role as a person.

Starting a co-degree in France, there were many difficulties, including language. I would like to thank Professor Yannick PETIT and Professor Lionel CANIONI for their help. Thank you for your consideration not only in research but also in the extent of the life of a student studying abroad. And I want to thank Professor Inka of SLAM, Professor Bruno, Arthur, Wende, Alain, Delphine, Julian, Laura, Joyce, Sophie and Theo, Thierry of ICMCB for filling up life in Bordeaux. Experiences in Bordeaux will be an unforgettable memory for me.

I also thank my seniors, colleagues, and juniors who have been the most precious and supportive people I've ever met in the lab. We were able to rely on each other at a time when we were wandering about the future, and we were greatly helped by a lot of learning.

I would like to my sincere gratitude to Jae-hyuk KIM, Ga-young KIM, Dae-gyu KIM, Eung-jang LEE, Eun-hee JUNG, Kyung-seok KIM, Jin-myeong MOK, Hong-gyu AHN, Bo-ram KIM, and Sung-ho LEE. During my master's and doctoral programs, my seniors' appearances and roles became a standard for me in order to be a decent junior and a better senior. And I also thank Daeyeon KIM and Young Eun LEE who are my 13th graders. The time I shared with you in Anam and Sinchon was a big help to me. And I'd like to thank Yu-mi JUNG, Young-min KEE, Beom-jun JANG, Si-young NO, Jong-hyun PARK, Gyu-ri BAE, Sang-min LEE, Seong-hyun JEON, Seung-hyun LEE, Woo-young JUNG, Seok-hyun KIM, Joo-eon PARK, Jeong-gu JI, In-joon SEO, Beom-jin KIM, Sang-mook LEE, Young-hwan CHOI, Byeong-yun HAN, Jeong-Woo KIM, Dong-wook SHIN, Jun-hyeong KIM, Chan-su AHN, Ha-rim JEONG, Seong-jae JIN, Yeong-hwan JIN. And I thank Sung-hee HWANG, Sun-young LEE, Eun-ji IM, and Hye-sun LEE for always helping us and taking care of us.

Lastly, I want to thank my parents and younger brothers for unsparing support and encouragement during my university life. Although there were ordeals and difficulties, both big and small, I was able to finish my degree safely thanks to constant faith and encouragement.

In order to reciprocate the grace and faith I have received, I will try to do my best as a disciple, junior, fellow, senior, and family. Again, I express my great gratitude.

April 2020

## 감사의 글(Acknowledgment in Korean)

짧고도 길었던 박사과정의 마무리에 우두커니 서서 지난 7년 6개월의 시간을 무심히 돌이켜 보니, 제가 받은 은혜에 대해 감사함을 모두 표현하지 못한 것 같습니다. 이 기회를 빌려 진심 어린 감사함을 표현하고자 합니다.

2013년 저를 제자로 받아주시고, 인간적인 면, 연구자의 자세, 구성원의 역할, 리더의 자질 등을 직·간접적으로 가르쳐 주신 박승한 교수님께 가장 먼저 감사의 말씀을 전합니다. 연구실 생활을 하는 동안 교수님께 배운 가르침이 그 시간에만 머물지 않고 사회에서도 발휘되어, 저를 포함한 많은 선배님, 동료들, 후배들이 각자의 위치에서 훌륭히 본인의 역할을 충실히 해내는 원동력이 되고 있다 생각합니다. 부디 오랫동안 건강하시어 이러한 가르침이 지속되었으면 하는 이기적인 바람을 가져봅니다. 또한 저게 프랑스의 보르도 대학과 공동학위를 할 수 있는 기회를 주셔서, 제가 세상을 좀 더 넓게 볼 수 있는 계기가 될 수 있었습니다. 석·박사 학위 기간 동안 배운 삶의 지혜를 꾸준히 익히고 체득하여 한 사람으로써의 몫을 다 할 수 있도록 최선을 다하는 모습을 보여드리겠습니다.

프랑스에서 공동학위를 시작하며 언어를 포함한 어려운 점이 많았습니다. 이에 본인의 일처럼 도와준 Yannick PETIT 교수님과 Lionel CANIONI 교수님께 감사의 말씀을 전합니다. 또한 연구뿐만 아니라 유학생의 삶의 영위하는 범위에서도 섬세한 배려해 주셔서 감사합니다. 그리고 보르도에서의 삶을 더욱 풍성하게 채워준 SLAM의 Inka 교수님, Bruno 교수님, Arthur, Wende, Alain, Delphine, Julian, Laura, Joyce,

Sophie 그리고 ICMCB의 Theo, Thierry 교수님께 감사한 마음을 전합니다.  
보르도에서의 생활은 제게 잊지 못할 소중한 기억이 될 것입니다.

또한 연구실에서 만난 가장 소중하고 힘이 되어준 여러 선배님, 동기, 그리고 후배들에게 감사함을 전합니다. 미래에 대한 불안과 고민으로 방향을 하던 시기에 만나 서로 의지할 수 있었고, 많은 배움으로 큰 도움을 받았습니다. 김재혁, 김가영, 김대규, 이용장, 정은희, 김경석, 목진명, 안홍규, 김보람, 이성호 선배님들께 감사한 마음을 전합니다. 연구실에서 가장 저학기였던 제가 졸업을 앞 둔 최고 학기가 되는 동안, 부끄럽지 않은 후배, 더 좋은 선배가 되기 위해 선배님들의 모습과 역할이 제게는 하나의 기준이 되었습니다. 그리고 13학번 동기인 대연이와 영은이 형에게도 감사의 마음을 전합니다. 안암과 신촌에서 나누었던 시간은 제게 큰 힘이 되었습니다. 그리고 저를 많이 도와주고 따라와준 물리학과 후배 정유미, 기영민, 장범준, 노시영, 박종현, 배규리, 이상민, 전성현, 광과학공학과 후배 이승현, 정우영, 김석현, 박주언, 지정구, 서인준, 김범진, 이상목, 최영환, 한병윤, 김기환, 종우형, 신동욱 선임님, 정하림, 진영환, 진성재, 안찬수, 김준형에게 감사함을 전합니다. 함께 시간을 보내주어 함께 있어주어, 든든했고, 든든하고, 든든할 것입니다. 그리고 곁에서 항상 저희를 도와주시고 챙겨주신 황성희, 이선영, 임은지, 이해선 선생님들께 감사한 마음을 전합니다.

마지막으로 15년의 긴 학생 생활을 할 수 있게 지원과 사랑을 아끼지 않으신 부모님과 응원과 격려를 해준 동생에게 감사합니다. 크고 작은 시련과 어려움이 있었지만, 끊임없는 믿음과 격려를 주신 덕분에 학위를 무사히 마칠 수 있었습니다.

제가 받은 은혜와 믿음에 보답하기 위해 제자로, 후배로, 동료로, 선배로, 가족으로써 도리를 다 할 수 있도록 노력하겠습니다. 다시 한 번 큰 감사한 마음을 표현합니다.

2020년 4월



## **Abstract**

In the past 30 years as the pulse width of lasers has been narrowed and high-power lasers have been developed, researches on the interaction between photon and materials using femtosecond lasers have been actively conducted. The high energy density of femtosecond pulsed lasers enables nonlinear photoionization processes in several ways. This paper reports a study of a type Argentum direct laser writing in silver containing zinc phosphate glasses by inducing a nonlinear absorption deformation of femtosecond laser pulses. When silver-containing zinc phosphate glasses are irradiated with femtosecond laser pulses, ring-shaped clusters are formed due to non-linear absorption. The fluorescence properties and the refractive index of the silver cluster induced by this deformation are different from those of the original zinc phosphate glass.

Simultaneous comparisons of chemical micro probes, near-field scanning optical microscopy (NSOM), and numerical modeling were used to analyze the laser-induced silver species distribution. The results significantly strengthen the understanding of material modifications in such glasses in a non-thermal interaction regime. In particular, it has been found that the spatial distribution of species in silver-containing glasses produced by femtosecond laser irradiation has a significant effect on chemical etching selectivity.

The Y-shaped beam splitters, 2D structures made by using type A DLW, was fabricated and its performance was measured. It was confirmed that a waveguide of a general shape in which the refractive index of the core is larger than that of cladding can be produced by using a type A DLW. Since the type A DLW always induces positive refractive index changes

from  $2.7 \times 10^{-3}$  to  $5.1 \times 10^{-3}$ , it is very suitable for making waveguide. A symmetric Y-junction and various asymmetric Y-junctions were also designed and fabricated using double line waveguides. Their output ratios were measured according to the transition of the inject position. It was confirmed that the output ratio could be varied from 96%-4% to 57%-43% due to the different irradiance in the process of writing between the upper branch and lower branch. So DLW in silver containing zinc phosphate glasses can be utilized easily and quickly to fabricate the desired type of optical device with only the writing process.

Finally, the scope of application was further expanded by investigating 5D optical data storage (ODS) using type A DLW. We have demonstrated 5D optical data storage encoded in orientated type A DLW modifications by using a relatively low laser irradiance compared to conventional DLW. Five dimensions were achieved by adding the orientation of ellipse pattern and fluorescence intensity to 3D position. The ellipse pattern was created by anamorphic focusing, and the orientation was adjusted to 16 levels by employing SLM. In addition, AOM device was used to adjust the femtosecond laser intensity of 16 levels.

To confirm the possibility of the proposed 5D ODS, two different images were simultaneously embedded simultaneously in one image by type A DLW. And it was demonstrated that the two different original images of 4-bit bitmap format were successfully restored. The corresponding reading fidelities of 60.5% and 25.1% were obtained for the orientation direction and fluorescence intensity levels, respectively. In addition, it is shown that the reading accuracy can be greatly improved to 85.0% and 47.1% when 3-bit bitmap format was applied. Using the proposed this technology, we showed a maximum data

density of  $14.9 \text{ Gb/cm}^3$  can be achieved, and it can reach up to  $119.2 \text{ Gb/cm}^3$  (using  $\text{NA} = 1.3$  oil target).

In conclusion, the fluorescence characteristics of type A DLW in silver containing zinc phosphate glasses were studied, and its utility as a multi-dimension application was confirmed. We believe this technology has great potential for nano-scale patterning in semiconductor and fabrication of micro-scale optical devices.

Key words: Direct Laser Writing (DLW), Femtosecond Laser, Type A DLW, Waveguide, 5D Optical Data Storage (ODS), Laser Patterning, and Laser Lithography



## List of Figures

Figure 1. Various applications using direct laser writing .....	4
Figure 2 Time scale of the interaction between photon and material [28] .....	9
Figure 3 The process and results of interaction of fs laser pulse and transparent materials : (1) high laser irradiance at focal volume in transparent material; (2) process of energy deposition by multiphoton absorption and avalanche ionization; (3) process of energy transfer and thermalization; (4) result of material relaxation and permanent modification by melting, nano-grating, and micro-explosion [29].....	1 0
Figure 4 The process for formation of laser-induced ring shape cluster within the silver- doped phosphate glasses [38] .....	1 4
Figure 5 Classification of modifications according to laser flux and types of refractive index change [41] .....	2 5
Figure 6 Configurations of type argenteum modification with stationary focus (a) and in the same plane (g). Fluorescence images of writing pattern in the front and side view (b, e). Images obtained by High Reflection Scanning Electron Microscopy(HRSEM) (c, f). [42] .....	2 6
Figure 7 Comparison of refractive index changes between type I and type A [41] .....	2 7
Figure 8 Fluorescence properties of silver-containing phosphate glass (a) Fluorescence image of structures engraved on glasses sample with three different chemical composition, (b) Fluorescence intensity according to writing velocity, (c) Spectrum distribution of emitted light when excited with a laser of 405 nm wavelength [28].	2 8
Figure 9 Refractive index change for laser irradiance and number of pulses; (a) matrix of structures for 2 parameter changes; (b) Image showing optical path difference for one structure; (c) Graph showing refractive index change for two parameters change [43] .....	2 9
Figure 10 Experimental Setup Schematic for Direct Laser Writing; fs laser, Acousto-Optic Modulator, Spatial Light Modulator, and XYZ stage.....	3 0
Figure 11 Graph showing the relationship between voltage to both fused silica and laser power at m=0 order.....	3 1

Figure 12 IGOR Program, which is designed to control SLM mask, enables several modes of focusing and precisely adjust the positioning of the laser beam. ....	3 3
Figure 13 (a) White light image of 1D DLW patterns sample after etching process; (b, c) Images obtained by CMOS camera after injection of 405 nm and 632.8 nm laser beam with objective lens. ....	3 7
Figure 14 Experimental set-up of Near-field Scanning Optical Microscope in illumination mode, with light injection from a tapered optical fiber probe tip (100 nm aperture). 2 laser sources, objective lenses (focusing (20x, 0.40NA) and imaging (40x, 0.60NA)), long pass filter, and single channel photomultiplier detector (PMT). ....	3 8
Figure 15 (a, d) Image of surface topology obtained from NSOM in illumination mode; (b, e) Image of near field optical signal obtained by NSOM when the silver species are excited by 405 nm laser diode and 632.8 nm He-Ne laser; (c, f) Associated line profiles through center of ring-shape silver cluster.....	3 9
Figure 16 Numerical modeling of the laser-induced redistribution of silver species (8.8 TW/cm <sup>2</sup> , N <sub>pulse</sub> = 200 or 1400), showing the profiles of the silver ions (black line), the induced silver cluster and hole centers (green line), and all of silver species (red line). ....	4 2
Figure 17 (a) Experimental topological profile (blue curve) and simulated etching-induced topological profile (red curve) adjusted by optimizing the normalized etching rate distribution (green curve). (b) Silver element distribution by micro-probe measurement (blue curve, from [9]) and NSOM measurement (red curve, from Figure 16 (d)) with respect to the optimized normalized etching rate distribution (green curve). ....	4 4
Figure 18. Fabrication of optical splitter/coupler. (a) The fused biconical taper process with optical fiber; (b) The fabrication process of the optical beam splitters by casting method .....	4 9
Figure 19. Schematic for optical device fabrication through Direct Laser Writing (DLW) .....	4 9
Figure 20. (a) Schematic image showing 2D structure fabrication with type A modification; (b) Top and side view of fabricated 2D structure [38] .....	5 1
Figure 21. (a) Type I waveguide and (b) type A waveguide. (1) The image of Top/Side view of DLW pattern for both type. Various Optical path differences profiles for two types as a function of (2) laser pulse energy and (3) writing speed.....	5 2
Figure 22. Experimental/theoretical relationships between (a) the radius of Ag <sub>2</sub> <sup>+</sup> ring structure and number of pulses/laser irradiance, (b) refractive index change and	

number of pulses/laser irradiance.....	5 3
Figure 23. Structure schematic of Y-junction.; $l$ : total length of Y-junction, $l_1$ : The length from the input to the point where it is divided into two branches, $l_2$ , $l_3$ : Length of curved part with curvature of 150mm, and $l_4$ : Length from the end of the curve to the output..	5 5
Figure 24. Experimental setup to measure the output of the Y-junction .....	5 6
Figure 25. Output image and profile line of symmetric Y-junction.....	5 7
Figure 26. (a) A white light image of the input of a waveguide made of Type A DLW; (b) the relationship between injection position with 200 nm interval and total power; (c) variation of output ratio for injection position .....	5 9
Figure 27. Shape of asymmetric Y-junction and applied irradiance for each branch.....	6 0
Figure 28. (a) Changes of output ratios of lower branch according to injection position for different asymmetric Y-junctions; (b) Output profiles and output ratios for one symmetric and four asymmetric beam splitter, when injection position = 0.....	6 1
Figure 29. Index changes and profiles for one symmetric Y-junction and four asymmetric Y-junctions .....	6 3
Figure 30. Shape of modified asymmetric Y-junction and applied irradiance for each branch. ....	6 4
Figure 31. (a) Changes of output ratios of lower branch according to injection position for four modified asymmetric Y-junctions; (b) Output profiles and output ratios for four modified asymmetric beam splitter, when injection position = 0.....	6 6
Figure 32. (a) Schematic showing beam injection into waveguide using NSOM probe tip; (b, c) output ratio result when the objective lens and the NSOM probe tip is used to put incident beam in the symmetric Y-junction; (d, e) output ratio result when the objective lens and the NSOM probe tip is used to put incident beam in the asymmetric Y-junction. ....	6 8
Figure 33. Historical evolution of the information recording in human society.....	7 1
Figure 34 Comparison of features of four ODS mediums; CD, DVD, HD DVD, and Blu-ray .....	7 2
Figure 35. (a) Holographic Versatile Disc(HVD); (b) Schematic showing how HVD uses two laser beams to store information; (c) Digital Multilayer Disk(DMD); (d) Cross section of DMD layers recorded in a 3D disc .....	7 3

Figure 36. Experimental results of Min Gu's group using different wavelength laser beam and polarization.....	7 4
Figure 37. Experimental results from Kazansky's group implementing 5 dimensional ODS by adding orientation of nano-gratings and retardance by using type II DLW	7 5
Figure 38. Femtosecond laser tightly focused in the silver containing glass, resulting in subsequent production of fluorescent silver clusters at its periphery. ....	7 8
Figure 39. Variation of SLM mask and DLW patterns according to the manipulation of coefficient of tangential focusing.....	7 9
Figure 40. Variations of eccentricity(a) and fluorescence intensity(b) of ellipse-shape DLW pattern according to tangential focusing coefficient.....	8 0
Figure 41. Images of orientation change of elliptical patterns obtained by SLM phase mask manipulation, corresponding to $2^4 = 16$ orientation-encoded digital levels. ....	8 1
Figure 42. Fluorescent silver cluster distributions for several depths with respect to the tangential focal plane, respectively corresponding to circular or elliptical fluorescent shapes (confocal microscope imaging (20x, NA = 0.75) with excitation at 405 nm), for symmetrical or anamorphic focusing conditions. ....	8 2
Figure 43. Fluorescence intensity change(a) and retrieving result of ellipse orientation(b) according to voltage applied to AOM .....	8 3
Figure 44. Relation between intensity level and fluorescence intensity (a, c) when voltage intervals from 0.6V to 0.8V are divided equally and (b, d) When optimized by dividing fluorescence intensity interval equally .....	8 4
Figure 45. Measured fluorescence intensity versus incident laser irradiance, to calibrate the 5D decoding process. The inset image shows a fabricated matrix with 16 intensity levels and 16 orientations in the silver-containing glass.....	8 6
Figure 46. Flow map showing how intensity part and orientation part are utilized in writing/reading process of 5D optical data storage.....	8 8
Figure 47. (a) and (b) are the original images of two Nobel laureates encoded in 16 grey-scale levels; (c) is the DLW entangled image by independently addressing the 16 orientation levels of (a) and the 16 irradiance levels of (b); (d) Fluorescence calibration matrix observed by confocal microscopy to retrieve intensity-orientation correlations and to provide the dedicated correction for subsequent fluorescence intensity reading (excitation at 405 nm). ....	9 0

Figure 48. (a) Retrieved image from the initial image in Figure 47(a); (b) Retrieved image from the initial image in Figure 47(b); (c) Level difference between Figure 47(a) and 16(a); (d) Level difference between Figure 47(b) and 16(b); (e) Histogram of the level difference between original and decoded levels for the orientation direction; (f) Histogram of the level difference between original and decoded levels for the fluorescence intensity.....	9 4
Figure 49. Histogram of retrieving results for each orientation level of orientation decoding; 0°, 11.25°, 22.5°, and 33.75° .....	96
Figure 50. Histogram of retrieving results for each orientation level of orientation decoding; 45°, 56.25°, 67.5°, and 78.75° .....	97
Figure 51. Histogram of retrieving results for each orientation level of orientation decoding; 90°, 101.25°, 112.5°, and 123.75° .....	98
Figure 52. Histogram of retrieving results for each orientation level of orientation decoding; 135°, 146.25°, 157.5°, and 168.75° .....	99
Figure 53. Histogram of retrieving results for each intensity level of intensity decoding; 1, 2, 3, and 4 .....	101
Figure 54. Histogram of retrieving results for each intensity level of intensity decoding; 5, 6, 7, and 8 .....	102
Figure 55. Histogram of retrieving results for each intensity level of intensity decoding; 9, 10, 11, and 12 .....	103
Figure 56. Histogram of retrieving results for each intensity level of intensity decoding; 13, 14, 15, and 16 .....	104
Figure 57. (a) Retrieved image from the initial image in Figure 47(a); (b) Retrieved image from the initial image in Figure 47(b); (c) Level difference between Figure 47(a) and 25(a); (d) Level difference between Figure 47(b) and 25(b); (e) Histogram of the level difference between original and decoded levels for the orientation direction; (f) Histogram of the level difference between original and decoded levels for the fluorescence intensity.....	106
Figure 58. Histogram of retrieving results for each orientation level of orientation downgrade-decoding; 0°, 22.5°, 45°, and 67.5° .....	109
Figure 59. Histogram of retrieving results for each orientation level of orientation downgrade-decoding; 90°, 112.5°, 135°, and 157.5° .....	110
Figure 60. Histogram of retrieving results for each intensity level of intensity downgrade-decoding; 1, 2, 3, and 4 .....	112
Figure 61. Histogram of retrieving results for each intensity level of intensity downgrade-decoding; 5, 6, 7, and 8 .....	113
Figure 62. (a) An image of unit pattern fabricated by using type A DLW; (b) the profile of	

fluorescence intensity along the y-axis (short axis of ellipse); (c) the profile of fluorescence intensity along the x-axis (long axis of ellipse); (d) the profile of fluorescence intensity and Gaussian fitting along the z-axis(depth) at  $z = 0$  focal plane ..... 114

Figure 63. Royon's experimental data written at 20  $\mu\text{m}$  intervals between layers to overcome crosstalk [76]. ..... 115

## List of Tables

Table 1 The SLM mask which control the phase of laser beam and the DLW patterns in the silver containing glass for different modes of focusing. ....	3 3
Table 2. The relation between voltage applied to the AOM and Irradiance in the focal plane of an objective lens .....	5 4
Table 3. Refractive index change and thickness of double line according to the laser irradiance. ....	6 2
Table 4. Fidelity results calculated from orientation decoding by ODS unit pattern; the bit errors for $\Delta O=0$ , $\Delta O=\pm 1$ , and $\Delta O=0, \pm 1$ . ....	9 5
Table 5. Fidelity results calculated from intensity decoding by ODS unit pattern; the bit errors for $\Delta I=0$ , $\Delta I=\pm 1$ , and $\Delta I=0, \pm 1$ . ....	100
Table 6. Summary of the writing/reading accuracy .....	107
Table 7. Fidelity results calculated from orientation downgrade-decoding by ODS unit pattern; the bit errors for $\Delta O'=0$ , $\Delta O'=\pm 1$ , and $\Delta O'=0, \pm 1$ . ....	108
Table 8. Fidelity results calculated from intensity downgrade-decoding by ODS unit pattern; the bit errors for $\Delta I'=0$ , $\Delta I'=\pm 1$ , and $\Delta I'=0, \pm 1$ . ....	111



# Chapter 1. Introduction

## 1.1 Direct Laser Writing with ultrashort pulse lasers

During the active research and development of lasers in the 1960s and 1970s, many experiments were conducted on the interaction between photons and materials. In 1978, Hill K.O. measured the UV radiation damage and the changes of refractive index by irradiating a continuous wave gas laser beam onto Ge-doped silica glass [1]. And using these characteristics, optical devices were fabricated on fibers and thin films. At this time, laser damage caused by visible laser and IR laser induced only a linear effect with low photon energy, which received little attention.

After the development of high energy density femtosecond pulse laser, Hirao et al. induced modifications inside silica and Ge-doped silica glass by using a femtosecond laser of 120 fs, 200 kHz, and 810 nm, and measured an increase in refractive index from 0.01 to 0.035 in 1996 [2]. The femtosecond pulse laser provided a solution to overcome the low photon energy of visible and NIR laser.

The high energy density of femtosecond pulsed lasers enables the nonlinear photoionization processes provide high energy sufficient for the valence electrons to move into the conduction band by following three different ways depending on the intensity and repetition rate of the laser [3,4], (i) Multiphoton ionization, (ii) tunneling ionization, and (iii)

avalanche ionization. A few picoseconds after, the laser excited electrons transfer their energy to the lattice, resulting in permanent material deformation. Due to these complex mechanism, femtosecond laser microfabrication can be applied to a wide range of materials.

## **1.2 Applications using direct laser writing**

The peak power of the fs laser beam is high, but the average fluence is relatively low, so it is more studied in laser processing of dielectric materials, polymers, and transparent glasses than laser processing of metals. Although the peak power of the fs laser beam is high, the average power is lower than continuous wave lasers, femtosecond lasers are more used for laser processing of dielectric materials, polymers, and transparent glasses than laser processing of metals, as shown in Figure 1.

Various optics including lens systems, micro resonators, and color filters for IR sensors are designed and manufactured with direct laser writing using ultra-short pulse lasers. In 1994, Michael T. Gale et al. produced continuous-relief micro optical elements (Fresnel microlenses, microlens array, kinoforms, and other continuous-relief phase elements) in photoresists by using CW HeCd laser [5]. He designed, manufactured and measured Fresnel lens with a diameter of 5 mm and a focal length of 10 mm (0.24 N.A.). Micro-lens having a diameter of 30  $\mu\text{m}$  up to 1 cm were also fabricated. The fabrication of the optical elements implemented in this paper requires several post-processing steps after direct

laser writing. Timo Gissibl et al. produced an ultracompact multi-lens objective by using two photon direct laser writing with 3D printing technology in 2016 [6]. He designed and fabricated singlet, doublet, and triplet with a height of about 115  $\mu\text{m}$  and a focal length of 68.3  $\mu\text{m}$  on a 170  $\mu\text{m}$  thick glass substrate. Naoto Tsutsumi et al. fabricated 3D microstructures and micro-lens arrays using negative photoresist SU-8 with a femtosecond Ti:sapphire pulse laser [7]. Piotr Wasylczyk et al. manufactured transmission phase gratings that serve as color filters in the visible [8]. By focusing the femtosecond laser pulse to the photoresist, each simple diffraction structure had the structure of a regular grid of pillars, and transmission of each grid has a wavelength dependency. In his paper, one basic unit was manufactured with a width of 450 nm and a height of 1.0  $\mu\text{m}$  to 2.4  $\mu\text{m}$ , which is important factor to determine the wavelength of transmission. Heming Wei et al. designed and produced a sensitive refractometric polymer micro-resonator sensor [9].

Direct laser writing is widely used not only for optics elements, but also for electronics in graphene/metal doped thin films [10–15], lithography [16–18], and micro 3-dimension printers [19,20]. In particular, Joachim Fischer, Min Gu, and Benjamin Harke brought the concept of stimulated emission depletion (STED) fluorescence microscopy to reduce the size of voxels modified by direct laser writing [16,17,21]. Although it has different characteristics depending on the medium, in both experiments, structures of less than 100 nm were fabricated.

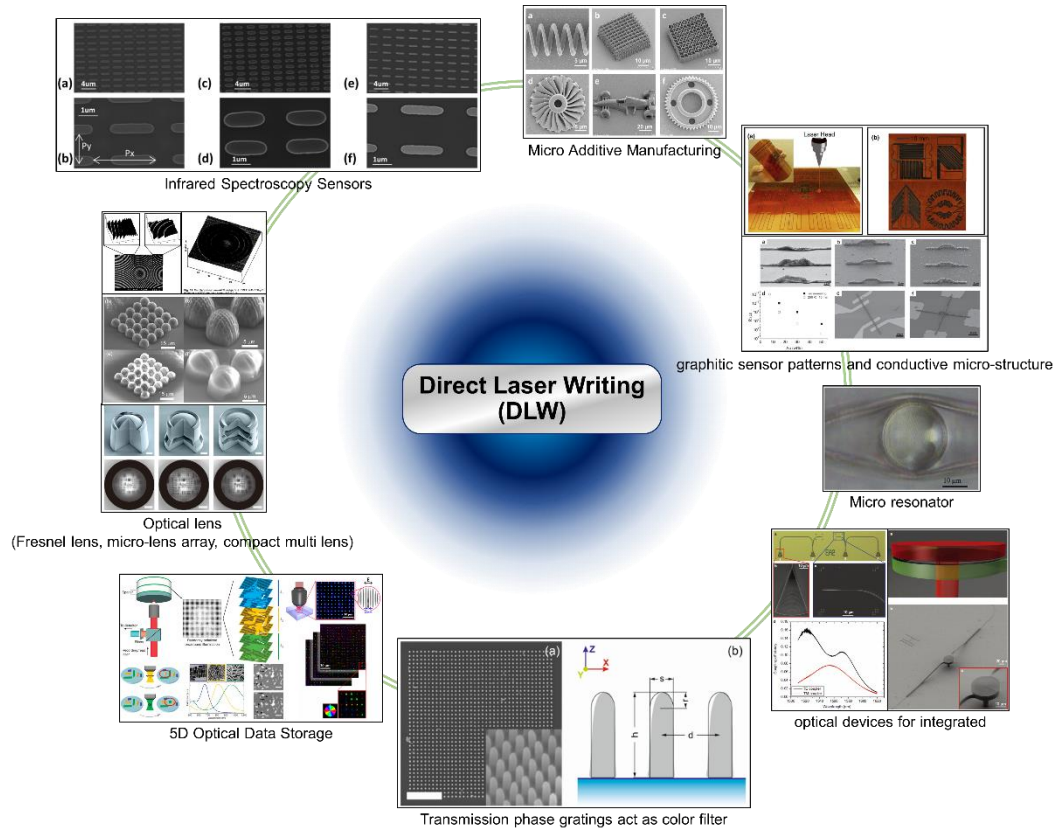


Figure 1. Various applications using direct laser writing

### 1.3 The scope of this manuscript

In this paper, a new type of direct laser writing in silver-doped zinc phosphate glasses by using femtosecond pulse laser is introduced. And the properties and multidimensional applications of type Argentum DLW are reported.

In chapter 2, the modeling for cluster formation of metallic cluster in silver-containing glass due to femtosecond laser pulses is covered which explains the morphology of silver clusters and distribution of metal species. And this chapter details the experimental set-up used in this paper and the main role of each part.

In chapter 3, based on near-field scanning optical microscopy (NSOM) images, chemical micro-probe analysis, spatial profile after soft etching, and numerical simulations of the silver species redistribution, the fs laser-induced spatial redistribution of silver species of our photosensitive silver-containing phosphate glasses is described correlatively.

Chapter 4 introduces the two-dimensional waveguides fabricated by Type A modifications. In particular, studies on the fabrication, performance and properties of symmetrical Y-junctions and asymmetrical Y-junctions are included. Asymmetric Y-junctions were fabricated by carving the two branches with different irradiance and the output ratios were measured. And it shows interesting results that can be used as an asymmetric splitter.

In Chapter 5, five-dimensional (5D) data storage has been investigated by using type A direct laser writing. A data storage unit of ellipse pattern, produced by anamorphic focusing of femtosecond laser, has been proposed to demonstrate 5D data storage (3D for XYZ, 1D for orientation of ellipse and 1D for fluorescence intensity). In the writing process, two different images of 4-bit bitmap format were embedded in one single image by combining both ellipse pattern orientation and laser irradiance. In the reading process, the two merged original images were successfully decoded by comparing each data storage

unit with a calibration matrix and restoring the levels of ellipse orientation and fluorescence intensity simultaneously.



## Chapter 2. Direct Laser Writing Experimental System

### 2.1 Interaction between fs pulse Laser and Materials

Since the development of dye lasers in the mid-1980s, fs lasers have been used in a variety of applications including ablation (drilling, cutting, marking), Photo-Lithography, Direct Laser Writing(DLW) , and micro 3D printing recently [22–25]. Ultra-short pulse laser is being developed continuously because the smaller the time scale of laser pulse, the more interaction between photon and material can be studied. For example, an ultrashort pulse laser is required for the mechanical study of molecular switching, the synthesis and decomposition of materials made by photosynthesis of plants, and the process of restoring perturbation due to photoelectric effect [26,27].

The interaction of photon and material depends on the type of material, lattice structure and energy exchange mechanism. Generally, some materials are known to have a process as shown in Figure 2. First, when the energy of photon is transferred to the material due to laser irradiance, multiphoton absorption and ionization proceed in the material. The energy transferred to the electron after the first step due to energy deposition is transferred into the molecules of the material and the vibration of the lattice, or phonon. After that, the perturbation caused by the photon enters into the process of relaxation to the energy equilibrium state. This process returns to equilibrium by heat diffusion, explosion, chemical reactivity, etc. We can induce material modification by irradiance of femtosecond laser

pulses and subsequent series of photo-material interactions before local material relaxation occurs.

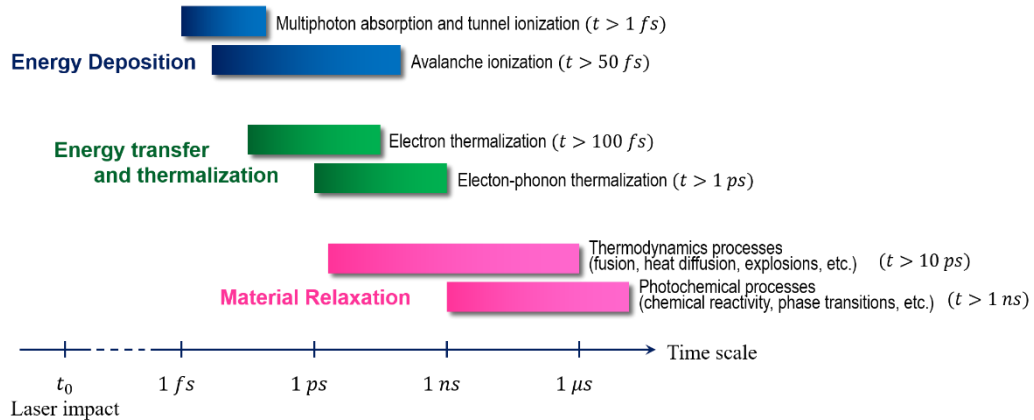


Figure 2 Time scale of the interaction between photon and material [28]

In addition to the irradiance parameters of the laser, modifications induced by pulse laser can be classified into three types according to morphological changes [29]: (1) type I modification: smooth refractive index change, (2) type II modification: birefringent refractive index modification, (3) type III modification: micro-explosions leading to empty voids. Type I modifications are relatively weak energy and induce smooth and isotropic refractive index changes in the focal volume of the laser. Type II modification is induced when a slightly higher energy laser pulse is irradiated on bulk of fused silica glass. The interference of the laser field and the induced electron plasma wave inscribe a writing pattern in the form of periodic nano-grating, which induces a birefringent refractive index change. Finally, type III modification is induced by the highest energy laser pulses, which leaves a writing pattern of low density or hollow core at the core by micro-explosion in focal volume. Figure 3 shows the sequence of steps and the writing patterns for the three types.

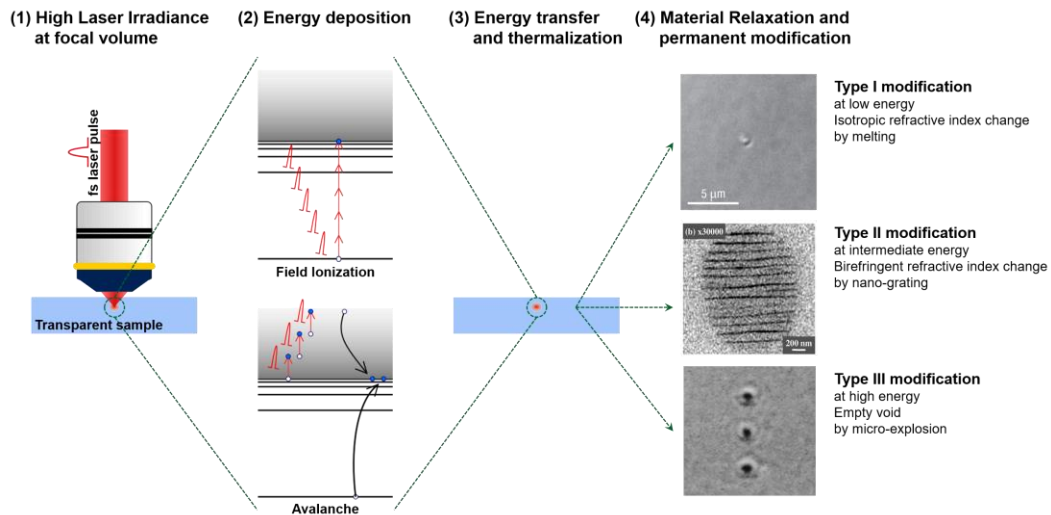


Figure 3 The process and results of interaction of fs laser pulse and transparent materials : (1) high laser irradiance at focal volume in transparent material; (2) process of energy deposition by multiphoton absorption and avalanche ionization; (3) process of energy transfer and thermalization; (4) result of material relaxation and permanent modification by melting, nano-grating, and micro-explosion [29].

## 2.2 Silver-containing glass sample

### 2.2.1 General formation process for metallic cluster

After DLW on a photosensitive glass sample doped with a Nobel metal (i.e. Cu, Au, Ag), the nucleation of the metallic ions and further cluster are created induced under appropriate reduction-oxidation conditions [30]. This glass sample also interacts with the laser pulse through above process shown in Figure 2. In the first step, ionization of the

glass occurs while the fs laser pulse is irradiated. The free electrons are then diffused and trapped in the holes, the glassy network, and the doped metal ions [31]. At the same time, free electrons absorb the laser's photon energy and transfer energy to the lattice. The temperature rises from the subsequent pulse train, and the diffusion of metallic species is thermally activated. This leads to the continuous kinetic reaction and clusters of metallic ions begin to form. The cumulative fs pulse causes photo-dissociation to occur in the center of the focal volume, leaving only the metallic cluster at the periphery of beam waist. At the edge of the beam, it is not enough energy to reach photo-dissociation, but it satisfies the conditions which ionization and reduction-oxidation processes occur. The laser-induced redistribution of metallic species causes a forced charge separation inside the glass, forming a static electric field,  $\vec{E}_{dc}$ . These static electric fields inside the glass bring nonlinear properties. In particular, the second harmonic generation is derived by providing a second-order susceptibility which was zero before the formation of metallic cluster [32].

### **2.2.2 The formation process for Silver-doped Zinc Phosphate glasses**

The glass sample used in this experiment was silver containing optical glass based on zinc phosphate glasses. This glass sample is developed and researched by Institut de Chimie de la Matière Condensée de Bordeaux (ICMCB), and its photo-sensitivity, fluorescence property, and spectroscopic are different depending on the chemical composition ratio. The produced glass samples were used for direct laser writing in the

Short pulse Lasers Applications and Materials (SLAM) lab at Centre Lasers Intenses et Applications (CELIA).

The silver-ions doped glasses used in this experiment also apply to the cluster formation process of the noble metal described above. Figure 4 shows the process of silver cluster described above, which has ring shape. In the first step, when the fs-laser pulse is irradiated on the silver-containing glass, free electrons are generated as shown in the yellow zone of Figure 4 (a). The generated free electrons form  $\text{Ag}^0$  by kinetic reaction with silver ions.  $\text{Ag}^0 : \text{Ag}^+ + e^- \rightarrow \text{Ag}^0$  At the same time,  $\text{Ag}^{2+}$  is generated by a hole trapped in  $\text{Ag}^+$ .  $\text{Ag}^{2+} : \text{Ag}^+ + h^+ \rightarrow \text{Ag}^{2+}$  However,  $\text{Ag}^{2+}$  generated at this time has limited mobility by surrounding phosphate chains. So it's mobility is negligibly low compared to that of  $\text{Ag}^+$ . The reaction to generate  $\text{Ag}^0$  continues until the concentration of free electrons disappears. At this time, the distribution of  $\text{Ag}^0$  and  $\text{Ag}^{2+}$  is located in the center of the beam as shown in green circle in Figure 4 (a).

As shown in Figure 4 (b), the area where  $\text{Ag}^0$  exists is diffused, and the green circle is slightly enlarged. As absorbed laser pulse energy is transferred to lattice and molecular, heat diffusion occurs as shown in blue circle of Figure 4 (b) by raising temperature in focal volume.  $\text{Ag}^0$  ions activated by temperature encounter  $\text{Ag}^+$  ions, which causes formation of  $\text{Ag}_2^+$  as shown in Figure 4 (b) red circle.  $\text{Ag}_2^+ : \text{Ag}^0 + \text{Ag}^+ \rightarrow \text{Ag}_2^+$  This reaction finishes when  $\text{Ag}^0$  is destroyed. Then  $\text{Ag}^{2+}$  will be distributed in clusters as shown in red circle in Figure 4 (c).

The sequence of above steps is fast-paced and already terminates before the next pulse, causing all  $\text{Ag}^0$ ,  $e^-$  and  $h^+$  to disappear. The next pulse brings photo-dissociation,

which begins to destroy the already formed  $\text{Ag}^{2+}$  cluster. This dissociation only occurs at the center where there is sufficient energy, and the silver clusters continue to accumulate in the periphery of the beam. After this series of processes has been repeated, only the ring-shaped cluster is left inside the glass as shown in Figure 4 (d) [33,34]. This  $\text{Ag}_2^+$  cluster has a high durability and remains almost permanent engraved inside the glass sample [35].

The associated space charge separation in glass produces a static electric field  $\vec{E}_{\text{dc}}$  as shown in Figure 4 (d) black arrows. In the silver containing glasses, the laser induced-static electric field has high value up to  $10^9$  V/m, which almost reaches to the electrical breakdown of material. And this allows an effective second order nonlinearity has follow value.  $\chi_{\text{eff}}^{(2)} = 3E_{\text{dc}}\chi^{(3)} \sim 1$  pm/V [36,37]. This brings one- or two- ring shape of second harmonic generation response [36,37].

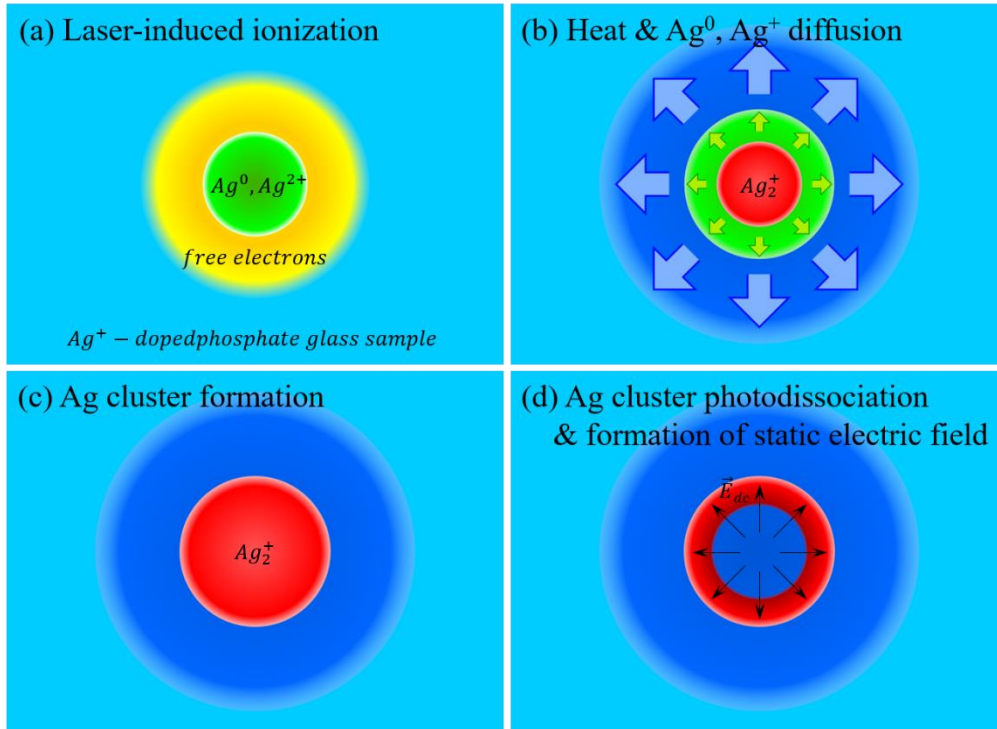


Figure 4 The process for formation of laser-induced ring shape cluster within the silver-doped phosphate glasses [38]

### 2.2.3 Modeling for cluster formation of metallic cluster

The cluster formation process of the metallic ions can be expressed by the following general modeling equation. Evolution of temperature  $T$ , electron concentration  $n_e$ , hole concentration  $n_h$ , and concentration of metallic species  $n_M$ , static electric field induced by cluster  $E_{dc}$  can be written as:

$$\frac{\partial T}{\partial t} = \Gamma_{D_{th}} + S_{th} \quad \text{Equation 1}$$

$$\frac{\partial n_e}{\partial t} = \Gamma_D(T, n_e) + \Gamma_M(T, n_e, \vec{E}_{dc}) + \Gamma_K(n_e, n_h, n_M) + \Gamma_I + \Gamma_{Diss}(n_M) \quad \text{Equation 2}$$

$$\frac{\partial n_h}{\partial t} = \Gamma_K(n_e, n_h, n_M) + \Gamma_I \quad \text{Equation 3}$$

$$\frac{\partial n_M}{\partial t} = \Gamma_D(T, n_M) + \Gamma_M(T, n_M, \vec{E}_{dc}) + \Gamma_K(n_M, n_e, n_h) \pm \Gamma_{Diss}(n_M) \quad \text{Equation 4}$$

$$\frac{\partial \vec{E}_{dc}}{\partial t} = \frac{Q(n_M, n_e, n_h)}{\epsilon_0 \epsilon_{dc}} \quad \text{Equation 5}$$

where  $\epsilon_0$  and  $\epsilon_{dc}$  are permittivity at vacuum and dielectric material. In Equation 1,  $\Gamma_{D_{th}}$  and  $S_{th}$  present the heat diffusion and the laser induced heat source respectively.  $\Gamma_D(T, n_e)$  and  $\Gamma_M(T, n_e, \vec{E}_{dc})$  in Equation 2 are terms for the diffusion and the mobility. And  $\Gamma_K$  is term for kinetic reactions of metallic species and  $\Gamma_I$  represent the laser induced electron and hole source in Equation 2 and Equation 3. In Equation 3, the hole mobility term is neglected because of its relatively low impact. In Equation 4,  $\Gamma_{Diss}(n_M)$  represents the dissociation pathways of involving metallic clusters. Here, when the metal species

dissociate, the sign has a negative value, whereas when the cluster is formed, the sign has a positive value.  $Q(n_M, n_e, n_h)$  in Equation 5 describes the self-induced electric charge redistribution, and  $\vec{E}_{dc}$  represent the static electric field generated by ring-shape metallic cluster.

Applying these equations to silver-doped glasses, the metallic species can be represented by the silver ion  $Ag^+$ , the silver component  $Ag^0$ , the doubly ionized silver ion  $Ag^{2+}$ , and silver cluster  $Ag_2^+$ . We will not consider the larger silver cluster  $Ag_m^{x+}$ ,  $m > 2$ . This is because there is little mobility even if  $m = 2$ , and enough information can be obtained up to considering  $Ag_2^+$ . Also we suppose that the  $Ag^+$  and  $Ag^0$  have mobility, while the  $Ag^{2+}$  and  $Ag_2^+$  have no mobility. From these assumptions and conditions, Equation 4 can be written as the following four equations.

$$\begin{aligned} \frac{\partial n_{Ag^+}}{\partial t} = & \Gamma_D(T, n_{Ag^+}) + \Gamma_M(T, n_{Ag^+}) \\ & + \Gamma_K(n_{Ag^+}, n_e, n_h, n_{Ag^0}, n_{Ag^{2+}}, n_{Ag_2^+}) + \Gamma_{Diss}(n_{Ag_2^+}) \end{aligned} \quad \text{Equation 6}$$

$$\frac{\partial n_{Ag^0}}{\partial t} = \Gamma_D(T, n_{Ag^0}) + \Gamma_K(n_{Ag^0}, n_e, n_h, n_{Ag^+}, n_{Ag^{2+}}, n_{Ag_2^+}) \quad \text{Equation 7}$$

$$\frac{\partial n_{Ag^{2+}}}{\partial t} = \Gamma_K(n_{Ag^{2+}}, n_e, n_h, n_{Ag^+}, n_{Ag^0}) \quad \text{Equation 8}$$

$$\frac{\partial n_{Ag_2^+}}{\partial t} = \Gamma_K(n_{Ag^+}, n_{Ag^+}, n_{Ag^0}) - \Gamma_{Diss}(n_{Ag_2^+}) \quad \text{Equation 9}$$

The concentration of silver species during cluster formation can be expressed by the above equations.

Absorption of laser pulse energy is mainly explained by multiphoton ionization (MPI), impact ionization, and recombination. In Equation 1 and Equation 2, the laser-induced electron and hole source is expressed as

$$\Gamma_I = \sigma_K \left( \frac{I}{\hbar\omega} \right)^K (n_{at}^0 - n_e) + \sigma \frac{I}{U_g} n_e - \frac{n_e}{\tau_r} \quad \text{Equation 10}$$

where  $I(r, t, z)$  is the distribution of the laser intensity, experimentally Gaussian distribution. And the first term represents MPI process, the second term is written for impact ionization, and the last term corresponds to the recombination process. In Equation 10,  $\sigma$  is the inverse bremsstrahlung cross section,  $\tau_r$  represents electron-hole recombination time.

The intensity of the laser pulse decreases as follow:

$$\frac{\partial I}{\partial \zeta} = -\sigma_K \left( \frac{I}{\hbar\omega} \right)^K (n_{at}^0 - n_e) K \hbar\omega - \sigma I n_e \quad \text{Equation 11}$$

where the input laser pulse intensity distribution  $I|_{\zeta=0} = I_0\Phi(r)e^{-\tau^2/\tau_0}$  with  $\tau_0 = \tau_p/2\sqrt{\ln 2}$ ,  $\tau_p$  is the laser pulse duration(FWHM),  $\zeta \in [0, L_\zeta]$ . The time in the frame moving with group velocity of the laser pulse  $v_g$  is  $\tau = v_g t - z$ , and the position of the laser pulse in space, correspondingly to its central time slice ( $\tau = 0$ ):  $\zeta = v_g t$ .

Experimentally, the energy absorption is only about 0.04% to 0.5% when the injection laser irradiance ranges from 2 TW/cm<sup>2</sup> to 9 TW/cm<sup>2</sup>. So the electron and hole source term after each laser pulse can be approximate as follows:  $\bar{n}_e(r) = n_e^0\Phi(r)^K$ , where  $n_e^0 = 10^{17} \text{ cm}^{-3}$  for all considered pulse irradiance. And  $\Phi(r)$  is term for a normalized beam shape with radial symmetry, where  $r$  is the radial coordinate and  $K$  is the order of the multiphoton ionization processes. So for train of laser pulses, the electron and hole source term can be written as follow:

$$\Gamma_I = \sum_{n=1}^{N_p} \bar{n}_e(r)\delta(t - nt_L) \quad \text{Equation 12}$$

where  $t_L = 1/\nu$ ,  $N_p$  is the number of pulse train, and  $\nu$  is the repetition rate of laser pulse.

Finally the absorption of the laser pulse intensity can be estimated by solving Equation 11 with  $n_e = \bar{n}_e(r)$  skipping the avalanche term. The radial distribution of the absorbed energy density  $S(r)$  is

$$S(\vec{r}) = \frac{1}{L_z} \int_{-\infty}^{+\infty} I_{abs}(r, \tau) d\tau \quad \text{Equation 13}$$

where  $I_{abs}(r, \tau) = I(r, \tau)|_{z=0} - I(r, \tau)|_{z=L_z}$ . The value of the absorbed energy  $E_{abs}$  is

$$E_{abs} = \int_0^{\infty} \int_0^{\infty} I_{abs}(r, \tau) r dr d\tau \quad \text{Equation 14}$$

The temperature distribution in space and time is calculated according to

$$\frac{\partial T}{\partial t} = D_{th} \Delta T + \frac{1}{C_p \rho} \sum_{n=1}^{N_p} S(r) \delta(t - nt_L) \quad \text{Equation 15}$$

where  $S$  is the heat source term calculated in Equation 13,  $C_p$  and  $\rho$  are specific heat capacity and the density of the glass, respectively, and  $N_p$  is the number of laser pulses.  $D_{th}$  is the heat diffusion coefficient in the glass, assumed as a constant. The first term in this equation represents the temperature diffusion  $\Gamma_{D_{th}}$  in Equation 1, and the second term corresponds for laser energy absorption  $S_{th}$  in Equation 1.

Diffusion  $\Gamma_D$  and mobility  $\Gamma_M$  terms of general model for silver ions  $Ag^+$  and electron  $e^-$  are coupled:

$$\Gamma_D + \Gamma_M = \nabla(D\vec{\nabla}n) - \nabla(\mu\vec{E}_{dc}n) \quad \text{Equation 16}$$

where  $D$  is the diffusion coefficient of the considered species,  $n$  is the its concentration,  $\mu = \frac{q}{kT}D$  is the mobility in the electric field  $\vec{E}_{dc}$  defined according to the Einstein relation, and  $q$  is the particle charge. Generally, the diffusion process of the metallic species depends on the lattice temperature  $T$ . So diffusion coefficient can be expressed as:

$$D(T) = D(T_0) \exp\left(\frac{E_a}{kT_0}\right) \exp\left(-\frac{E_a}{kT}\right) \quad \text{Equation 17}$$

where  $k$  is the Boltzmann constant and  $E_a = 0.8$  eV is the activation energy [39].

The charge distribution  $Q$  for particular case of silver-containing glass is calculated as follow:

$$\frac{Q}{q_0} = n_{Ag^+} + 2n_{Ag^{2+}} + n_{Ag_2^+} + n_h - n_e - n_{L^-} \quad \text{Equation 18}$$

where  $q_0$  is the absolute value of the electron charge.  $n_{L^-}$  is concentration of the input silver ion.  $n_{L^-} = n_{Ag^+}^0$ .

Here, the kinetic terms  $\Gamma_k$  for clustering silver ions can be expressed with the electrons  $e^-$ , holes  $h^+$ , silver ions  $Ag^+$ , complexes of silver ions with electrons  $Ag^0$ , doubly

ionized silver ions  $Ag^{2+}$ , and silver cluster  $Ag_2^+$ . It all starts with the first femtosecond laser pulse. This pulse brings the photo-ionization of the glass. Photo-electrons and holes in this process are trapped in the silver ions contained in the glass. Thus there are three competitive kinetic reactions. electron-hole recombination,  $Ag^+ + e^- \rightarrow Ag^0$ , and  $Ag^+ + h^+ \rightarrow Ag^{2+}$ .  $Ag^0$ , which has relatively high mobility, undergoes a chemical reaction with silver ions  $Ag^+$  again, forming a silver cluster  $Ag_2^+$ .  $Ag^0 + Ag^+ \rightarrow Ag_2^+$ . For electrons and holes,  $\Gamma_k$  in Equation 2 and Equation 3 are as follow:

$$\Gamma_k(n_e, \dots) = -K_r n_e n_h - K_r n_{Ag^{2+}} n_e - K_{Ag^0} n_{Ag^+} n_e \quad \text{Equation 19}$$

$$\Gamma_k(n_h, \dots) = -K_r n_e n_h - K_r n_{Ag^0} n_h - K_{Ag^{2+}} n_{Ag^+} n_h \quad \text{Equation 20}$$

Here the first term is for electron-hole recombination and is related to the recombination constant  $K_r$ , estimated as  $K_r = \frac{1}{\tau_r n_e^0}$ . The second terms are for recombination of electron- $Ag^{2+}$  and hole- $Ag^0$ . And the last terms represent the electron/hole trapping by silver ions characterized by thermally activated kinetic constants  $K_{Ag^0}$  and  $K_{Ag^{2+}}$ .

In Equation 6, the concentration of silver ions  $n_{Ag^+}$  expressed as partial derivative of time can be written as:

$$\Gamma_k(n_{Ag^+}, \dots) = -K_{Ag^0}n_{Ag^+}n_e - K_{Ag^{2+}}n_{Ag^+}n_h - K_{Ag_2^+}n_{Ag^+}n_{Ag^0} + K_r a_{Ag^0}n_h + K_r n_{Ag^{2+}}n_e + 2K_{Ag^+}n_{Ag^{2+}}n_{Ag^0} \quad \text{Equation 21}$$

where the first and second terms are for the trapping of free electron and hole respectively. The third term represents the formation of silver cluster  $Ag_2^+$ , and the fourth and fifth terms correspond to the recombination processes of hole- $Ag^0$  and electron- $Ag^{2+}$ .

Similarly, in Equation 7, Equation 8, and Equation 9,

$$\Gamma_k(n_{Ag^0}, \dots) = K_{Ag^0}n_{Ag^+}n_e - K_{Ag^{2+}}n_{Ag^+}n_{Ag^0} - K_r n_{Ag^0}n_h - K_{Ag^+}n_{Ag^{2+}}n_{Ag^0} \quad \text{Equation 22}$$

$$\Gamma_k(n_{Ag^{2+}}, \dots) = K_{Ag^{2+}}n_{Ag^+}n_h - K_r n_{Ag^{2+}}n_e - K_{Ag^+}n_{Ag^{2+}}n_{Ag^0} \quad \text{Equation 23}$$

$$\Gamma_k(n_{Ag_2^+}, \dots) = K_{Ag_2^+}n_{Ag^+}n_{Ag^0} \quad \text{Equation 24}$$

The thermal dependence of the kinetic constants is evaluated according to the Arrhenius equation with pre-exponential factor given by the collision theory [40].

$$K_{Ag}(T) = K_{Ag}(T_0) \sqrt{\frac{T}{T_0}} \exp\left(\frac{E_a}{kT_0}\right) \exp\left(-\frac{E_a}{kT}\right) \quad \text{Equation 25}$$

This dependency also applies to reactions of silver species formation. The  $K_{Ag}$  is the kinetic constants for all silver species.:  $K_{Ag^0}$ ,  $K_{Ag^{2+}}$ ,  $K_{Ag_2^+}$ ,  $K_{Ag^+}$ .

Laser induced silver clusters' dissociation is applied to the general model. The photo-dissociation of metallic cluster is a thermally assisted process determined by the ratio between the photon energy and the dissociation energies of different dissociation processes of the clusters. That is the reason the dissociation coefficient  $K_{diss}$  is an experimental parameter derived from the measurements. The decrease of the silver cluster  $Ag_2^+$  in the center of the laser focal volume is caused by following two factors.: The high temperature of lattice and the photon energy from the fs laser pulse. Firstly, when lattice reaches a high enough temperature (about 200 K, lower than  $T_g$ ), the thermal dissolution of silver cluster can be described by the interplay between the redox potential of the glass composition, ionization of the glass, and the glass temperature. Secondly, photon-dissociation due to high energy laser pulses is explained by multiphoton dissociation.

Considering the dissociation of the smallest silver clusters ( $Ag_m^+$ ,  $m > 2$ ), we will take an empirical approach. Both multiphoton assisted dissociation and high temperature assisted dissociation occur through following chemical pathway.:



So dissociation term in Equation 2, Equation 4, Equation 6, and Equation 9 can be written as:

$$\Gamma_{Diss} = \alpha_{Diss} \sum_{n=1}^{N_p} K_{Diss} n_{Ag_2^+} \delta(t - nt_L) \quad \text{Equation 27}$$

where  $\alpha_{Diss}$  corresponds to the mass and charge conservation according to the dissociation pathway ( $\alpha_{Diss} = -1$  for  $Ag_2^+$ ,  $2$  for  $Ag^+$ , and  $1$  for  $e^-$ ). The distribution of laser intensity and the temperature of lattice that induce dissociation are the same as the distribution of irradiated laser intensity. And Dissociation function  $K_{Diss}(r)$  takes the form of a step-function by dissociation functionality. In other words, the dissociation function has a unity value at the center of the Gaussian beam and a value close to zero at the periphery of the beam. So  $K_{Diss}(r)$  is phenomenologically presented as a function of the absorbed laser pulse energy by the dependence on the source term S in the heat diffusion Equation 15:

$$K_{diss}(r) = 1 - \exp\left[-\frac{S(r)^N}{S_0^N}\right] \quad \text{Equation 28}$$

The two free parameters  $S_0$  and N are terms for the position and the steepness of the dissociation threshold.

## 2.2.4 Optical properties of silver containing glass

The writing patterns with silver-cluster created produced above processes has a different properties from the three types of modifications, and is classified separately as type Argentum (so called type A) [41]. Type Argentum requires less laser energy than other types and bring different morphology of refractive index changes. Type I modifications lead to smooth and negative refractive index changes, while Type Argentum is characterized by a positive change refractive index along the silver clusters made. That is, the pattern of the ring shape is created. Figure 5 shows the new position of type Argentum.

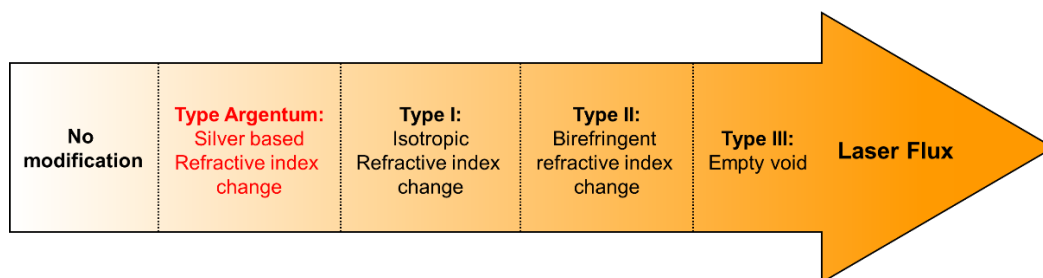


Figure 5 Classification of modifications according to laser flux and types of refractive index change [41]

Figure 6 shows the configurations, fluorescence images of confocal microscopy and images of High Resolution Scanning Electron Microscopy(HRSEM) when the laser beam is irradiated on silver containing glass sample. Figure 6 (a) is the configuration that shows the focusing volume when the laser beam is irradiated onto the sample. In the edge of writing zone, the silver cluster is induced. Figure 6 (b) shows the fluorescence image of a laser induced silver cluster at the front and side view. Figure 6 (d) shows the chessboard

pattern by moving the sample on the same plane. In Figure 6 (e), the existing writing pattern is erased by secondary writing and rewritten at the overlapping part.

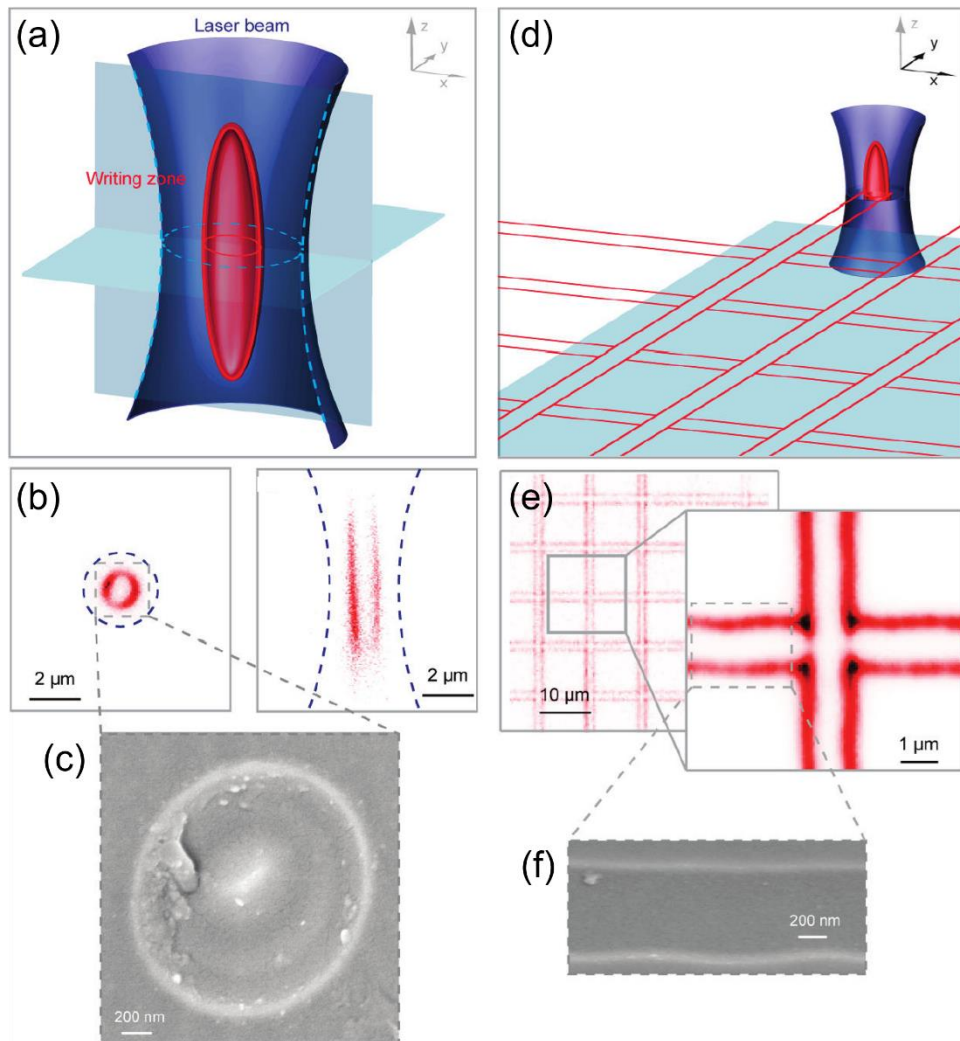


Figure 6 Configurations of type argenti modification with stationary focus (a) and in the same plane (g). Fluorescence images of writing pattern in the front and side view (b, e). Images obtained by High Reflection Scanning Electron Microscopy(HRSEM) (c, f). [42]

Type A modifications also differ in the sign of the refractive index change. In Type I, Figure 7 (a) has a negative change in refractive index, but in Type A it has a positive change as shown in Figure 7 (b) [41].

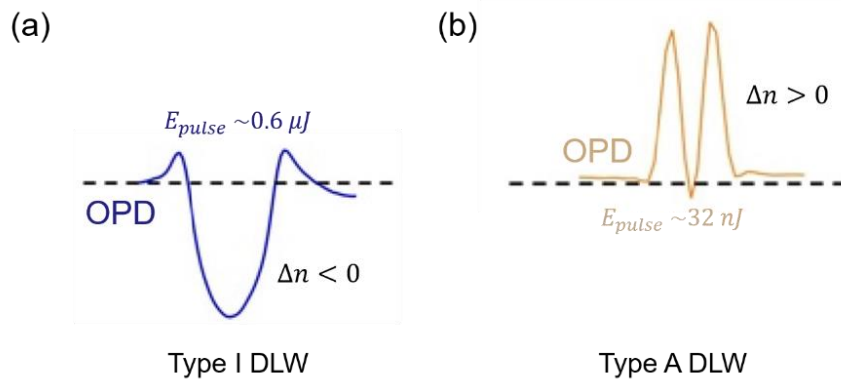


Figure 7 Comparison of refractive index changes between type I and type A [41]

Silver-doped phosphate glasses have the fluorescence properties shown in Figure 8 [28]. The three glass sample differ in compositions: (expressed in mol percent) (1) Poly-phosphate: 61.14  $P_2O_5$  – 21.58  $Ga_2O_3$  15.28  $Na_2O$  – 2  $Ag_2O$ , (2) Pyro-phosphate: 46.6  $P_2O_5$  – 16.45  $Ga_2O_3$  – 34.95  $Na_2O$  – 2  $Ag_2O$ , (3) Ortho-phosphate: 51.53  $P_2O_5$  – 12.12  $Ga_2O_3$  – 51.53  $Na_2O$  – 2  $Ag_2O$ , keeping the ratio  $Ga_2O_3 / P_2O_5 = 0.35$  constant. Samples of these combinations have common fluorescence emission spectra from  $\lambda_{em} = 450$  nm to  $\lambda_{em} = 650$  nm when excited with excitation wavelength at  $\lambda_{ex} = 405$  nm. The intensity of fluorescence varies depending on the intensity of irradiance, writing speed, and number of writing pulses. As Figure 8 (b) shows, the faster the writing velocity, the smaller the number of pulses that affect the writing structure, as a result it bring lower fluorescence intensity.

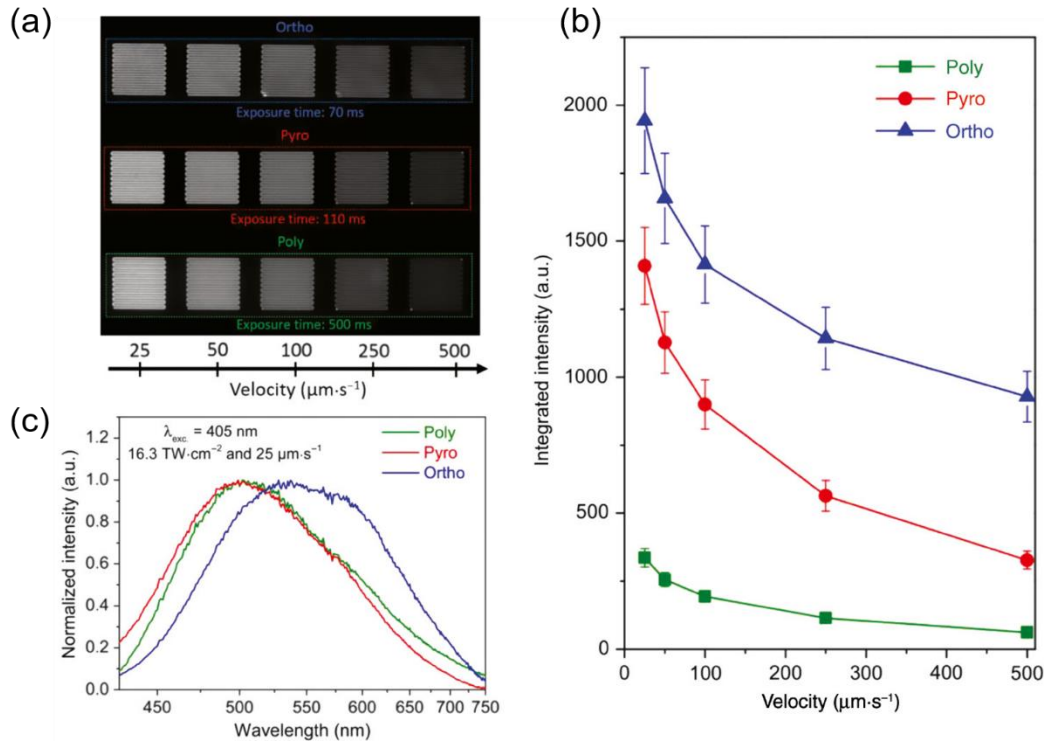


Figure 8 Fluorescence properties of silver-containing phosphate glass (a) Fluorescence image of structures engraved on glasses sample with three different chemical composition, (b) Fluorescence intensity according to writing velocity, (c) Spectrum distribution of emitted light when excited with a laser of 405 nm wavelength [28].

In Figure 9 silver-doped phosphate glasses exhibited refractive index change ranging from  $0.9 \times 10^{-3}$  to  $8 \times 10^{-3}$  when irradiated with fs pulse laser from  $6 \text{ TW}/\text{cm}^2$  to  $9 \text{ TW}/\text{cm}^2$  [43]. The variation in refractive index also depends on the laser irradiance, writing speed, and number of writing pulses. The larger the irradiance and the more the number of pulses (i.e. the lower the writing speed), the larger the refractive index change and the greater the fluorescence intensity.

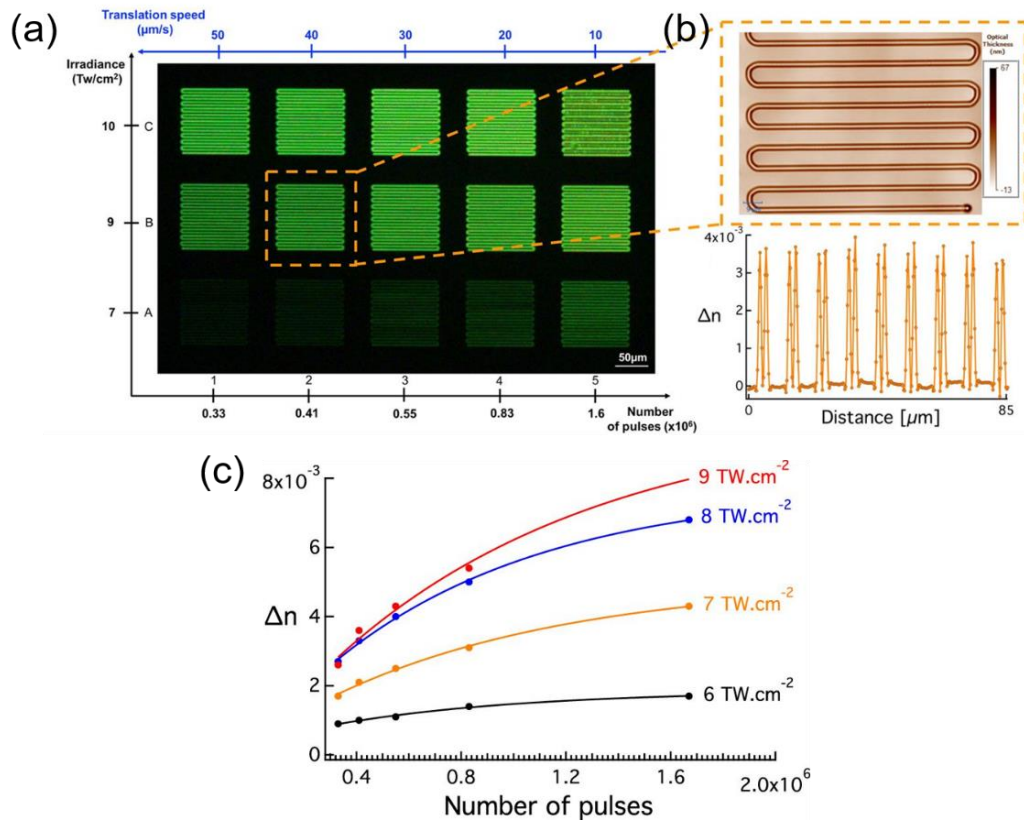


Figure 9 Refractive index change for laser irradiance and number of pulses; (a) matrix of structures for 2 parameter changes; (b) Image showing optical path difference for one structure; (c) Graph showing refractive index change for two parameters change [43]

## 2.3 Experimental set-up: fs-Laser, AOM and SLM

### 2.3.1 femtosecond laser and Experimental set-up

Yb:KGW femtosecond laser (T-pulse 200, Amplitude system, 9.8 MHz repetition rate, average power 2.4 W, 390 fs pulse FWHM duration and operating at 1030 nm) was used for DLW. Figure 10 shows the complete experimental set-up for DLW with Acousto-Optic Modulator, Spatial Light Modulator, and XYZ stage. When writing, mainly Zeiss air objective (20x, NA = 0.75) and Mitutoyo air objective (20x, NA = 0.40) were used for focusing. Newport company's XPS was used for XYZ positioning of the sample within few nano-meter resolution.

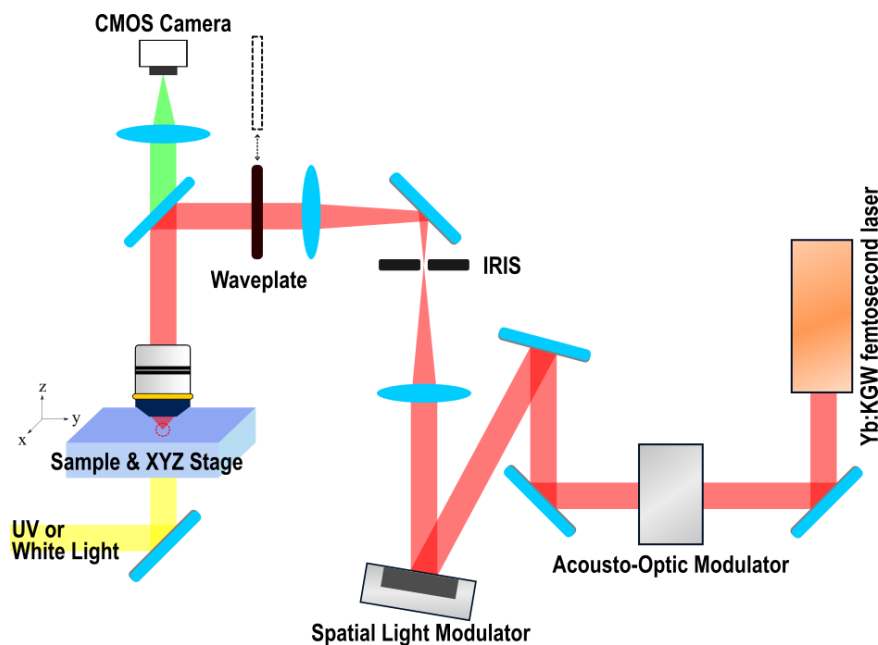


Figure 10 Experimental Setup Schematic for Direct Laser Writing; fs laser, Acousto-Optic Modulator, Spatial Light Modulator, and XYZ stage.

## 2.3.2 Acousto-Optic Modulator

The power of the laser beam can be controlled by adjusting the voltage applied to the Acousto-Optic Modulator (AOM). The voltage across the material of the AOM controls the intensity of sound, and the intensity of sound modulates the intensity of the diffracted beam. In this study, fused silica was used as an acousto-material and a product operating at a velocity of 5960 m/s (model number: AMQ80-A0.7-L1030.1064-Z20, AA Opto-Electronic company). As the voltage across the fused silica can be adjusted from 0 V to 1 V, so the laser power that is diffracted into  $m = 0$  order can be varied from 0 W to 1.80 W. At this time, the applied voltage and output power do not have a linear relationship but look like sigmoid function shown as Figure 11. Therefore, we can inversely calculate the irradiance to the sample from the applied voltage.

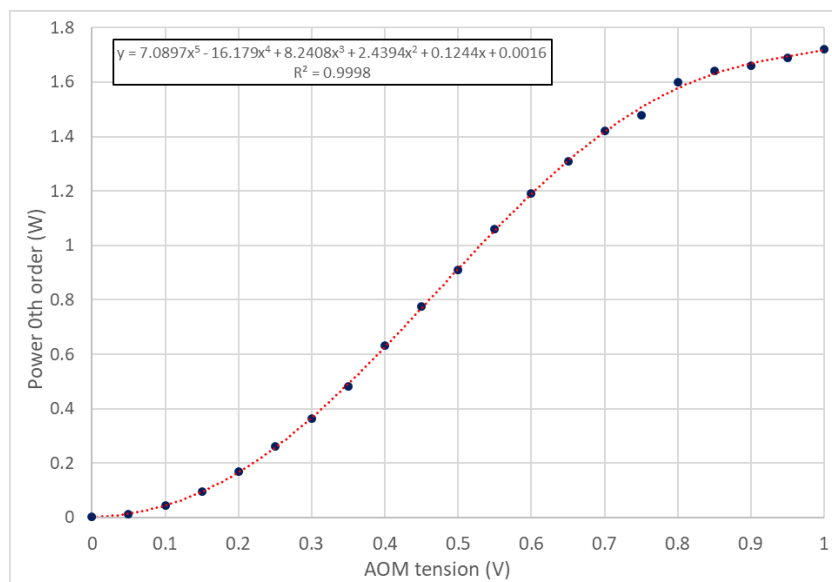


Figure 11 Graph showing the relationship between voltage to both fused silica and laser power at  $m=0$  order

### 2.3.3 Spatial Light Modulator

The laser beam passing through the AOM can be adjusted two-dimensionally at the focal plane of the objective lens via the Spatial Light Modulator(SLM). That is, the spatial distribution of light such as the phase, polarization state, and propagation direction can be modulated according to the information we need. In this study, liquid-crystal-silicon SLM (LCOS, X10468-03, 800 × 600 pixel, Hamamatsu Photonics) was used to control the wavefront of the laser beam. Figure 12 show a program coded by IGOR program to control phase on SLM mask. With this program, symmetrical focusing, asymmetrical focusing, Hermite-Gaussian focusing, and Laguerre-Gaussian focusing were enabled, and parameters were set to precisely manipulate the focusing position and spatial shape of the beam. Table 1 The SLM mask which control the phase of laser beam and the DLW patterns in the silver containing glass for different modes of focusing. Table 1 shows the SLM mask for respective focusing mode and DLW patterns in silver containing glass.

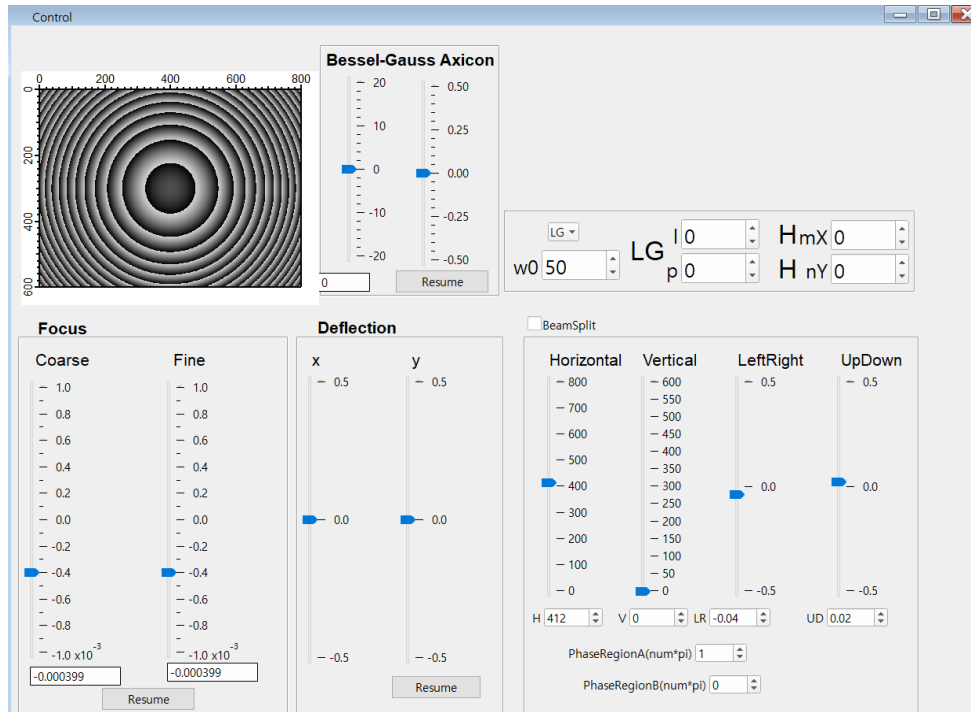


Figure 12 IGOR Program, which is designed to control SLM mask, enables several modes of focusing and precisely adjust the positioning of the laser beam.

	Symmetrical focusing	Anamorphic focusing	Hermite-Gaussian focusing	Laguerre-Gaussian focusing
SLM Phase mask				
DLW patterns in silver doped glass				

Table 1 The SLM mask which control the phase of laser beam and the DLW patterns in the silver containing glass for different modes of focusing.



## **Chapter 3. 1-dimensional DLW and its spatial redistribution of Silver species**

### **3.1 Introduction**

Femtosecond (fs) laser modification technology of materials has made tremendous progress over the past decade, to access a large panel of applications that require special optical, physical and/or chemical properties associated with integrated bulk or surface functionalities [44]. While considering laser-induced element redistribution, most of the reported literature deals with processes in thermal regime with temperature increase above glass fusion [45,46]. Additional potentialities rely on the innovative synthesis of prepared materials with photosensitive agents [34]. In this framework, controlling the photosensitive agents under laser irradiation in a non-thermal regime, as well as the spatial redistribution and chemical evolution due to activated chemical reactivity, is of prime importance to achieve reliable nano- and micro-scale material changes with high optical quality. Such control and understanding is highly challenging since it involves multi-scale material changes, which requires correlative investigation approaches.

In chapter 3, based on near-field scanning optical microscopy (NSOM) images, chemical micro-probe analysis, spatial profile after soft etching, and numerical simulations of the silver species redistribution, the fs laser-induced spatial redistribution of silver species of our photosensitive silver-containing phosphate glasses is described correlatively.

These results corroborate each other, and have led us to retrieve for the first time the nanoscale spatial profile of soft chemical etching rate of laser-induced modifications.

### **3.2 Experimental Methods: used glass sample, laser irradiance, and analyses**

A silver-containing zinc phosphate glass 55 ZnO - 40P<sub>2</sub>O<sub>5</sub> - 4Ag<sub>2</sub>O - 1Ga<sub>2</sub>O<sub>3</sub> (in mol. %) was used to fabricate 1 dimensional patterns as previously detailed [47]. Direct laser writing (DLW) was carried out with a Yb fs oscillator (Amplitude Systèmes, T-pulse 500, 9.1 MHz, 1030 nm, 390 fs FWHM), focused with a microscope objective (Mitutoyo, M Plan Apo NIR, 20x N.A. 0.4).

DLW was performed to create a structure with a length of 400  $\mu\text{m}$  by longitudinally translating the glass sample along the laser beam propagation. Sample velocity was 100  $\mu\text{m/s}$  and laser irradiance was 5 - 10 TW/cm<sup>2</sup>, typically. The irradiated sample was then re-polished perpendicularly to these fluorescent structures, to make them intersect the glass interface. The white light image of the sample produced after above process is shown in Figure 13(a). Figure 13 (b, c) are images obtained after focusing a laser beam of 405 nm and 632.8 nm with an objective lens.

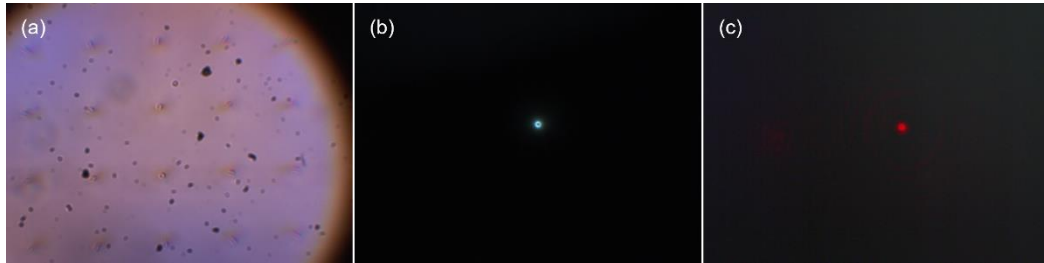


Figure 13 (a) White light image of 1D DLW patterns sample after etching process; (b, c) Images obtained by CMOS camera after injection of 405 nm and 632.8 nm laser beam with objective lens.

NSOM experiments were performed in illumination mode [48], where point-like light injection was achieved with a tapered optical fiber probe tip (100 nm aperture), as shown in Figure 14. A nano-positioning stage allowed for ultrafine lateral scanning of regions of interest. The distance between the tip and the sample surface remained constant under 100 nm by feedback control of a shear force detection system based on a quartz crystal tuning fork (resonance frequency of 32.768 kHz). The collection part of the setup (with a low NA objective and a single channel PMT detector) is a wide field collection. The spatial resolution of light injection results from the point-by-point scanning of the surface sample with the tapered optical fiber tip. Two wavelengths were considered, at 405 nm and 632.8 nm, to respectively achieve resonant and non-resonant evanescent coupling of the non-radiating light field from the output of the tapered optical fiber tip into free-optics propagation in the glass substrate.

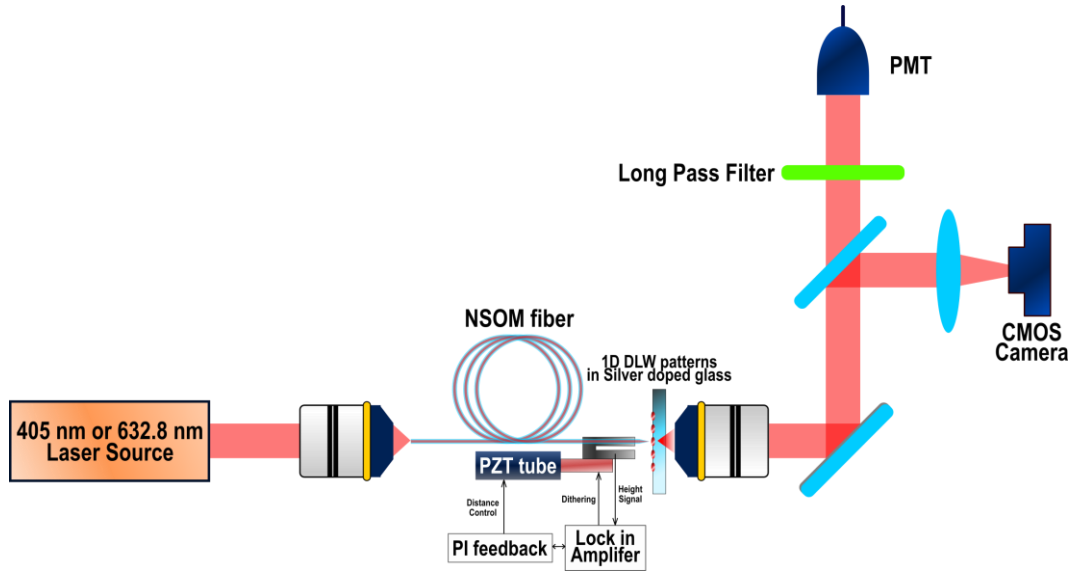


Figure 14 Experimental set-up of Near-field Scanning Optical Microscope in illumination mode, with light injection from a tapered optical fiber probe tip (100 nm aperture). 2 laser sources, objective lenses (focusing (20x, 0.40NA) and imaging (40x, 0.60NA)), long pass filter, and single channel photomultiplier detector (PMT).

### 3. 3 NSOM Results and discussion

During NSOM experiment, the feedback control on the shear force positioning system showed no surface height modification as shown in Figure 15(a, b) while scanning a laser induced structure, indicating a truly flat surface at the structures after polishing, which excludes any topological artifact. Indeed, by injecting a laser diode excitation source at 405 nm and collecting light above 435 nm after a long-pass filter (Edmund GG-435), the high-resolution image of the transverse distribution of fluorescent silvers at the surface was

obtained (see Figure 15(b)). The horizontal cross section along the diameter of the fluorescent tubes is given by Figure 15 (c) (green curve). Similar to confocal fluorescent imaging (not shown here), NSOM shows the clear annular distribution of silver clusters, the larger fluorescence pedestal coming from the concomitant excitation and fluorescence collection from planes below surface.

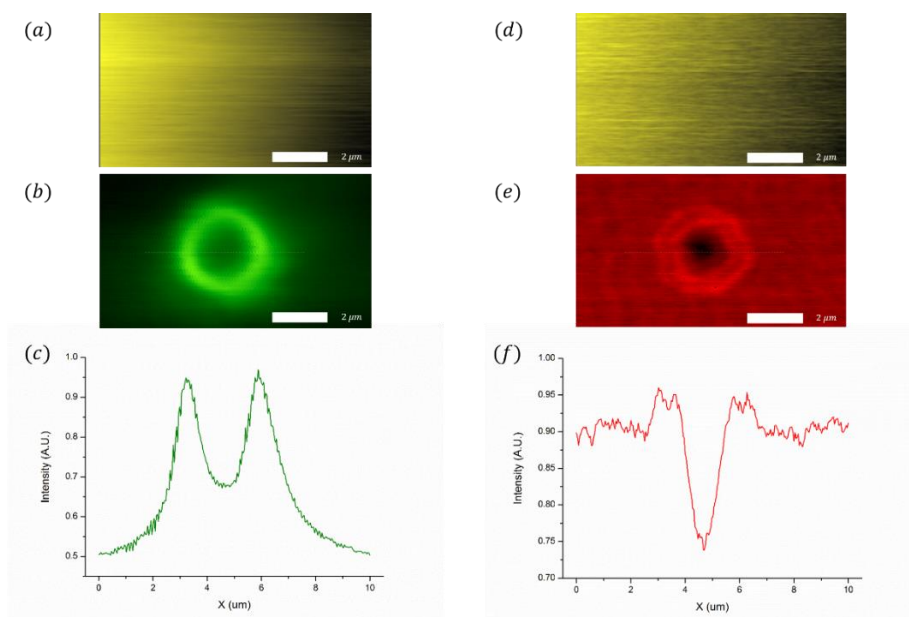


Figure 15 (a, d) Image of surface topology obtained from NSOM in illumination mode; (b, e) Image of near field optical signal obtained by NSOM when the silver species are excited by 405 nm laser diode and 632.8 nm He-Ne laser; (c, f) Associated line profiles through center of ring-shape silver cluster

While injecting a He-Ne laser source at 632.8 nm and collecting light with a long-pass filter (665 nm, Edmund RG-665), the NSOM image (Figure 15(e)) led to a non-zero background signal and a weakly brighter double-ring distribution (6% increase) that typically matches the position of the fluorescent ring image from Figure 15(b), and to a darker distribution (17% decrease) inside the annular silver cluster distribution (Figure 15(f),

red curve). Similar NSOM image had also been obtained while collecting without the RG-665 long-pass filter: since the fluorescence excitation of both the randomly distributed Ag<sup>+</sup> ions and the 3D localized silver clusters is extremely weak while excited at 632.8 nm [49], we thus believe that measurements (Figure 15(e) and Figure 15(f), red curve) are mostly from the 632.8 nm residual background, after the non-resonant evanescent coupling.

NSOM image with the He-Ne injection remarkably gave access to new insight concerning the laser-induced silver-mediated material modification, comparatively to the UV-excited counterpart. The proposed interpretation of the observed spatial distribution at 632.8 nm (Figure 15(e) and Figure 15(f)) is that it corresponds to a direct image of the local redistribution of silver element (ions and clusters) after DLW, as discussed hereafter. First, our phosphate glass typically shows a linear correlation between the refractive index of non-structured bulk samples and their silver content. Second, several reports evidence of the laser-induced migration of silver elements over mesoscopic scales (larger than 100 nm) during laser irradiation: *Bellec et al.* have shown by high-resolution electron scanning microscopy the enhancement of silver elements correlatively located at the position of the silver clusters [33]; by chemical analysis from electron microprobe, *Desmoulin et al.* have observed the partial depletion of the silver reservoir (about 10-20%) in the center of laser-induced silver-based annular structures (same structures as those of the present study) [50]; *Marquestaut et al.* have reported by back-scattered electron scanning microscopy that the created silver cluster distributions could further be thermally developed into 3D-localized plasmonic metallic silver nanoparticles [51]; Third, local index change can result from both a local density change and/or the local creation of new polarizable chemical bounds (as occurring for the creation of silver clusters). *Abou Khalil et al.* recently reported

the direct correlation between spatial distributions of silver clusters and associated refractive index change [43]. Thus, light interaction at 632.8 nm with silver elements is mostly non-resonant. Any correlation between a local index change and the 3D distribution of silver elements can mostly be related to density aspects, thus to the local of silver element concentration (ions and clusters). Thus, non-resonant NSOM coupling efficiency appears as directly depending on the local refractive index experienced by the light field in the sub-wavelength regime at the glass surface, at the output of the tapered optical fiber tip. Thus, it directly depicts the spatial redistribution of silver elements (silver ions and clusters), as shown in Figure 15(e) and Figure 15(f).

### **3. 4 Simulation and result**

Remarkably, the NSOM experience at 632.8 nm seems to be the first direct optically-based imaging (instead of electron beam approaches [33,50,51]) of the laser-induced reservoir depletion of silver ions and silver element redistribution. Although qualitative, the NSOM method appears as a unique imaging approach since it provides a great sensitivity to local composition dependences, while the chemical micro-probe analysis (although fully quantitative) generally shows a limited sensitivity of 1 – 2 %: *Desmoulin et al.* had seen only the reservoir depletion of silver ions, but not the creation of silver clusters (see Figure 16 from [50]). Consequently, NSOM and electron microprobe appear as highly complementary tools.

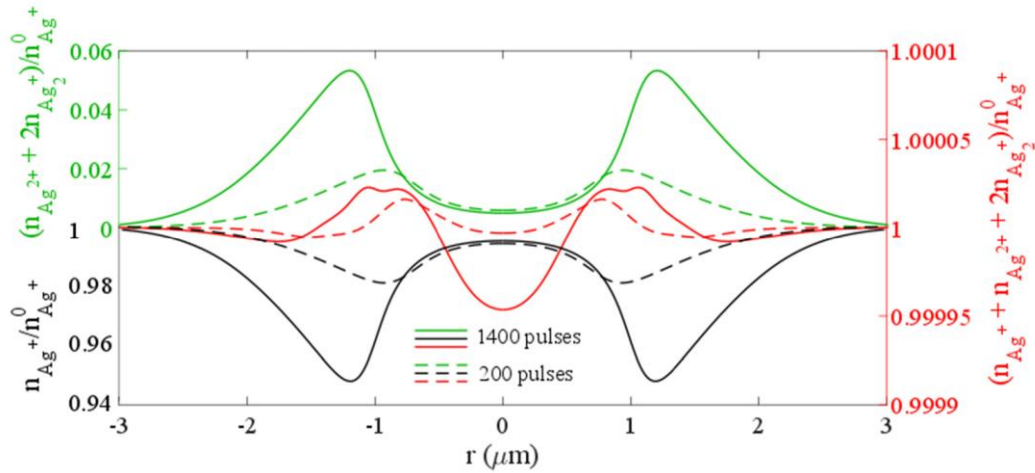


Figure 16 Numerical modeling of the laser-induced redistribution of silver species (8.8 TW/cm<sup>2</sup>, N<sub>pulse</sub> = 200 or 1400), showing the profiles of the silver ions (black line), the induced silver cluster and hole centers (green line), and all of silver species (red line).

To support the interpretation of non-resonant NSOM, numerical investigations were performed with our multi-scale multi-pulse multi-physics numerical model of laser-activated silver ion migration and photochemistry [38], considering similar laser irradiation parameters and silver-containing glass (intensity = 8.8 TW/cm<sup>2</sup>, N<sub>pulses</sub> = 200 or 1400, beam radius at the focal plane  $r_0 = 2.5 \mu\text{m}$ ). The full calculated redistribution of silver species was extracted, including the silver ions ( $\text{Ag}^+$ ), the induced silver clusters ( $\text{Ag}_2^+$ ) and the remaining hole centers ( $\text{Ag}^{2+}$ ). Figure 16 shows the normalized calculated silver element distributions: the  $\text{Ag}^+$  ions (black curve), the total silver elements (red curve:  $n_{\text{Ag}^+} + n_{\text{Ag}^{2+}} + 2n_{\text{Ag}_2^+}$ ), and the induced clusters and holes (green curve:  $n_{\text{Ag}^{2+}} + 2n_{\text{Ag}_2^+}$ ). The numerical model obeys the overall conservation of silver elements. The  $\text{Ag}^+$  distribution (black curve) shows both the central  $\text{Ag}^+$  depletion due to their radial outward diffusion, but also their reduction at the periphery of the irradiated spot by chemical consumption to create the silver clusters (as observed also with the red curve of silver cluster and hole distributions). Still, the overall

silver element distribution (red curve) confirms both the central depletion due to ion migration and the accumulation at the periphery due to the chemical precipitation and stabilization with silver clusters. Such silver element distribution (red curve of Figure 16) remarkably matches the 1D cross-section of the He-Ne injected NSOM experiment (Figure 15(e)), especially for  $N_{\text{pulses}} = 1400$ . The silver element redistribution (Figure 16, red curve) shows a slightly smaller ring diameter than that of the simulated silver clusters (Figure 16, green curve), possibly corresponding to the non-resonant NSOM double-ring structure (Figure 15(c), red curve). This corroborates the interpretation of the NSOM approach, strengthening our description of laser-activated mechanisms of silver-containing glasses in an athermal regime.

To go further, spatially-distributed etching rates have been investigated, by correlatively considering the spatial distribution of silver elements from micro-probe measurements [9] and the present NSOM data. Figure 17(a) depicts the experimental surface morphology of the laser-modified area revealed after 6 minutes soft etching with deionized water (blue curve, from [50]). Spatial etching rate distributions have been designed (Figure 17(a), green curve) [52], so that the simulation of the associated simulated etching process leads to a surface profile (Figure 17(a), red curve) in very good agreement with the experimental surface profile (Figure 17(a), blue curve). The optimized etching rate profile shows the normalized behavior of the pristine glass at the periphery of the laser-modified area (typically corresponding to 0.22 nm/s for the considered soft etching conditions). At the position of silver clusters, the etching rate strongly drops by a factor of 20.6, corresponding to a chemically hardened area of the laser-modified glass. Between the silver cluster localization, the etching rate shows a Gaussian-like distribution (FWHM =

310 nm), with central and pedestal values being 2.5 times larger and 1.8 times smaller, respectively, than that of the pristine glass. This shows a very strong chemically-sensitive material modification highly located in the center of the laser irradiation, with non-trivial etching sensitivity distributions. Figure 17 (b) provides then the comparison of such etching rate distribution (green curve) with the micro-probe measurement of the silver element distribution (blue curve, from [43]) and the present non-resonant NSOM measurement interpreted as the refractive index spatial distribution (red curve), independently revealing the presence of the three same laser-affected areas.

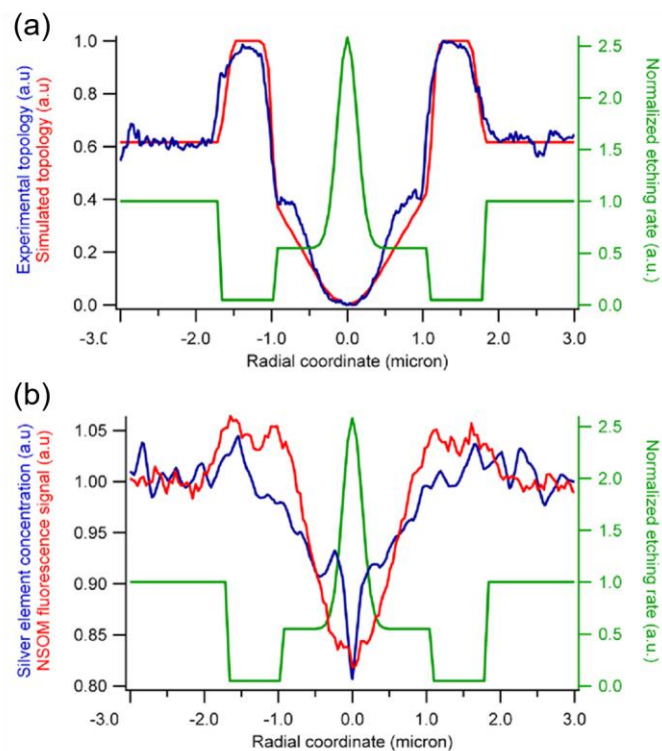


Figure 17 (a) Experimental topological profile (blue curve) and simulated etching-induced topological profile (red curve) adjusted by optimizing the normalized etching rate distribution (green curve). (b) Silver element distribution by micro-probe measurement (blue curve, from [9]) and NSOM measurement (red curve, from Figure 16 (d)) with respect to the optimized normalized etching rate distribution (green curve).

Indeed, the NSOM measurements of silver element accumulation and cluster creation correlate with a very low etching rate (radius between 1 to 1.8  $\mu\text{m}$ ). Moreover, the silver reservoir depletion is independently shown by NSOM and electron micro-probe. Finally, the estimation of a very strong on-axis etching rate (240 nm, FWHM, green curve) corroborates the very narrow on-axis silver depletion (sub-200 nm, FWHM, blue curve), which may even be seen in the on-axis NSOM trace (red curve). Thus, laser-induced index change distributions [43] as well as the spatially-distributed etching rate depend here on the local concentration and nature of silver species [28], and on additional glass matrix rearrangements such as release of molecular oxygen to ensure charge compensation and material stabilization, as reported in thermal poling [53] or for glass irradiations in a thermal regime [54].

### **3. 5 Conclusion**

In conclusion, we have reported for the first time the correlative description of laser-induced silver redistribution in terms of chemical micro-probe, NSOM and numerical modeling. The results significantly strengthen the understanding of material modifications in such glasses in a non-thermal interaction regime. In particular, it has been found that the spatial distribution of species in silver-containing glasses produced by femtosecond laser irradiation has a significant effect on chemical etching selectivity. This should help for future

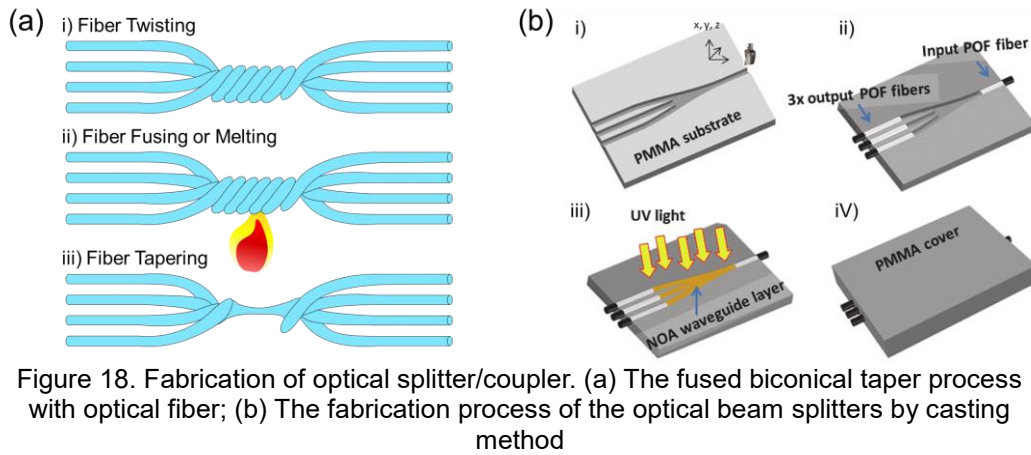
development of nanoscale surface chemical patterning, such as for 2D photonics crystal applications [55].



## **Chapter 4. 2-dimensional DLW and application**

### **4.1 Introduction**

Research on Direct Laser Writing (DLW) with glass samples, especially fused silica, has been actively conducted for decades. In particular, type I modification induces a smooth refractive index change of glass which results from the formation of color center [56–58], and/or the change of the density [59,60], it is appropriate to use it as a method of manufacturing waveguides. In general, to manufacture optical fibers, optical glass is transformed into an extremely pure preform glass cylinder by modified chemical vapor deposition (MCVD) method. Then, when the preform blank cools down, it goes through quality control testing. Lastly the optical fiber is manufactured via a fiber drawing tower. The optical fiber is used to manufacture the optical communication devices such as splitter and coupler, as shown in Figure 18(a). And polymer devices with a size larger than the mm scale are made through a step-by-step cast method as shown in Figure 18(b) [61]. But these method requires many steps and a lot of time, and has a limitation in the dimension of the device.



Direct laser wiring can be an alternative to overcome the limitations of conventional optical device manufacturing. This method, shown in Figure 19, can produce optical fibers and structures in a very short time and extend the optical device to 3-dimensional as well as 2-dimensional. This method also allows micromachining up to several hundred nm. These advantages have high usability in optical devices using transparent substrates and are likely to be connected to industry.

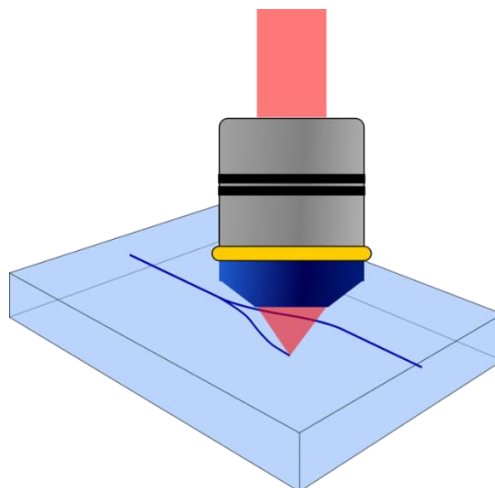


Figure 19. Schematic for optical device fabrication through Direct Laser Writing (DLW)

This chapter will introduce the study of two-dimensional waveguides produced by Type A modifications in silver containing zinc phosphate glass. In particular, the fabrication, performance and characteristics of symmetric Y-junction and asymmetric Y-junction will be covered. Asymmetric Y-junctions were fabricated by carving the two branches with different irradiance and the output ratios were measured. We confirmed that asymmetric optical splitters with various output ratios can be fabricated by using DLW in silver containing glass. We believe our results could suggest ways to fabricate 3D integrated circuits and optical devices with Direct Laser Writing.

## **4.2 Experimental Methods**

### **4.2.1 Type A DLW for waveguide**

Type A DLW in silver containing glass allows the center to be photo-dissociated, bringing the peripheral deformation of the ring-shape as in chapter 3. At this time, two-dimensional (2D) structures can be created by moving the sample mount. In this case, the 1D ring-shape pattern is extended to a 2D narrowly spaced double line, as shown in Figure 20 [43]. The thickness of this double line is changed according to the laser irradiance and the writing speed [38]. The structures fabricated in this paper usually have a thickness of less than 2  $\mu\text{m}$ .

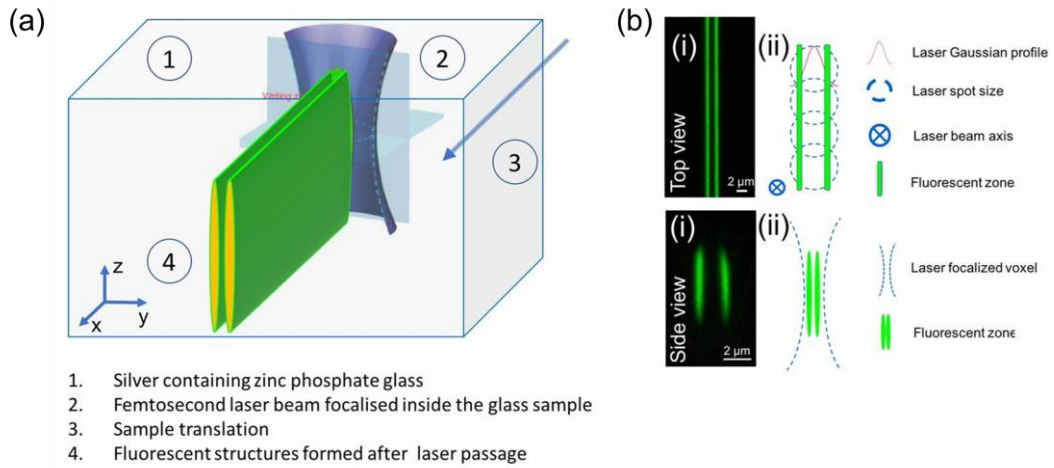


Figure 20. (a) Schematic image showing 2D structure fabrication with type A modification; (b) Top and side view of fabricated 2D structure [38]

Alain A. KHALIL compares the refractive index changes of the waveguides produced by type I DLW and type A DLW as shown in Figure 21 [41]. He gave optical path difference (OPD) profiles for two following variables, the laser pulse energy and the writing speed. Figure 21(a) shows the optical path difference of a type I waveguide and Figure 21(b) shows the OPD of a type A waveguide. Figure 21(1) shows the white light image and fluorescence image for the top/side view of the both waveguides. Figure 21(2) shows the case where the laser pulse energy is fixed and the writing speed is changed, and Figure 21(3) the writing speed is fixed and the laser irradiance is changed. Type I waveguides made with pulse energy below 1 uJ have a negative index change with or without a center pick. On the other hand, type A waveguide always has a positive index change. Therefore, type A DLW in silver containing glass has a suitable condition for manufacturing typical waveguide.

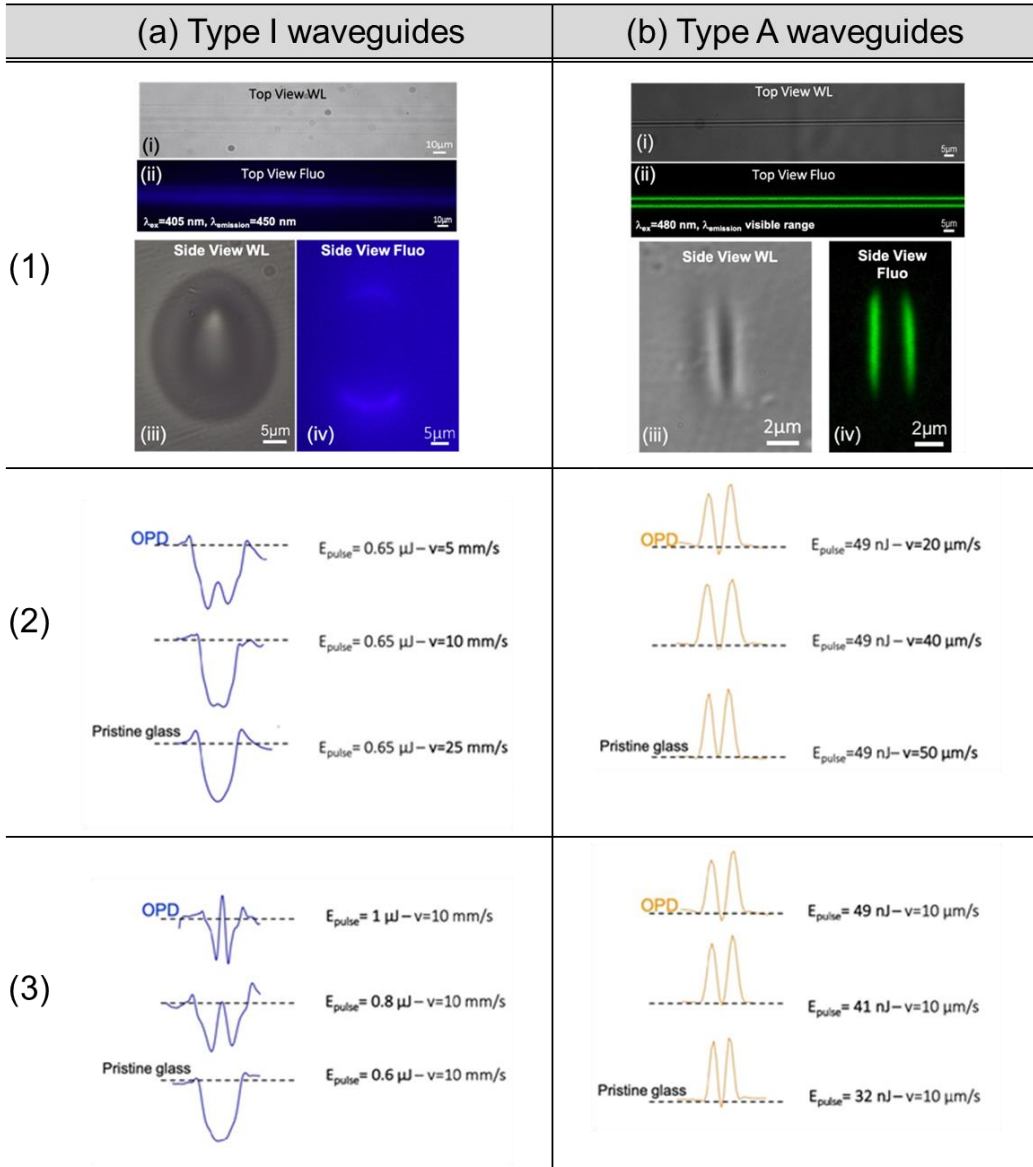


Figure 21. (a) Type I waveguide and (b) type A waveguide. (1) The image of Top/Side view of DLW pattern for both type. Various Optical path differences profiles for two types as a function of (2) laser pulse energy and (3) writing speed.

## 4.2.2 Preparation of samples

The silver containing zinc phosphate glass used in this chapter has the following molar composition.  $\text{PZnGa}_{5.5}\text{-Ag}_{5.5}$ , [p]: 52.7 %, [Zn]:36.3 %, [Ga]: 5.5 %, [Ag]: 5.5 %. This glass sample was developed and manufactured by Institut de Chimie de la Matière Condensée de Bordeaux (ICMCB) and sensitively forms silver clusters by femtosecond laser irradiation at 1030 nm. Figure 22 shows the characteristics of these glasses sample that both the radius of the ring-shaped DLW pattern (Figure 22(a)) and the refractive index change (Figure 22(b)) increase as the writing laser's irradiance or number of pulses increases [38,43].

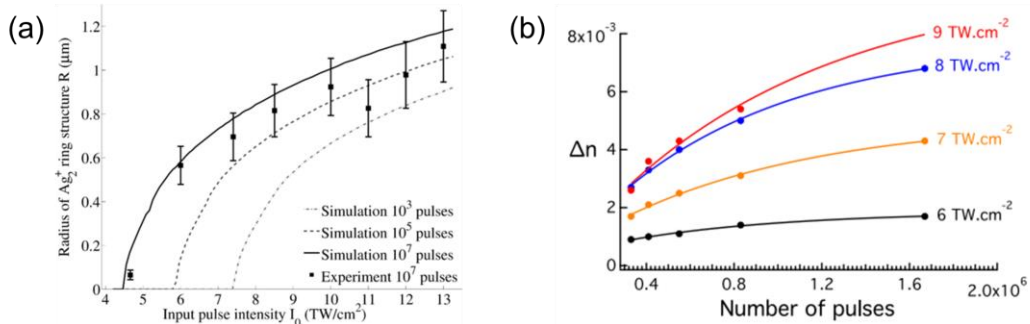


Figure 22. Experimental/theoretical relationships between (a) the radius of  $\text{Ag}_2^+$  ring structure and number of pulses/laser irradiance, (b) refractive index change and number of pulses/laser irradiance

## 4.2.3 Fabrication of Y-junction

To fabricate the Y-junctions, Yb:KGW femtosecond-laser (9.8 MHz repetition rate, 390 fs pulse(FWHM) and wavelength at 1030 nm) and Zeiss air objective (20 $\times$ , NA = 0.75) were

used. The irradiance of the laser beam incident on the sample was controlled through an Acousto-Optic Modulator (AOM). As mentioned in the previous chapter, the irradiance of the laser beam determines the radius and index change of the silver cluster, which can be utilized to fabricate symmetric and asymmetric Y-junctions. In this experiment, the voltage applied to AOM was set to have a constant 0.1V interval between 0.6V and 1V. The irradiance in the focal plane of the objective lens is shown in the following table.

<b>Voltage applied to the AOM device (V)</b>	<b>Irradiance in the focal plane of an objective lens (TW/cm<sup>2</sup>)</b>	<b>Irradiance ratio</b>
0.60	9.693	0.69
0.70	11.57	0.83
0.80	13.03	0.93
0.90	13.52	0.97
1.0	14.01	1.0

Table 2. The relation between voltage applied to the AOM and Irradiance in the focal plane of an objective lens

Y-junction, a two-dimensional optical device, is made of two s-bends with flip symmetry, as shown in Figure 23. One S-bend has a length of 6mm and consists of four parts. Part 1 is straight waveguide, the section from the input to the curve before. Part 2 is the section where two waveguides are coupled and is an arc of a circle with a radius of 150 mm and a height of 12.5  $\mu\text{m}$  to minimize curvature loss of waveguide. Part 3 is an arc with the same specifications as part 2, but the center of curvature is at the bottom. This section is intended to guide the split beam to the output after the coupling is completed. Finally, part 4 is the section from the end of curve to the output, and the outputs of two s-bend is 50  $\mu\text{m}$  apart. These Y-junctions were made through two writings, the upper branch and the lower branch.

In the writing process, the symmetric Y-junction was fabricated by setting the irradiance and writing speed of the two branches identically, and the asymmetric Y-junction was produced by fixing the writing speed and varying the irradiance. The symmetric Y-junction was produced with a writing speed of 0.1 mm/s and an irradiance of 14.01 TW/cm<sup>2</sup>. In the case of asymmetric Y-junction, the upper branch was fixed with irradiance of 14.01 TW/cm<sup>2</sup>, and the irradiance of lower branch was set to the irradiance of 13.52 TW/cm<sup>2</sup>, 13.03 TW/cm<sup>2</sup>, 11.57 TW/cm<sup>2</sup>, and 9.693 TW/cm<sup>2</sup>. This other irradiance allows the asymmetrical waveguide to be manufactured by varying the width of the branch double line and the degree of refractive index change. N. Syafiqah Mohamed-Kassim fabricated and simulated a large scale asymmetric Y-junction by making branch sizes different [62].

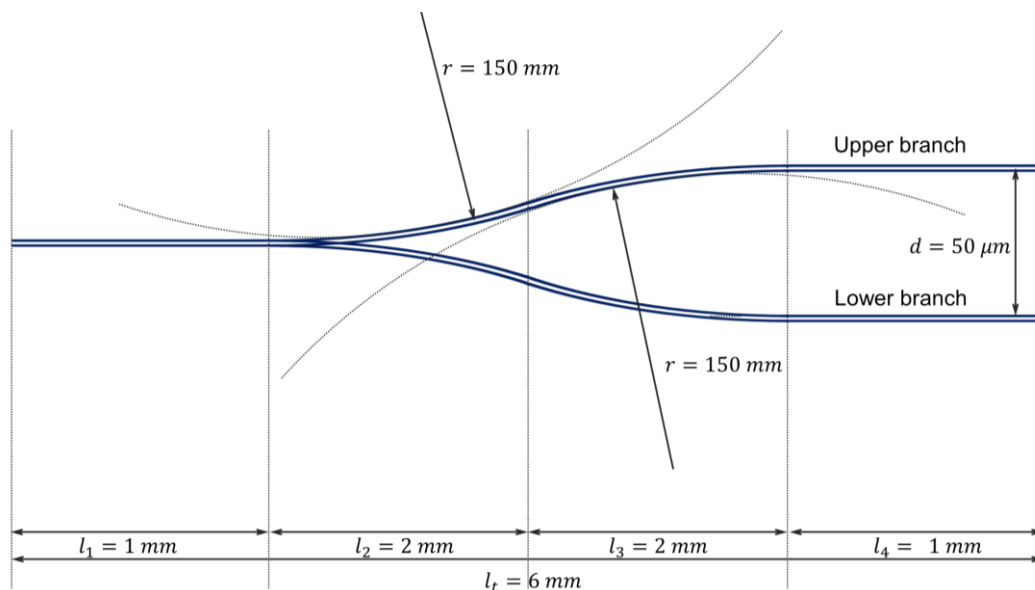


Figure 23. Structure schematic of Y-junction.;  $l_t$ : total length of Y-junction,  $l_1$ : The length from the input to the point where it is divided into two branches,  $l_2, l_3$ : Length of curved part with curvature of 150mm, and  $l_4$ : Length from the end of the curve to the output

#### 4.2.4 Measurement of output and optical path difference

In order to measure the output of the fabricated symmetric/asymmetric Y-junctions, the experimental setup is shown in Figure 24. The resulting waveguide was mounted on a nano-stage (PI company, P-611.3 NanoCube®, XYZ piezo system) with a resolution less than 1 nm. Since our type A DLW induces silver clusters with double lines, measured the output variation by changing the inject position in the vertical direction of the double line using the nano-stage. The laser beam was injected into the Y-junction input using a 20X, 0.40NA objective lens. The output intensity was measured using a 40X, 0.60NA objective lens, CCD camera, and beam profiler.

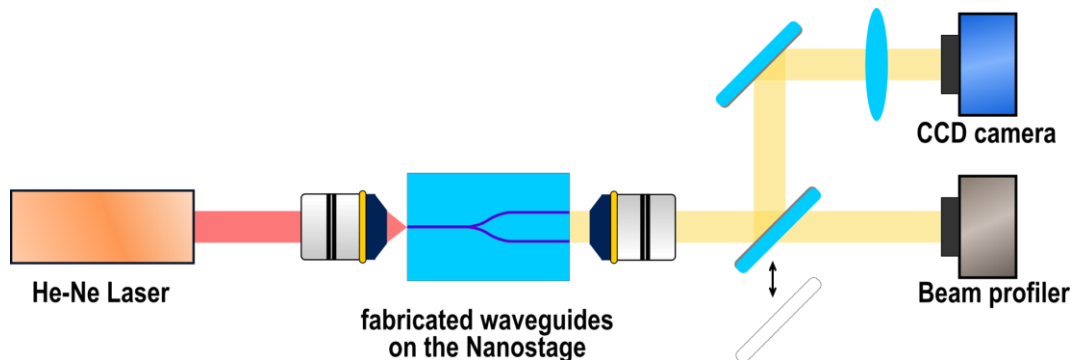


Figure 24. Experimental setup to measure the output of the Y-junction

The optical path difference (OPD) was measured by using wave front sensor (PHASICS Inc., SID4-HR GE) with a phase resolution of 1 nm and 100X, 1.30 NA oil objective lens (Zeiss, Plan-Neofluar). And the refractive index change was calculated using the measured OPD.

## 4.3 Result and discussion

### 4.3.1 Symmetric Y-junction

The output of symmetric Y-junction fabricated under the same conditions in the upper and lower branches was measured. Since the mode of the output beam changes a lot according to the injection coupling between input and laser beam, the experimental setup was made to maintain a single mode. Type A DLW has a total of four outputs since it induces a double line in one waveguide. In general, coupling occurs between two waveguides at close distance. However, double lines are considered to be an output because they have a spacing of less than  $2\ \mu\text{m}$ . This double line acts like a waveguide and is believed to be an effective single line rather than a coupling. Figure 25 shows the output shapes and output profile of symmetric Y-junction. It was confirmed that the incident laser beam was divided with a ratio of 51.30% and 48.70% at the end of two effective outputs.

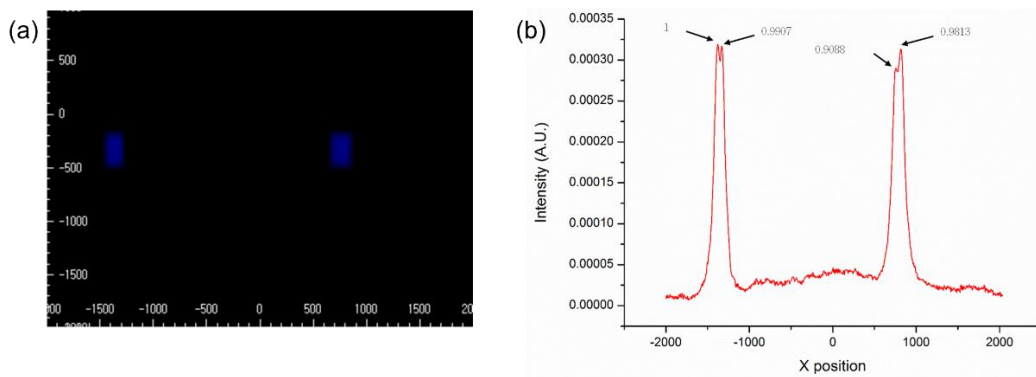


Figure 25. Output image and profile line of symmetric Y-junction

Since the waveguide fabricated with type A DLW is not a single circular waveguide, the output power and output ratio were tracked by moving the injection position vertically to the double line, as shown in Figure 26. Here the output power and ratio vary depending on the injection position while maintaining a single mode. Figure 26(b) shows how the total power for the injection position of the laser beam changes with interval of 200 nm. It has a shape similar to the Gaussian distribution of a He-Ne laser beam. A 20x, 0.40NA injection objective lens was used, and this lens has a beam waist of about 1.9  $\mu\text{m}$ . Figure 26(c) shows the tendency for the output ratio of the upper branch to change according to the transition of the injection position. This graph shows that the output ratio can vary from 20% to 75% as the injection position shifts. Also, at the incident position with the highest total power, the output has a ratio of about 40% - 60%, not 50% - 50%.

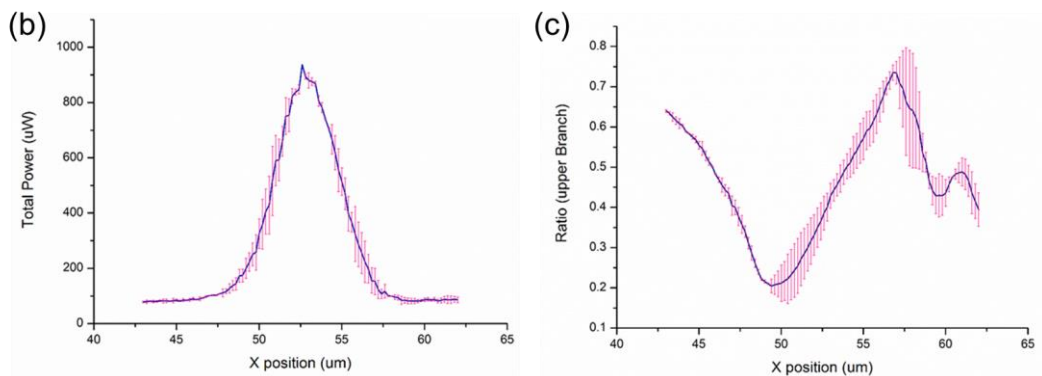
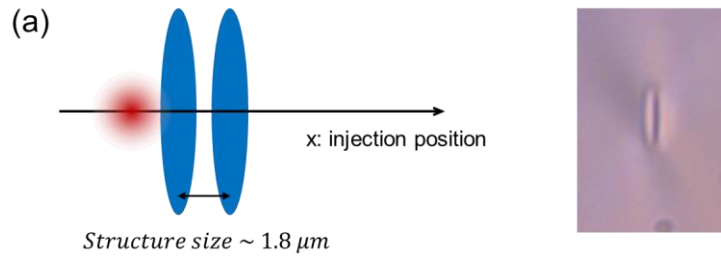


Figure 26. (a) A white light image of the input of a waveguide made of Type A DLW; (b) the relationship between injection position with 200 nm interval and total power; (c) variation of output ratio for injection position

### 4.3.2 Asymmetric Y-junction

Unlike symmetric Y-junction, where two branches were written by using the same irradiance, the upper branch was fabricated by fixing high irradiance and the lower branch by changing irradiance as shown in Figure 27. The upper branch is engraved from the input to the end of the output with an irradiance of 14.01 TW/cm<sup>2</sup>, and the lower branch is once again engraved from the input to the end of the output with irradiances of 13.52 TW/cm<sup>2</sup>,

13.03 TW/cm<sup>2</sup>, 11.57 TW/cm<sup>2</sup>, and 9.69 TW/cm<sup>2</sup>. At this time, the  $l_1$  part was overwritten with two different irradiances.

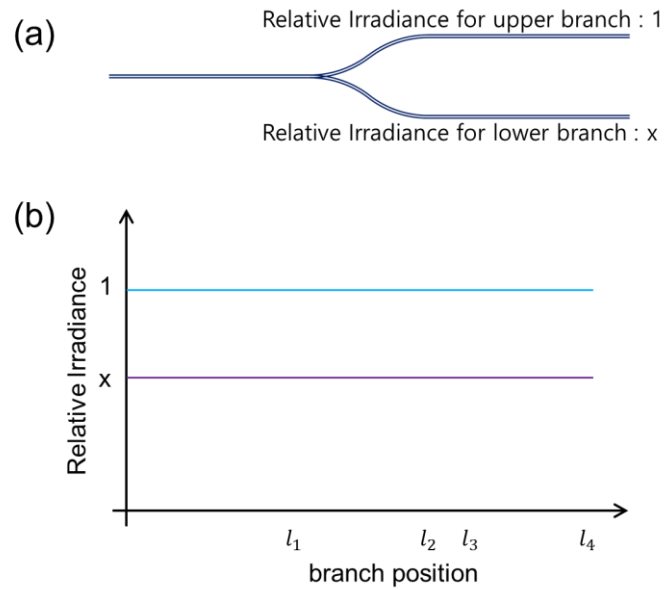


Figure 27. Shape of asymmetric Y-junction and applied irradiance for each branch

In this paper, four different asymmetric Y-junctions were fabricated and the output was measured. The total power and output ratio of asymmetric Y-junction were measured for the injection position at the same time. Then, Gaussian fitting was performed on the total power, and the point with the strongest output power was obtained. In Figure 28(a), the position was defined as injection position = 0 and the output ratios at the lower branches for different splitters are shown. The slope at the point where injection position = 0 is different for each Y-junction, which is considered to be related to injection coupling. The output profiles when the injection position is 0 are shown in Figure 28 (b). For each case, the split ratios are 43%-57%, 33%-67%, 27%-73%, 22%-78%, and 4%-96%. In this paper,

four beam splitters were fabricated, but it can be seen that different asymmetric beam splitters can be made by adjusting irradiance differently.

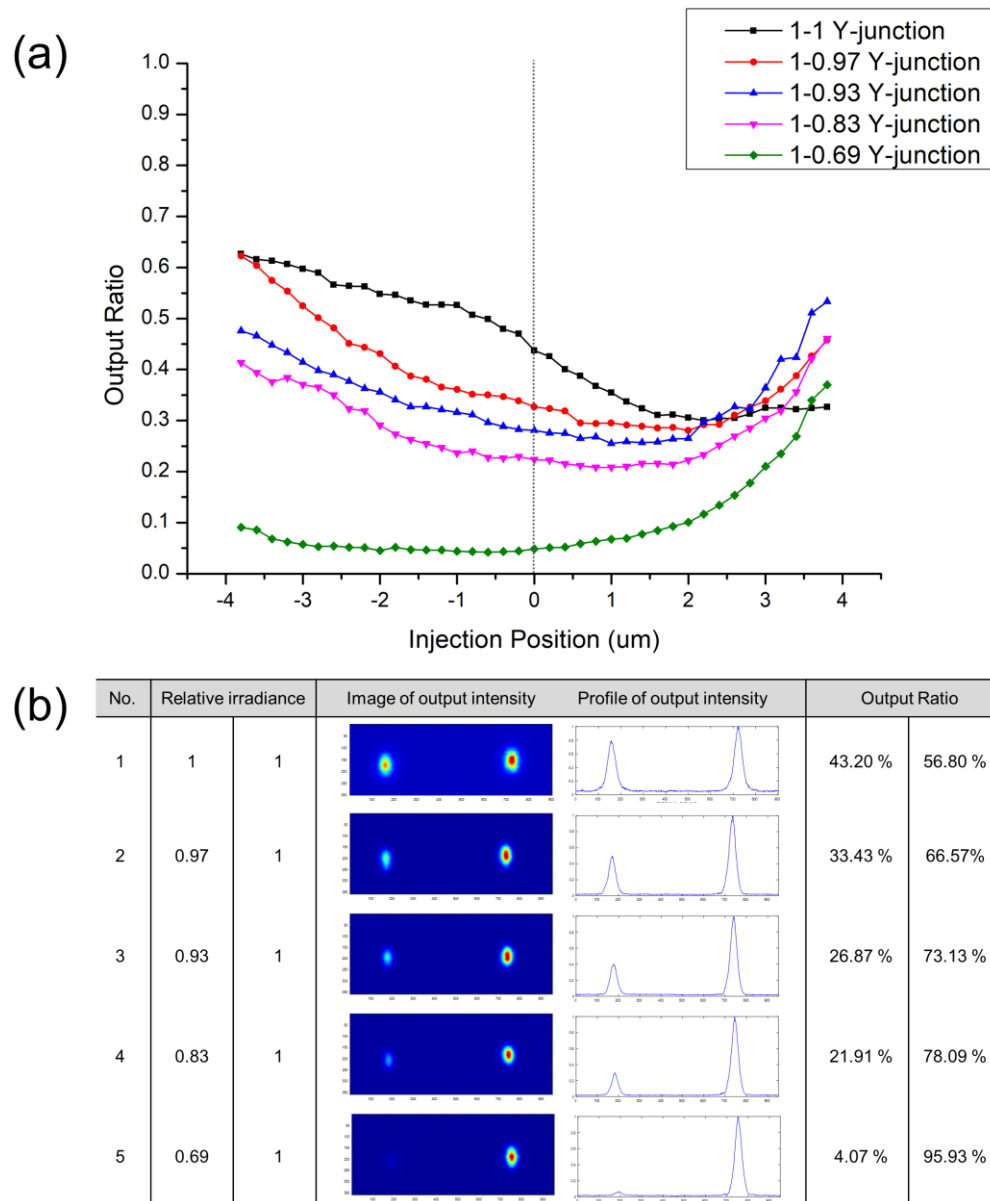


Figure 28. (a) Changes of output ratios of lower branch according to injection position for different asymmetric Y-junctions; (b) Output profiles and output ratios for one symmetric and four asymmetric beam splitter, when injection position = 0

As shown in Figure 29, refractive index changes ( $\Delta n$ ) of one symmetric Y-junction and four asymmetric Y-junctions made through type A DLW was measured by using a wave front sensor. When the irradiance was  $14.01 \text{ TW/cm}^2$ , a modification induces an average index change of  $5.1 \times 10^{-3}$ . The index changes decrease as the laser irradiance decrease. There was an index change of  $4.8 \times 10^{-3}$  when the irradiance was  $13.52 \text{ TW/cm}^2$ . An index change of  $4.4 \times 10^{-3}$  when the irradiance was  $13.03 \text{ TW/cm}^2$ . An index of  $2.9 \times 10^{-3}$  when the irradiance was  $11.57 \text{ TW/cm}^2$ . And when Irradiance was  $9.693 \text{ TW/cm}^2$ , there was an index change of  $2.7 \times 10^{-3}$ . In addition, as laser irradiance decreases, the spacing of the double lines decreases as follows.  $2.44 \text{ }\mu\text{m}$ ,  $2.22 \text{ }\mu\text{m}$ ,  $2.00 \text{ }\mu\text{m}$ ,  $1.78 \text{ }\mu\text{m}$ , and  $1.56 \text{ }\mu\text{m}$ .

Irradiance ( $\text{TW/cm}^2$ )	average Index change ( $\Delta n$ )	Thickness of double line ( $\mu\text{m}$ )
14.01	0.00509	2.44
13.52	0.00475	2.22
13.03	0.00435	2.00
11.57	0.00290	1.78
9.693	0.00270	1.56

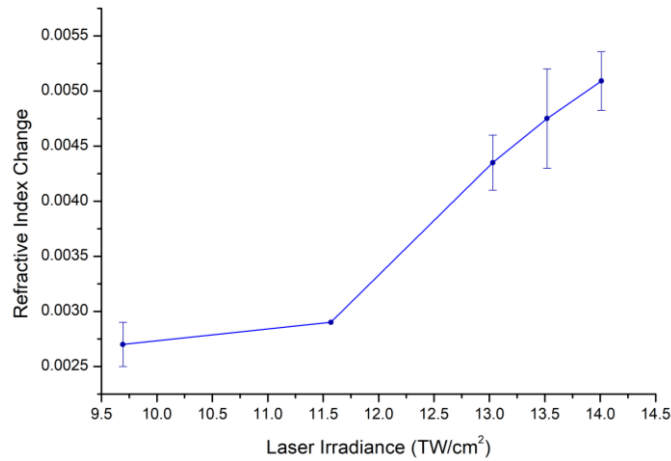


Table 3. Refractive index change and thickness of double line according to the laser irradiance.

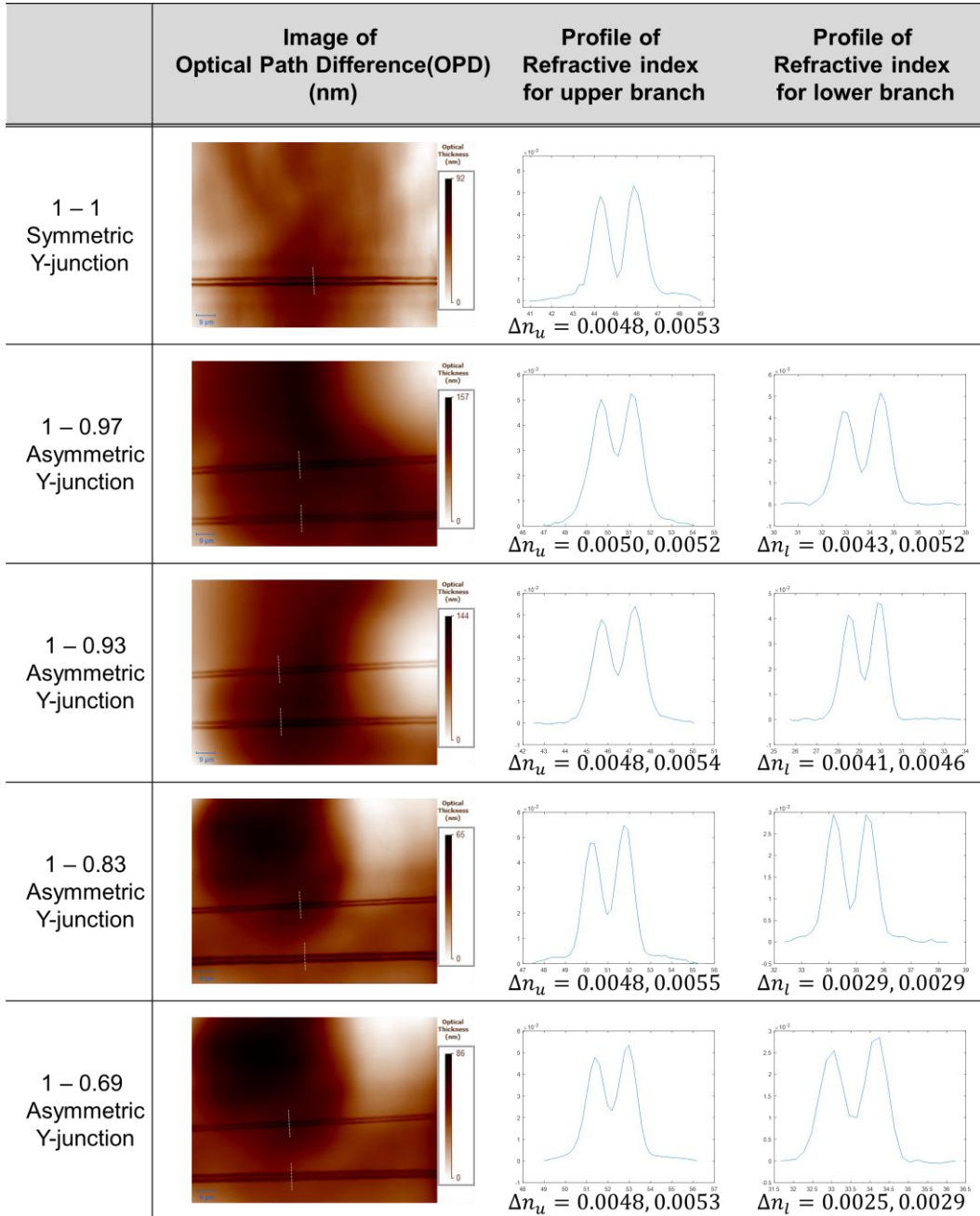


Figure 29. Index changes and profiles for one symmetric Y-junction and four asymmetric Y-junctions

### 4.3.3 Modified asymmetric Y-junction

A modified asymmetric Y-junction in a different form from the asymmetric Y-junction produced in the previous chapter was designed and written as shown in Figure 30. In the existing asymmetric Y-junction, the part from input to  $l_1$  was overwritten, but in the new asymmetric Y-junction, it was engraved only once in this section. In the modified asymmetric Y-junction, irradiance in the section where coupling between two waveguides occurs is fabricated under the same conditions as the asymmetric Y-junction. But in order to make the output size of the upper branch and that of the lower branch same at the end of Y-junction, the writing irradiance was increased from  $l_1$  to  $l_4$  in three steps as shown in Figure 30(b).

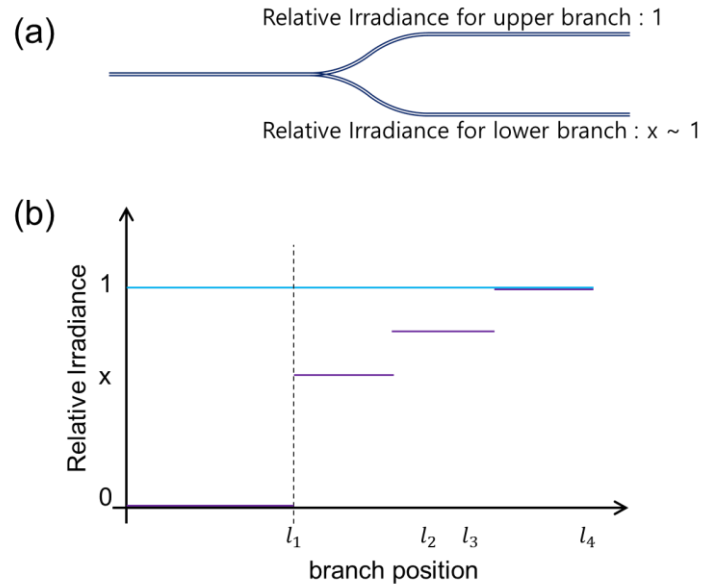
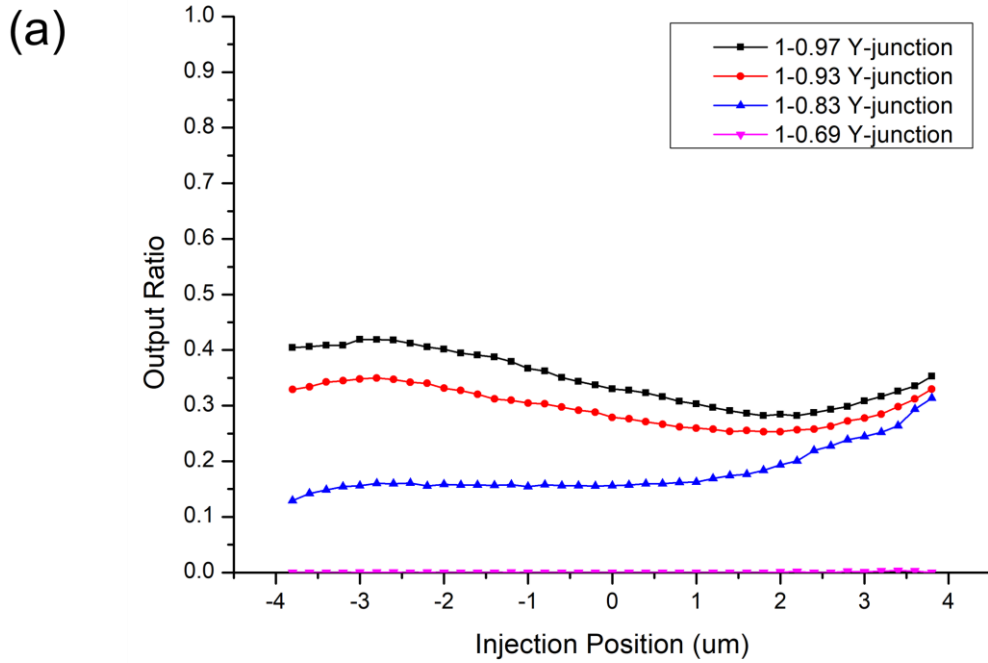


Figure 30. Shape of modified asymmetric Y-junction and applied irradiance for each branch.

The modified asymmetric Y-junction made in this way has the result of outputs, as shown in Figure 31. In Figure 31(a), the slope of output ratio for lower branch is similar to the previous asymmetric Y-junction. And it is also confirmed that the output ratio has almost similar results except 1-0.69 Y-junction. (The output shape is damaged due to some scratches on the surface of 1-0.69 modified asymmetric Y-junction) Figure 31(b) shows that 1-0.97 asymmetric Y-junction has an output ratio of 33% - 67%, 1-0.99 asymmetric Y-junction has an output ratio of 28% - 72%, 1-0.83 asymmetric Y-junction has an output ratio of 16% - 84%, and 1-0.69 asymmetric Y-junction shows that it has an output ratio of 0% - 100%.

Compared to the previous asymmetric Y-junction, it is found that the modified asymmetric Y-junction has a more gradual curve. That means that modified asymmetric Y-junctions have less sensitive dependence of output ratio with respect to inject position. And when it is used, it has a less limitation of the incidence position.



(b)

No.	Relative irradiance	Image of output intensity	Profile of output intensity	Output Ratio		
1	0.97	1			33.02 %	66.98 %
2	0.93	1			27.90 %	72.10 %
3	0.83	1			15.61 %	84.39 %
4	0.69	1			0 %	100 %

Figure 31. (a) Changes of output ratios of lower branch according to injection position for four modified asymmetric Y-junctions; (b) Output profiles and output ratios for four modified asymmetric beam splitter, when injection position = 0

#### 4.3.4 Near field injection with NSOM fiber tip

In the previous chapter, the laser beam was injected into the input of the waveguide by using 20X, 0.40NA objective lens. In this case, the focused beam has spot with a diameter of about 2 $\mu$ m. Meanwhile, the double line of our waveguide is spaced from 1.56  $\mu$ m to 2.44  $\mu$ m depending on the laser irradiance. One of the double lines has a thickness of about 600 nm.

As shown in Figure 32(a), laser beam was injected into only one of the double lines by using the illumination NSOM mode. The NSOM fiber (LovaLite company, E50-SM600-AI500-2, pulled type NSOM tip) has an aperture of 500 nm that is slightly smaller than the thickness of the waveguide, and is coated with Al and Cr with a thickness of 50 nm. In the illumination mode, the NSOM fiber tip has a large diffraction due to the small aperture size. So the distance from the end of fiber to the entrance of the Y-junction was maintained to be less than 100 nm with feedback system of NSOM.

Figure 32(b, c) is a graph showing the output ratio when incident on the symmetric Y-junction, and Figure 32(d, e) is a graph showing the output ratio when incident on the asymmetric Y-junction with a NSOM fiber. When comparing the injection using the objective lens and the injection using the NSOM probe tip, the tendency of the output change for the injection position has almost the same result. However, in the case of the probe tip injection into the asymmetric Y-junction (Figure 32(e)), there is a section in which the output mode changes, so the output ratio of the upper branch and that of the lower branch are crossed. These results support the fact that a double line fabricated with type A DLW is an effective single mode.

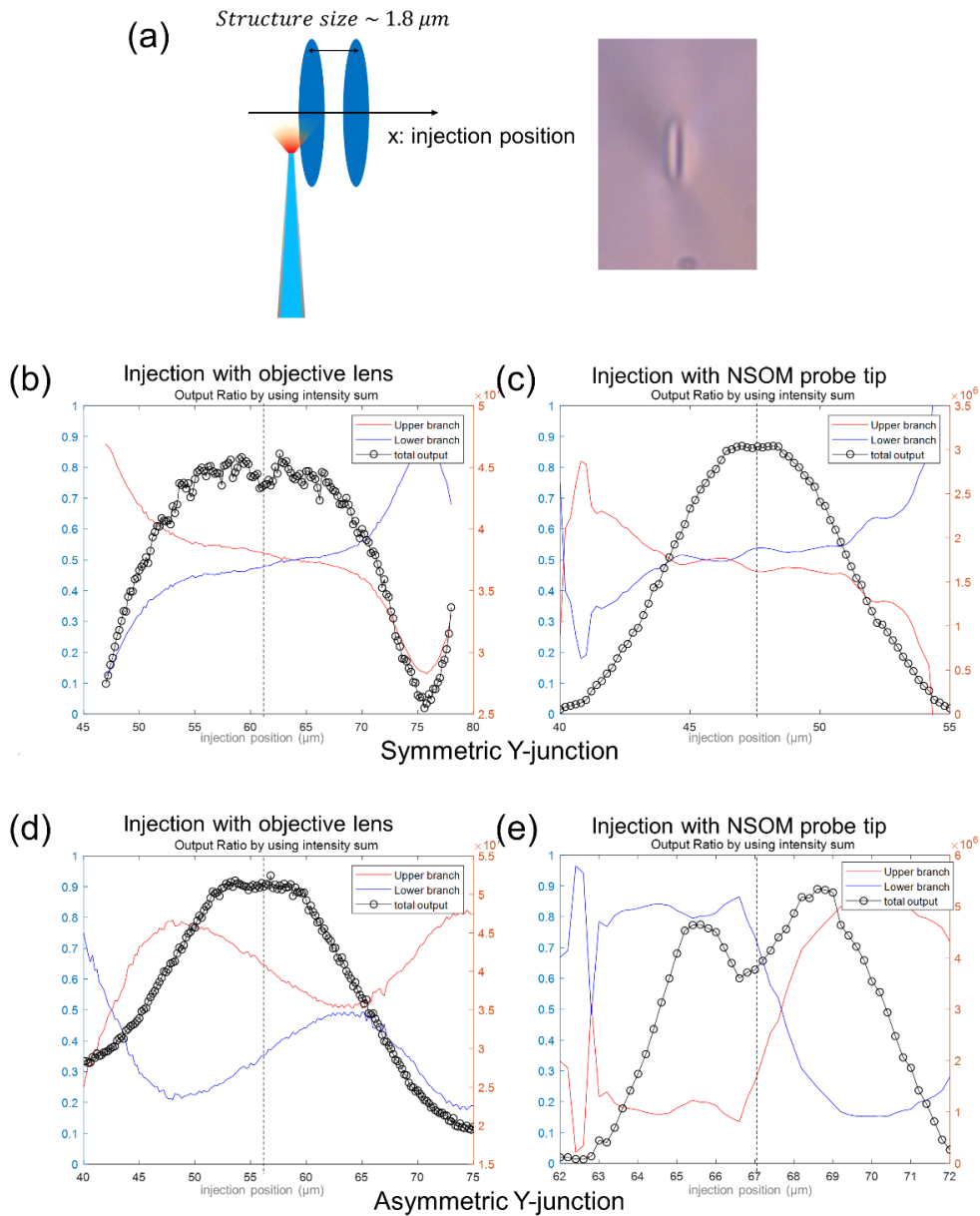


Figure 32. (a) Schematic showing beam injection into waveguide using NSOM probe tip; (b, c) output ratio result when the objective lens and the NSOM probe tip is used to put incident beam in the symmetric Y-junction; (d, e) output ratio result when the objective lens and the NSOM probe tip is used to put incident beam in the asymmetric Y-junction.

## 4.4 Conclusion

In this chapter, Y-shaped beam splitters, 2D structures made by using type A direct laser writing (DLW), was fabricated and its performance was measured. It was confirmed that a waveguide of a general shape in which the refractive index of the core is larger than that of cladding can be produced through type A DLW. Depending on the writing laser irradiance, positive refractive index changes from  $2.7 \times 10^{-3}$  to  $5.1 \times 10^{-3}$  occur. A symmetric Y-junction and various asymmetric Y-junctions were designed and fabricated using double line waveguides, and the output ratios were measured according to the transition of the injection position. It was confirmed that the output ratio could be from 96%-4% to 57%-43% due to the different irradiance in the process of writing between the upper branch and lower branch. In conclusion, we suggest that DLW in silver containing zinc phosphate glasses can be utilized easily and quickly to fabricate the desired type of optical device with only the writing process.



# Chapter 5. 5-dimensional Optical Data Storage

## 5.1 Introduction

It is no exaggeration to say that human civilization and culture today can be achieved through records and media. The history of human record dates back to prehistoric times, the days before the writing of letters. Known as the oldest murals in existence, the painting in the Chauvet-Pont-d'Arc cave in southern France is known to have been written about 30,000 years ago. Since the invention of letters, various media have been used to convey information, including mud, stones, animal bones and leathers, and papyrus. In these days, it is possible to send and receive digitized information through the Internet instead of analog methods. This approach has led to a dramatic increase in the amount of information, as shown in Figure 33.

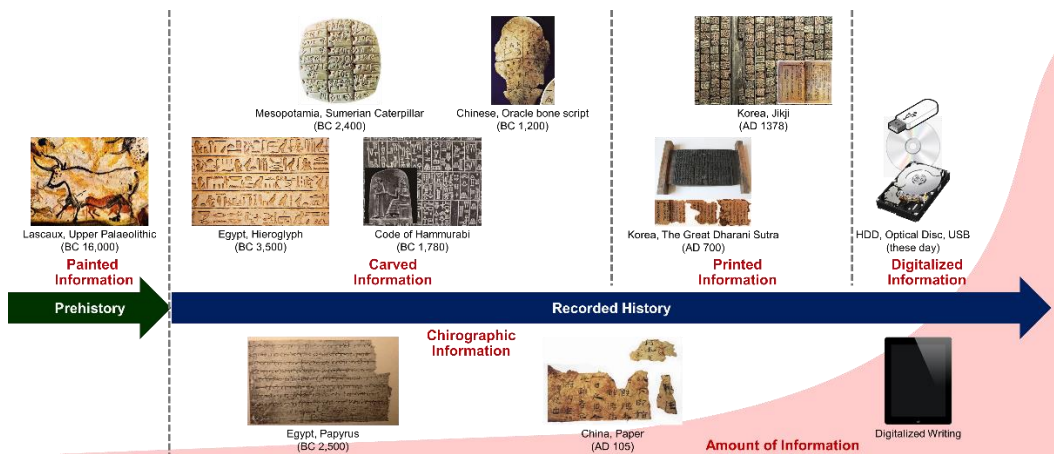


Figure 33. Historical evolution of the information recording in human society

In particular, Optical Data Storage (ODS) was started in 1976 with a Compact Disc (CD) derived from the laser disc technology demonstrated by Sony. After that ODS has evolved into Digital Versatile Disc(DVD), High Definition Digital Versatile Disc(HD DVD) and Blu-ray to increase storage capacity. This advance has been made by optimizing the laser wavelength, the numerical aperture of the objective lens, and the depth of writing plane. Figure 34 shows the schematics, surface images, physical sizes, and the data storage capacities for four ODS mediums.

	CD	DVD	HD DVD	Blu-ray
the wavelength of the injection laser and the numerical aperture of the objective lens	$\lambda = 780 \text{ nm}$ $N.A. = 0.45$ 1.1 mm	$\lambda = 650 \text{ nm}$ $N.A. = 0.6$ 0.6 mm	$\lambda = 405 \text{ nm}$ $N.A. = 0.65$ 0.6 mm	$\lambda = 405 \text{ nm}$ $N.A. = 0.85$ 0.1 mm
surface image of data medium				
The size of Unit Pattern	800nm(L) x 600 nm(W)	400nm(L) x 320 nm(W)	200nm(L) x 200 nm(W)	150nm(L) x 130 nm(W)
The size of Track Pitch	1.6 μm	740 nm	400 nm	320 nm
The width of Focusing Beam	1.6 μm	1.1 μm	620 nm	480 nm
Data Storage capacity	~680 MB	4.7GB or 8.5GB	15GB or 30 GB	25GB or 50 GB

Figure 34 Comparison of features of four ODS mediums; CD, DVD, HD DVD, and Blu-ray

After the above four ODS generations, the next mediums expected were Holographic Versatile Disc(HVD) and Digital Multilayer Disk(DMD), as shown in Figure 35. HVD employs two lasers with different wavelengths. The red laser beam is called the reference beam and serves as addressing and positioning. The other green or blue laser beam, called the signal beam, is used to write and read data. Figure 35 (b) shows that the interference fringes of these two lasers are used to write information in the photo polymer recording

layer. Using this method, it has a maximum data storage capacity of 6 TB. However, it has the following four disadvantages. (i) The price is too expensive to be in mass production, (ii) lack of error-correction technology, (iii) the optical system must be perfectly prepared, and (iv) short lifespan because it records data in the polymer.

And, as the name suggests, DMD is a way of storing information by stacking DVDs in layers. In other words, it means three-dimensional data storage, not two-dimensional data storage as shown in Figure 35 (d). Edwin Walker produced a DMD with a 200-layer, 1TB data capacity through two-photon recording[63]. Nevertheless, it is still difficult to commercialize because DMD is expensive and has cross-talk between layers. It will also depend on the material used, but the lifetime is similar to that of traditional ODS.

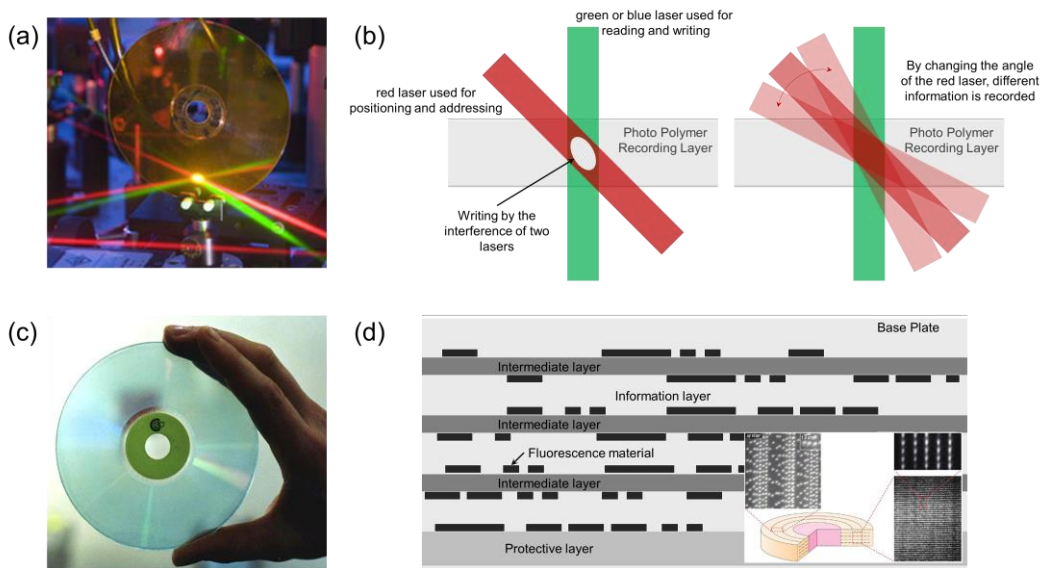


Figure 35. (a) Holographic Versatile Disc(HVD); (b) Schematic showing how HVD uses two laser beams to store information; (c) Digital Multilayer Disk(DMD); (d) Cross section of DMD layers recorded in a 3D disc

Despite remarkable progress, conventional storage media (CD / DVD, Blu-ray, HVD, DMD, USB, etc.) still have limitations on storage capacity and persistence over time [64,65]. To overcome storage capacity limitation, it has been reported that two-photon point excitation can be used to increase data storage density [66]. Figure 36 shows how P. Zijlstra et al. increased data storage density dramatically by using different incident laser wavelengths and polarizations [67]. The birefringence parameters of self-assembled nano-gratings were also employed to increase data storage dimensionality as shown in Figure 37 [68,69]. S. Alasfar et al. showed that different polarizations in urethane–urea copolymers can be used for high-density optical data storage (ODS) [70]. X. Ouyang investigated multi-level ODS with wavelength and polarization multiplexing in glass containing gold nanorods [71].

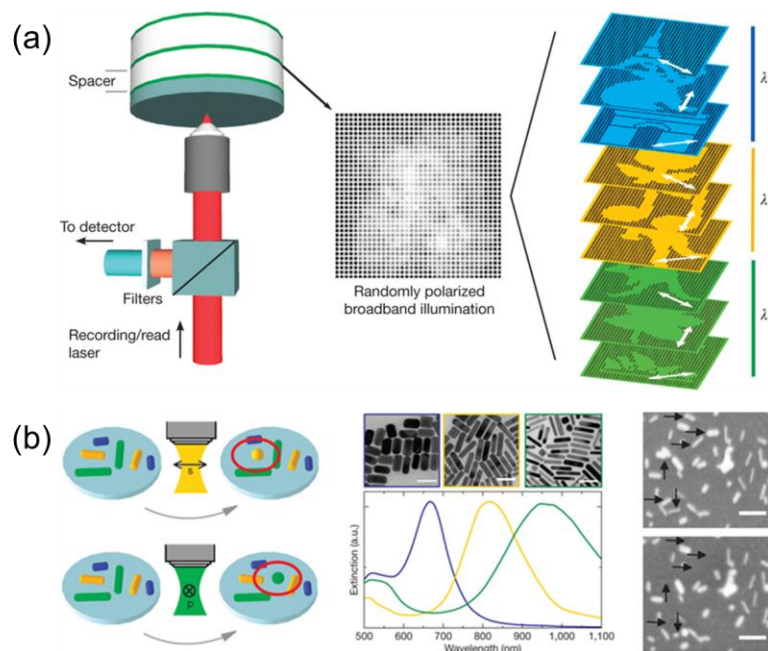


Figure 36. Experimental results of Min Gu's group using different wavelength laser beam and polarization

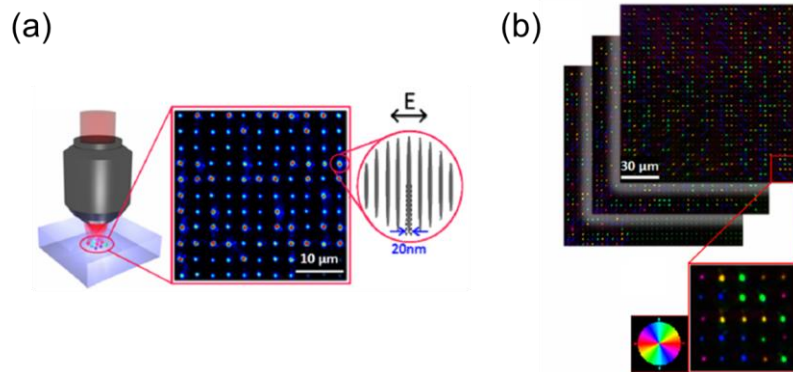


Figure 37. Experimental results from Kazansky's group implementing 5 dimensional ODS by adding orientation of nano-gratings and retardance by using type II DLW

Various materials and structures for long-term storage have been developed due to the limitations of present storage devices. Bow-tie nanoscale fuses on graphene were proposed to demonstrate permanent write-once-read-many application [72]. Permanent data storage in ZnO thin films was investigated by filamentary resistive switching devices [73]. Patterns fabricated in fused silica glasses have offered an estimated lifetime of more than 100 million years, making them suitable for the development of ultra-long lifetime ODS [69].

Type I or type II direct laser writing (DLW) had been usually adopted to produce nano- and micro-scale ODS units in fused silica and nanostructured glasses [74]. For the type I DLW, isotropic refractive index change was induced by the melting or thermal process. In case of type II DLW, birefringent index change was generated by periodic nanostructures. However, both of these DLW techniques require intense laser irradiance to create the modification. In contrast, the recently reported type A DLW can be performed in silver-containing glasses with relatively low incident laser irradiation of around 5 to 10 TW/cm<sup>2</sup> [41], taking advantage of tailored materials with sensitizing agents [34]. Fluorescent hollow

cylindrical structures were fabricated by using the Type A DLW [28,75], showing an increasing fluorescence intensity while the incident laser irradiance increases [28,76]. For long-term storage, an ageing test was carried out on a climatic test chamber at 100°C for 3100 h corresponding to a reference for long-term passive storage. No gradual changes in optical performance and less than 1% change in fluorescence spectra were observed [35].

In this paper, we investigate 5D ODS in silver-containing Zinc-phosphate glasses by using a type A DLW. Fluorescence intensity modulation, obtained by controlling the incident laser irradiance, was used to provide an additional dimension to ODS, in addition to the three spatial coordinates. In order to further increase the encoding dimensionality, the hollow cylindrical structure has been transformed into a hollow elliptical structure by performing an anamorphic focusing of the femtosecond laser, introducing the structure orientation as another experimental degree of freedom. By combining 16 levels of laser irradiance and 16 levels of ellipse orientation, two different images of 100×100 pixels in the format of 4-bit bitmap were embedded into one single image inside the silver-containing glass. The original images were decoded with an accuracy of 60.5% and 25.1% for ellipse orientation and fluorescence intensity, respectively, for the 4-bit bitmap format. When the 3-bit bitmap format is applied, the reading accuracy for the ellipse orientation was increased from 60.5% to 85.0%. In addition, by measuring the fluorescence intensity profile of primary ODS unit, we show that the data storage capacity can be reached to 14.9 Gb/cm<sup>3</sup>.

## **5.2 Experimental Methods**

### **5.2.1 Preparation of sample**

Since silver-containing glasses show a high photosensitivity, integrated waveguides, ribbon fibers, and diffraction gratings have been fabricated. For the sake of DLW quality, a commercial transparent silver-containing glass sample (AG01® from the ArgoLight company) was used. A block of fluorescent glass was specifically prepared to secure the reliability and stability. Fluorescent clusters were created in AG01® by femtosecond laser irradiation at 1030 nm, enabling the type A DLW, by tailoring irradiation parameters for the targeted 5D ODS. The imaging of all the laser-induced fluorescent features were observed with a confocal microscope (Leica, DM6 CFS TCS SP8) with 1 Airy disk pinhole and a Leica microscope objective (20x, NA = 0.75), under excited with a 405 nm laser.

### **5.2.2 First parameter for expansion of dimension: orientation of ellipse**

Yb:KGW femtosecond laser (Amplitude system, 9.8 MHz repetition rate, 390 fs pulse FWHM duration and operating at 1030 nm) was used for DLW, using a Zeiss air objective (20x, NA = 0.75), as shown in Figure 38. The front-wave phase of the laser beam was adjusted by the liquid-crystal-silicon spatial light modulator (SLM; LCOS, X10468-03, 800×600 pixel, Hamamatsu Photonics). In particular, the SLM phase mask with a cylindrical

profile was introduced to generate elliptically-shaped fluorescent patterns at the sagittal focus, so as to introduce the orientation encoding level [77].

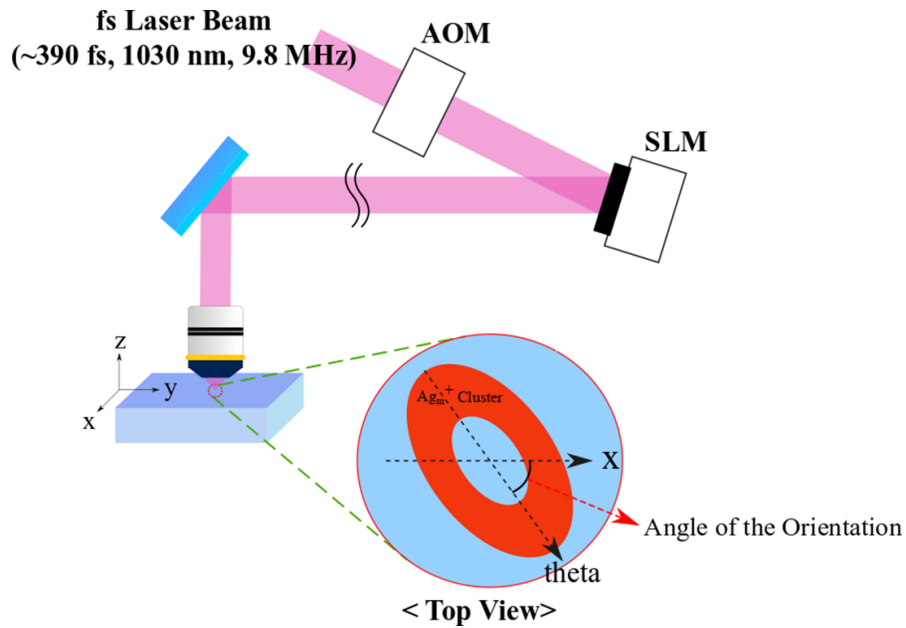


Figure 38. Femtosecond laser tightly focused in the silver containing glass, resulting in subsequent production of fluorescent silver clusters at its periphery.

For anamorphic focusing, the sagittal focusing coefficient was  $g_a$  and the tangential focusing coefficient was  $g_b$ . And the focal length was adjusted by changing these two focusing coefficients respectively. The sagittal focusing coefficient  $g_a$  was set and fixed at -0.000449 to focus on the plane of the sample we observe with the CMOS camera. Figure 39 shows the variation of SLM mask and DLW patterns according to the manipulation of tangential focusing coefficients  $g_b$ . When the tangential focusing coefficient is the same as the sagittal focusing coefficient, we can see that it has a DLW pattern of ring-shape. On the other hand, as the value of the tangential focusing coefficient changes, the long axis of the ellipse-shape gradually changes due to anamorphic focusing.

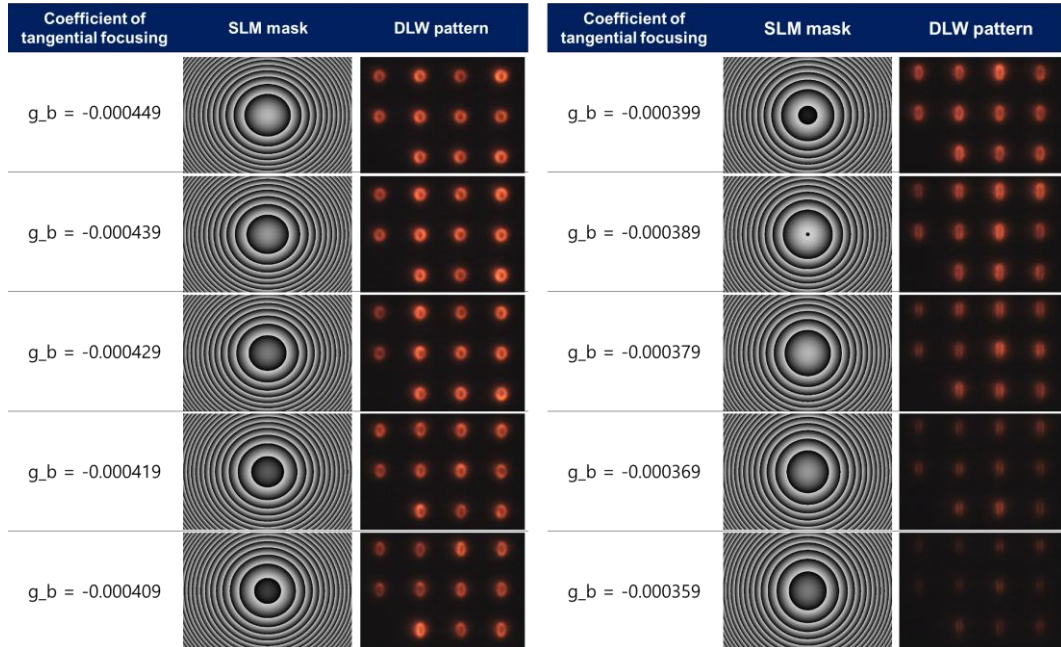


Figure 39. Variation of SLM mask and DLW patterns according to the manipulation of coefficient of tangential focusing

However, as shown in Figure 39, the tangential focal length elongates as the tangential coefficient increases, in other words the astigmatism is to be larger. So the range of the anamorphic coefficients needs to be set. As the tangential focusing coefficient changes, the eccentricity and fluorescence intensity are measured. The ellipse-shape's DLW pattern will later change its orientation. Therefore, as shown in Figure 40(a) we have determined that the eccentricity of ellipse must be greater than or equal to 0.5 for this ellipse to have a clear ellipse shape. However, Figure 40(b) shows that having a large eccentricity lowers the fluorescence intensity. This also adversely affects the decoding process. Therefore, we set the range of tangential coefficient from -0.000419 to -0.000409 to satisfy both eccentricity and fluorescence intensity simultaneously.

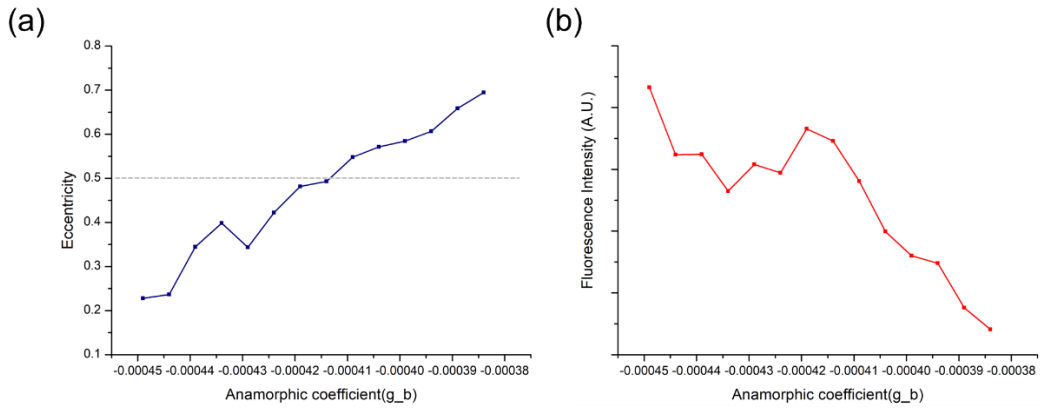


Figure 40. Variations of eccentricity(a) and fluorescence intensity(b) of ellipse-shape DLW pattern according to tangential focusing coefficient

The 16-step orientations of the elliptical pattern at the sagittal focus were produced by rotating the SLM mask. The orientation angle of the SLM mask then depicts the orientation of the main axis of the cylindrical phase contribution, which will also correspond to the orientation of the associated laser-induced fluorescent pattern. In this framework, Figure 41 shows the 16-step orientation angles of the SLM patterns at  $0^\circ$ ,  $11.25^\circ$ ,  $22.5^\circ$ ,  $33.75^\circ$ ,  $45^\circ$ ,  $56.25^\circ$ ,  $67.5^\circ$ ,  $78.75^\circ$ ,  $90^\circ$ ,  $101.25^\circ$ ,  $112.5^\circ$ ,  $123.75^\circ$ ,  $135^\circ$ ,  $146.25^\circ$ ,  $157.5^\circ$ , and  $168.75^\circ$ . Astigmatism was intentionally enhanced by anamorphic focusing to clearly illustrate here the orientation direction of the elliptical pattern.

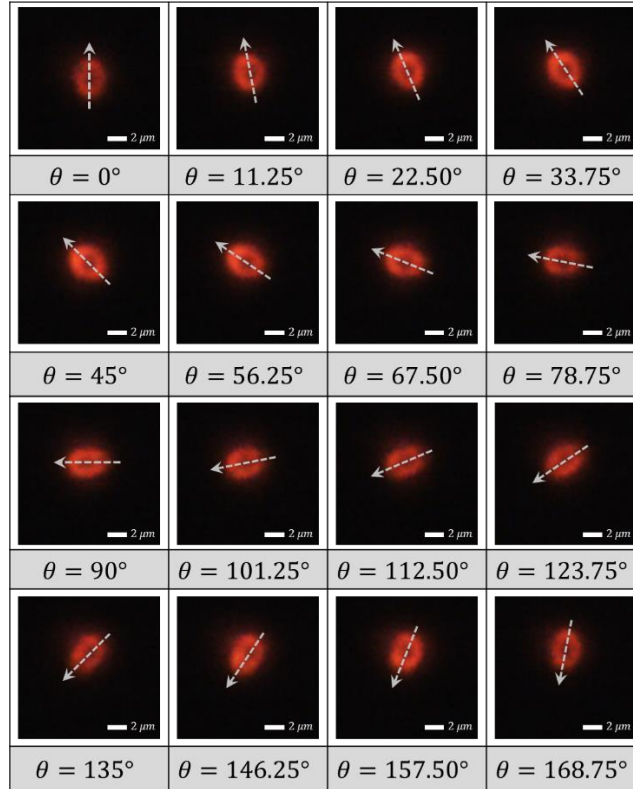


Figure 41. Images of orientation change of elliptical patterns obtained by SLM phase mask manipulation, corresponding to  $2^4 = 16$  orientation-encoded digital levels.

Figure 42 shows that the fluorescent pattern obtained by DLW varies with the distance from the focal plane. As displayed in Figure 39, in the case of anamorphic focusing with the cylindrical phase mask (such as it is the case for astigmatic beams), the caustic form (including both orientation and eccentricity) keeps on evolving with depth around the focal plane depth. In contrast, for symmetric focusing, the circular writing pattern does not change much with depth. The fluorescence intensity at the sagittal focus was observed to be the strongest with a clear oval pattern, and the eccentricity of the ellipse was also found to be the best for optimal post-DLW operation of orientation retrieving.

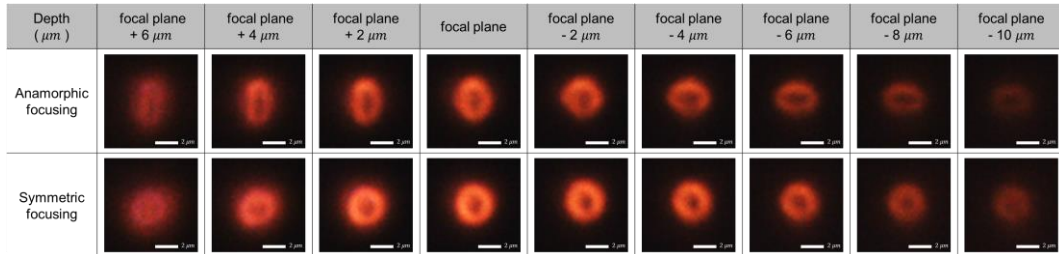


Figure 42. Fluorescent silver cluster distributions for several depths with respect to the tangential focal plane, respectively corresponding to circular or elliptical fluorescent shapes (confocal microscope imaging (20x, NA = 0.75) with excitation at 405 nm), for symmetrical or anamorphic focusing conditions.

### 5.2.3 Second parameter for expansion of dimension: Intensity of fluorescence

Although 1 bit-writing for intensity of 0 or 1 was used in conventional ODS medium, Arnaud Royon showed that 4bit-writing is possible with DLW in silver-containing glass [76]. The modification of the silver-containing glass depends on the laser irradiance, which can be determined by measuring the fluorescence intensity. And the irradiance of the laser at the sample was controlled by applied voltage at Acousto-Optic Modulator(AOM), called a Bragg cell. The voltage applied to the AOM is controlled between 0V and 1V, and the applied voltage and intensity of the 0th order diffracted beam are not linear as shown in Figure 43. In addition, when the voltage applied to AOM is low, photo-dissociation is not enough, and the modification is completed without formation of ellipse shape. Figure 43 (b) shows that a minimum voltage of 0.6V must be applied to the AOM for the orientation of ellipse to be retrieved. Therefore, the voltage range that satisfies both conditions, (i)

fluorescence intensity should have maximum linearity and (ii) orientation of ellipse should be retrieved, is from 0.6V to 0.8V.

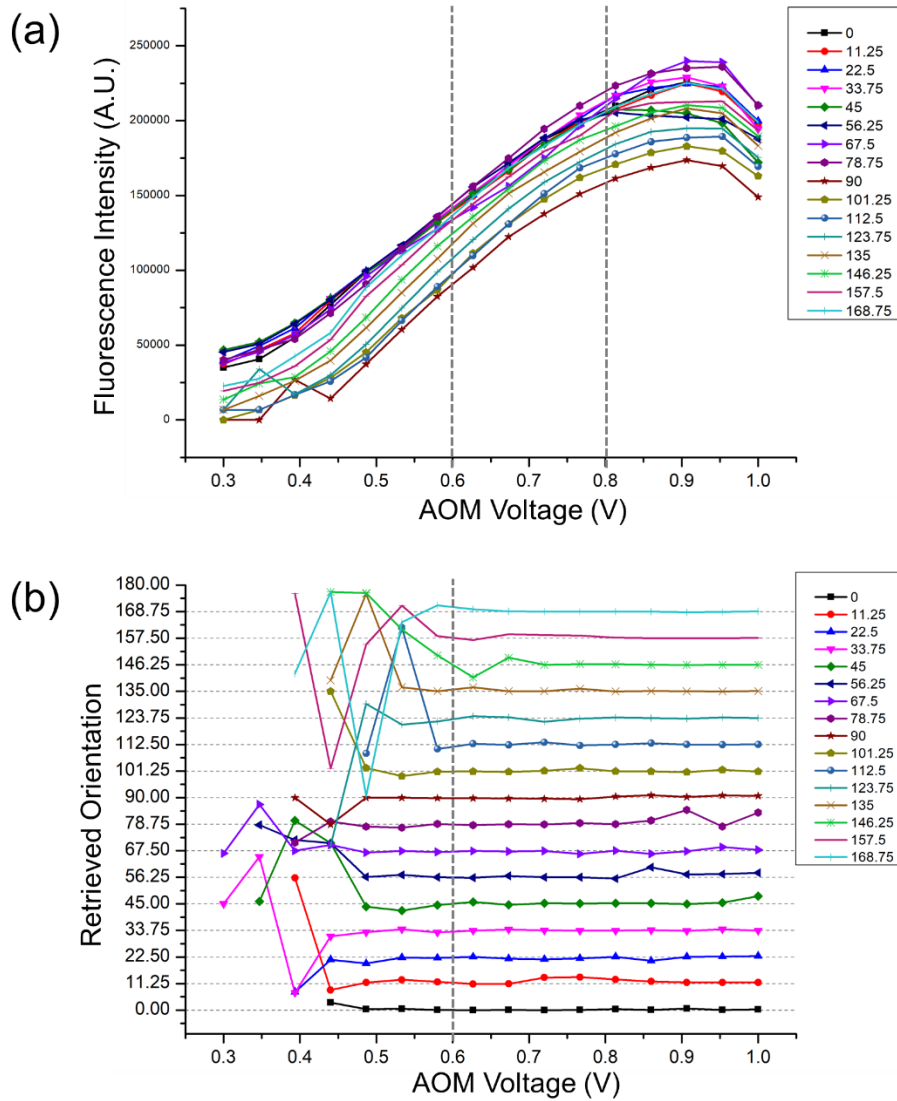


Figure 43. Fluorescence intensity change(a) and retrieving result of ellipse orientation(b) according to voltage applied to AOM

The AOM voltage command led to sample irradiations from 9.4 to 12.7 TW/cm<sup>2</sup> (pulse energy from 41.7 nJ to 56.2 nJ) at the beam focus, where the lower irradiance limit was slightly above the production of identifiable ellipsoidal patterns. Since laser intensity is not linear according to the AOM voltage, the voltage applied to the AOM is adjusted so that the laser intensity is evenly spaced for the 16-step DLW, so as to further provide  $2^4 = 16$  intensity-encoded digital levels as shown in Figure 44.

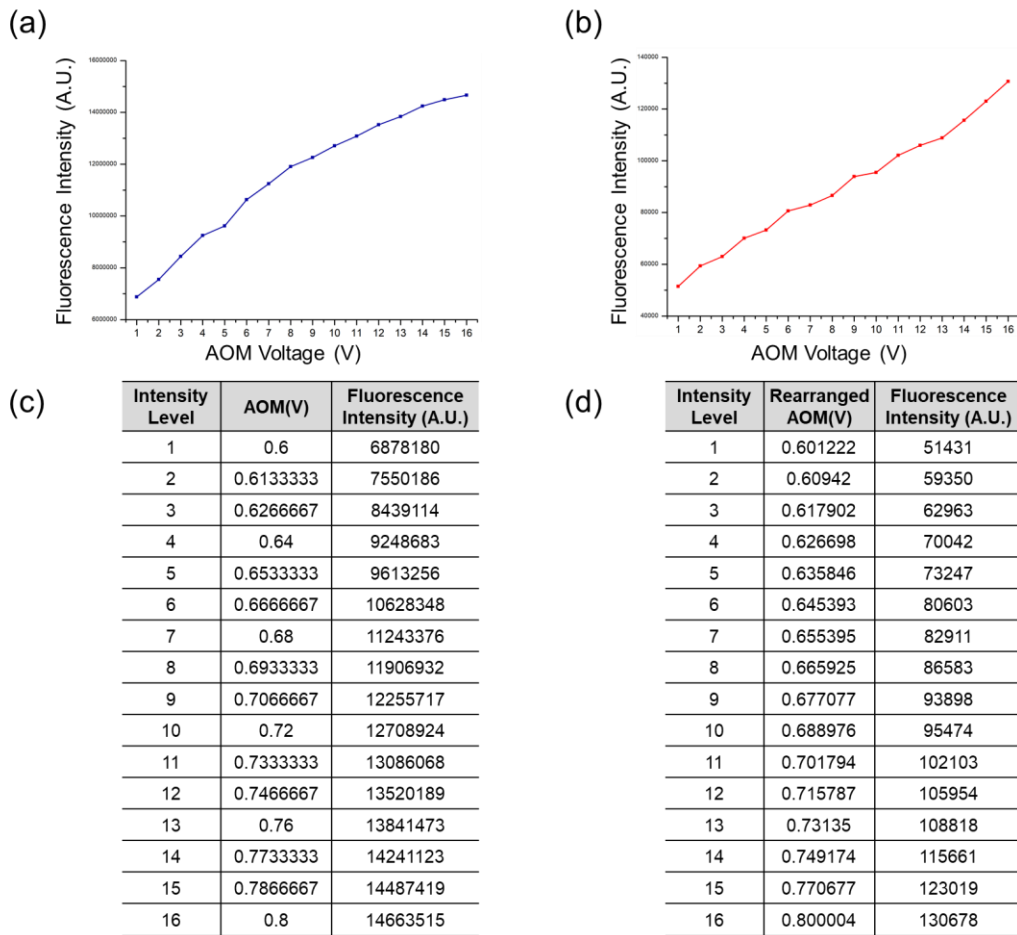


Figure 44. Relation between intensity level and fluorescence intensity (a, c) when voltage intervals from 0.6V to 0.8V are divided equally and (b, d) When optimized by dividing fluorescence intensity interval equally

It should be emphasized that in this experiment the range of laser irradiation was carefully chosen to be appropriate for writing patterns with sufficient fluorescence emission amplitude, so as to subsequently allow for an accessible reading of both the ellipse orientation and the intensity of fluorescence simultaneously. In our previous experiment [15], the laser irradiance was varied in a larger range, from a low irradiance level slightly above the DLW threshold up to a high irradiance level slightly below the material damage threshold, because in that case only fluorescence intensity was encoded and measured.

#### **5.2.4 Fluorescence calibration matrix with 16 intensity levels and 16 orientations of ellipse**

Inset image in Figure 45 shows the  $2^8 = 256$  fluorescence matrix fabricated by  $2^4 = 16$  levels of ellipse orientation and  $2^4 = 16$  levels of laser irradiance in the silver-containing glass. Here, the vertical axis represents the 16 levels of orientation, and the horizontal axis corresponds to the 16 levels of incident irradiance. From such a calibration microscope image, the measured fluorescence intensity versus the incident irradiance level is displayed in Figure 45. As shown in Figure 45, fluorescence intensity at level 5 ( $45^\circ$ ) was the highest, and increased linearly while increasing the incident laser irradiance. Minimum fluorescence intensities for different orientation levels were distributed irregularly, but the linearity with the laser irradiance increase was mostly maintained. We believe that this variation is mainly due to the residual mismatch between the center of the laser beam and the center of the SLM mask for anamorphic focusing and/or due to a minor astigmatism of the incident laser

itself. The graph from Figure 45 can be further used as a calibration matrix to retrieve 5D stored data in the reading process.

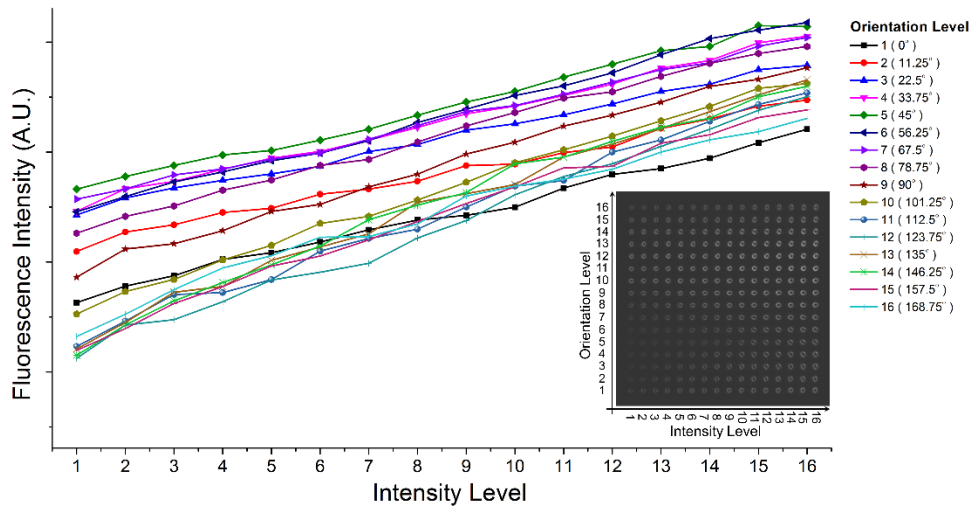


Figure 45. Measured fluorescence intensity versus incident laser irradiance, to calibrate the 5D decoding process. The inset image shows a fabricated matrix with 16 intensity levels and 16 orientations in the silver-containing glass.

### 5. 3 Outline of writing and reading process of optical data storage using two additional parameters with type A DLW

We confirmed the possibility of 5D Optical Data Storage using two independent parameters determined in the previous chapter with the flow shown in Figure 46. We select two images that represent the data of intensity and orientation respectively. As the first step, each pixel of the images selected is converted into an 8-bit image having 256 levels. At this time, the stored image can be represented as a matrix, where  $M_{i0}$  is the first matrix of the

intensity parameter and  $M_{o0}$  is the first matrix of the orientation variable. The saved  $M_{i0}$  and  $M_{o0}$  are converted once again for writing. The intensity image is converted to p-bit image and the orientation image is converted to q-bit image, represented by  $M_{i1}^p$  and  $M_{o1}^q$ . The converted intensity matrix  $M_{i1}^p$  is utilized for by the voltage of the AOM, simultaneously the converted orientation matrix  $M_{o1}^q$  is used for the rotation of the SLM mask. In this way, the two variables are intertwined so that one image is engraved in the sample through the type A DLW. The intensity image of this entangled image is represented by  $M_{i2}$  and the orientation image by  $M_{o2}$ . At this time,  $M_{i2}$  can be recognized directly as usual point drawing.  $M_{o2}$ , on the other hand, is hidden because it contains an image as an orientation of ellipse. This is the end of the waiting process.  $M_{i2}$  will reach  $M_{i3}$  through q-bit decoding. Likewise, q'-bit retrieving for  $M_{o2}$  brings  $M_{o3}$ . In the reading process, q and q 'can be optimized according to the situation. In this study, we studied the writing and reading process for the following number of bits. (p, p'=4 (fixed)), (q, q'=4 (16 level) or 3 (downgraded to 8 level))

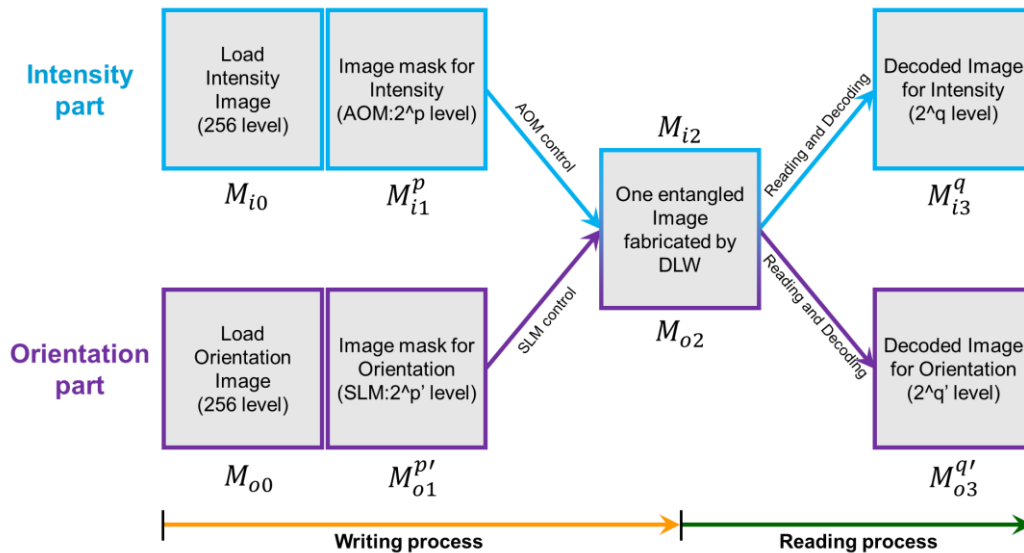


Figure 46. Flow map showing how intensity part and orientation part are utilized in writing/reading process of 5D optical data storage

#### 5. 4 Writing process with 256 levels: 16 levels for fluorescence intensity and 16 levels for orientation of elliptical pattern

For the writing process, two images of two Nobel Prize-winning French physicists were selected for simultaneous DLW using both levels of incident irradiance and ellipse orientation. Each image, composed of  $100 \times 100$  pixels, was converted to 4-bit bitmap format based on 16 levels of incident irradiance (Figure 47(a)) and 16 levels of ellipse orientation (Figure 47(b)), respectively.

Type A DLW with  $16 \times 16$  levels was used to inscribe a single image composed of two entangled images at the same XY plane in the silver-containing glass, as shown in Figure 47(c). Each fluorescent pattern was produced by irradiating  $10^6$  laser pulses through a Zeiss objective lens ( $20\times$ ,  $NA = 0.75$ ). Patterns were written with a spacing of  $7 \mu\text{m}$  so that adjacent patterns do not overlap laterally. Therefore, the entangled image inscribed through the writing process has a size of  $700 \mu\text{m} \times 700 \mu\text{m}$ .

As show in Figure 47(c), the image recorded using laser irradiance is visually recognizable in the entangled ODS image. The image recorded by the ellipse orientation also partially appears due to the slight coupling of fluorescence intensity distribution with respect to the orientation direction. Indeed, the fluorescence intensity was partially affected by non-uniform laser irradiance and/or by the slight intrinsic laser astigmatism, when rotating the ellipse pattern of the SLM mask, as mentioned above. Therefore, in order to retrieve the ellipse orientation of each pattern, a fluorescence correction matrix was required, similarly to what discussed about Figure 45. Hence, the calibration fluorescence matrix with  $16 \times 16$  intensity and orientation levels was simultaneously fabricated near the entangled DLW image, as shown in Figure 47(d), in order to minimize the reading errors. During the imaging process, we paid attention to reduce the non-uniformity from the scanning type of microscope so that a small region of interest ( $124.67 \mu\text{m} \times 124.67 \mu\text{m} \times 4096$  pixels, pixel dwell time: 300 ns, 4 frame average) was selected and repeated step-by-step to cover the full image.

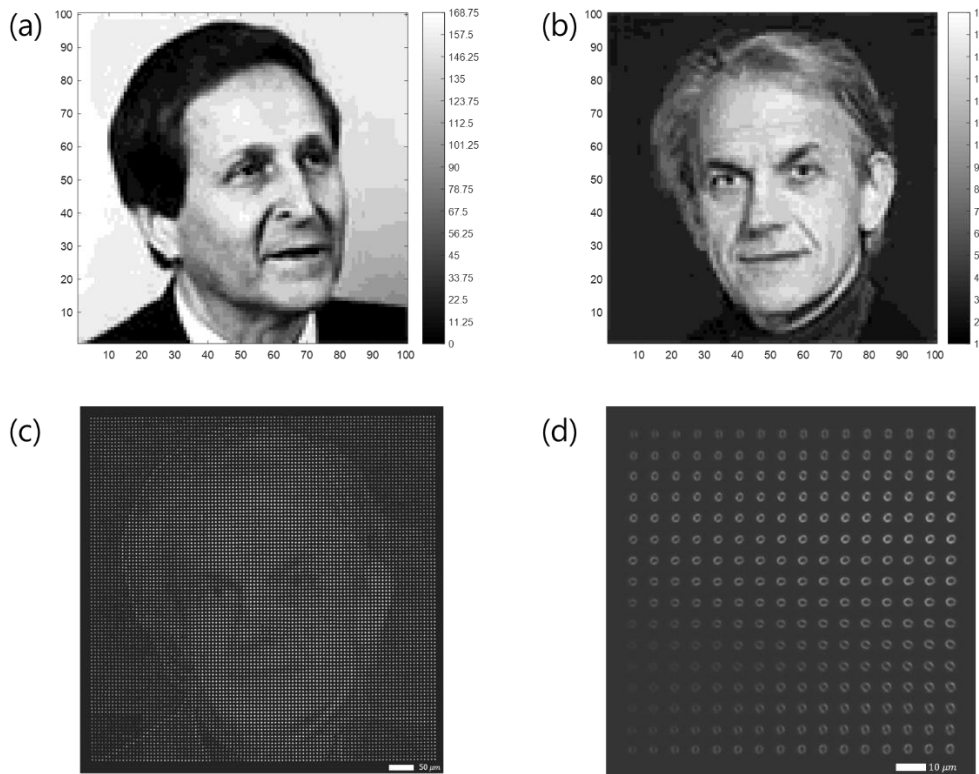


Figure 47. (a) and (b) are the original images of two Nobel laureates encoded in 16 grey-scale levels; (c) is the DLW entangled image by independently addressing the 16 orientation levels of (a) and the 16 irradiance levels of (b); (d) Fluorescence calibration matrix observed by confocal microscopy to retrieve intensity-orientation correlations and to provide the dedicated correction for subsequent fluorescence intensity reading (excitation at 405 nm).

## **5. 5 Reading process with 256 levels: 16 levels for fluorescence intensity and 16 levels for orientation of ellipse**

Each of the 100x100 patterns of the entangled image (Figure 47 (c)) has been compared with the 256 patterns of the calibration matrix (Figure 45, insert) for the readout process. In this process to overcome the un-uniformity of the confocal microscope, we tried to split the 100x100 image into 49 (7x7) split images to minimize the vignetting effect. The DLW pattern with information was compared with all of the 256 patterns in the calibration, and the pattern with the smallest deviation among the 256 patterns in the calibration matrix is selected. The pattern with information is then considered to have the same intensity/orientation level as the intensity/orientation level of the selected pattern. So level of fluorescence intensity and level of ellipse orientation were obtained simultaneously. In this way, decoding of one pattern was complete. Decoding was done for all information patterns sequentially, eventually the merged laser-imprinted image was split into two decoded images, as represented by  $M_{i3}^q$  and  $M_{o3}^q$  in Figure 46.

The retrieved images decoded over 16 orientation levels and 16 intensity levels are shown in Figure 48(a) and Figure 48(b). Detailed error analysis was performed to quantify the fidelity of the readout process and this was shown as a table and histogram for each DLW pattern. Comparing each of the two decoded images with the original 4-bit bitmap images, it was found that the orientation and intensity readout fidelities were 61% and 25%, respectively. The 4-bit orientation readout errors showed 34% 1-bit error and 5% 2-bit error. The 4-bit intensity readout errors showed 43% 1-bit error and 32% 2-bit (or more) error. The readout fidelity of intensity level was lower than that of the elliptical orientation level.

The lower intensity readout fidelity is mainly due to inhomogeneous intensity distribution of the readout laser at the focal plane. Figure 48(c) and Figure 48(d) display the level difference (namely the bit error) between the original and retrieved images for orientation and intensity, respectively. In other words, Figure 48(c) and Figure 48(d) are the level error images resulting from overall coding process. Even more than for Figure 48(c), the image generated by the elliptical writing appears slightly in Figure 48(d), due to the nonlinearity of intensity levels for the different elliptical orientations. As mentioned above, such nonlinearity occurs when the laser beam is not ideally aligned with the SLM mask and/or when the laser beam intrinsic astigmatism tends to couple the two intensity/orientation degrees of freedom. Therefore, we believe that this cross-correlation may be significantly decreased by minimizing the misalignment between the center of the laser beam and the center of the elliptical phase pattern on the SLM and/or with a laser showing a lower astigmatism. Moreover, in the error images, one can easily observe the successive positions of selected region of interest while imaging with the fluorescence microscope, showing how the composite image shown in Figure 47(c) has been recorded. Such a non-uniformity of sensitivity within the field of view of the used fluorescence microscope strongly affects and degrades the present retrieving process, which is indeed independent of the encoding and writing process. Strong improvement can thus be expected using a better spatially calibrated fluorescence microscope.

Figure 48(e) shows the histogram of the level difference between the original and decoded levels for the orientation dimension ( $\Delta O$ ). The accuracy increased from 61% to 95% if adjacent levels of  $\Delta O = \pm 1$  were included, as expected if the number of reading levels was reduced. Figure 48(f) indicates the histogram of the level difference between

the original and decoded levels for the fluorescence intensity ( $\Delta I$ ). Similar to orientation fidelity issues, the accuracy increased from 25% to 68% when including adjacent level of  $\Delta I = \pm 1$ .

For a more in-depth analysis, Table 4, Table 5, Figure 49, Figure 50, Figure 51, Figure 52, Figure 53, Figure 54, Figure 55, and Figure 56 show the results of each orientation / intensity level for 256 unit patterns. Table 4, Figure 49, Figure 50, Figure 51, and Figure 52 are the results for orientation decoding, and Table 5, Figure 53, Figure 54, Figure 55, and Figure 56 are the results for intensity decoding. In Table 4, in the case of  $\Delta O=0$  retrieved results are good in certain orientations, but not very good in some orientations. Including the case of  $\Delta O=\pm 1$ , the result is still not good at 11.25 degree, but the retrieving result of most orientation is improved. Although this error comes from experimental misalignment, it is worth verifying with 3-bit decoding rather than 4-bit decoding. Decoding results for each orientation/intensity can be found in histogram with the following detailed analysis. Number of patterns used, retrieving result, and errors.

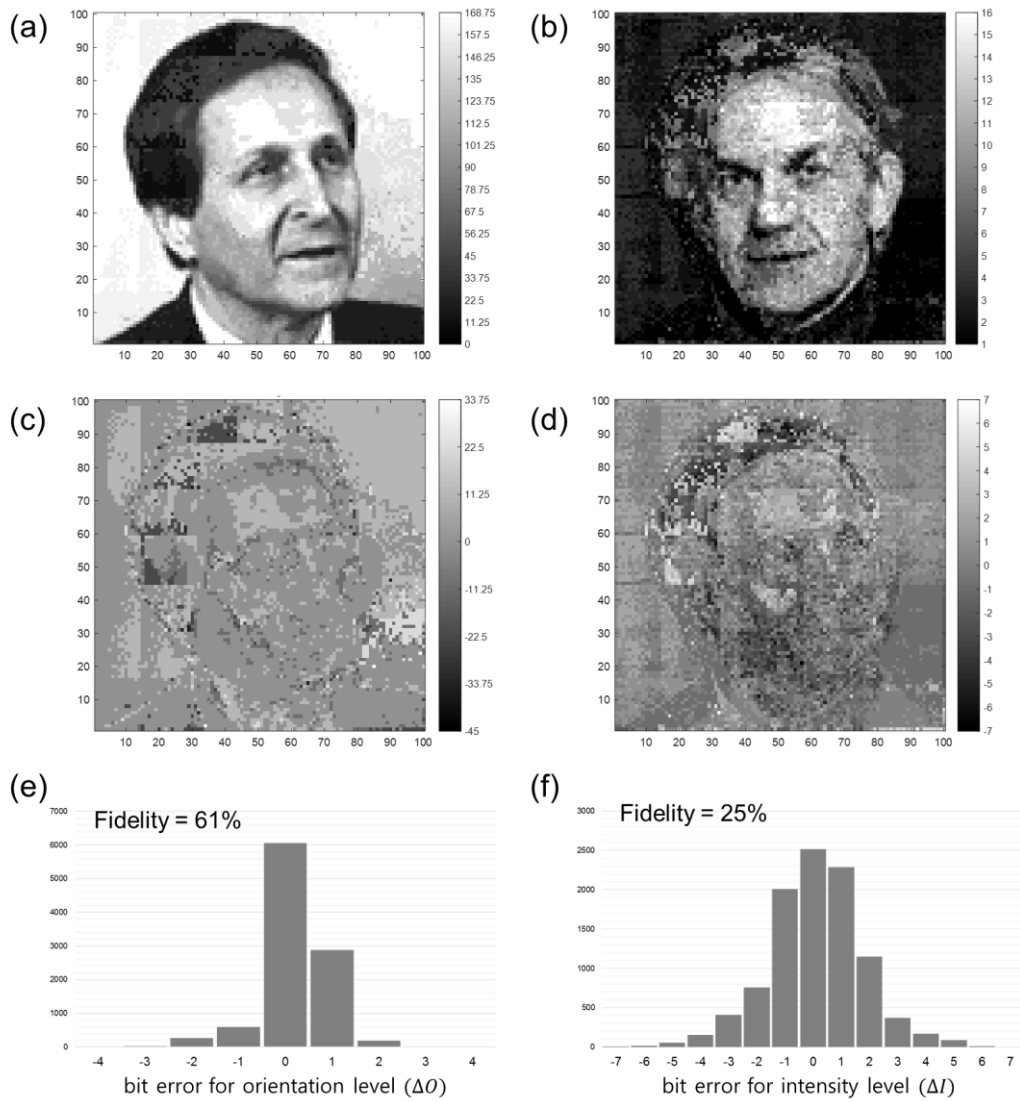


Figure 48. (a) Retrieved image from the initial image in Figure 47(a); (b) Retrieved image from the initial image in Figure 47(b); (c) Level difference between Figure 47(a) and 16(a); (d) Level difference between Figure 47(b) and 16(b); (e) Histogram of the level difference between original and decoded levels for the orientation direction; (f) Histogram of the level difference between original and decoded levels for the fluorescence intensity.

$\Delta O=0$		Orientation Level															
		0	11.25	22.5	33.75	45	56.25	67.5	78.75	90	101.25	112.5	123.75	135	146.25	157.5	168.75
Intensity Level	1	87.50%	#DIV/0!	0.00%	100.00%	#DIV/0!	100.00%	#DIV/0!	#DIV/0!	0.00%	0.00%	0.00%	100.00%	0.00%	0.00%	#DIV/0!	100.00%
	2	93.44%	76.92%	100.00%	40.00%	50.00%	77.78%	20.00%	20.00%	40.00%	40.00%	44.83%	84.21%	0.00%	20.00%	43.43%	100.00%
	3	95.82%	38.56%	100.00%	33.33%	79.41%	82.22%	16.22%	9.30%	71.19%	94.40%	83.12%	13.07%	13.20%	51.15%	32.53%	99.84%
	4	77.27%	29.84%	100.00%	47.37%	100.00%	73.68%	21.43%	16.67%	77.78%	90.91%	60.00%	7.41%	16.67%	32.31%	18.75%	100.00%
	5	90.53%	5.60%	97.44%	91.67%	90.00%	66.67%	90.00%	46.67%	68.00%	95.65%	29.41%	0.00%	9.09%	65.12%	0.00%	100.00%
	6	73.91%	3.65%	87.93%	95.00%	94.44%	40.00%	83.33%	50.00%	73.33%	81.25%	42.86%	0.00%	19.05%	67.74%	0.00%	100.00%
	7	87.50%	1.16%	77.61%	100.00%	100.00%	92.31%	46.67%	42.11%	53.85%	78.57%	42.86%	0.00%	5.26%	84.38%	22.22%	#DIV/0!
	8	100.00%	0.00%	73.47%	100.00%	100.00%	92.86%	80.00%	61.54%	92.86%	75.00%	46.15%	0.00%	40.74%	80.00%	12.50%	#DIV/0!
	9	100.00%	0.00%	68.97%	100.00%	94.74%	91.43%	87.50%	70.00%	100.00%	100.00%	36.36%	0.00%	68.97%	100.00%	16.67%	#DIV/0!
	10	100.00%	0.00%	73.53%	100.00%	100.00%	100.00%	59.26%	78.57%	100.00%	100.00%	44.83%	17.86%	87.04%	97.44%	20.00%	#DIV/0!
	11	100.00%	0.00%	87.50%	100.00%	94.12%	100.00%	88.89%	100.00%	100.00%	98.00%	73.91%	27.50%	89.66%	100.00%	0.00%	#DIV/0!
	12	100.00%	0.00%	88.89%	100.00%	100.00%	100.00%	100.00%	70.00%	100.00%	93.85%	91.49%	30.23%	94.87%	100.00%	9.52%	#DIV/0!
	13	100.00%	0.00%	87.50%	100.00%	100.00%	100.00%	100.00%	89.29%	100.00%	96.15%	94.87%	52.63%	96.67%	99.47%	12.82%	100.00%
	14	100.00%	0.00%	75.00%	100.00%	100.00%	100.00%	100.00%	100.00%	100.00%	100.00%	97.22%	68.42%	93.62%	98.11%	8.18%	100.00%
	15	#DIV/0!	0.00%	0.00%	100.00%	100.00%	100.00%	100.00%	100.00%	100.00%	100.00%	100.00%	75.00%	100.00%	100.00%	15.38%	100.00%
	16	#DIV/0!	#DIV/0!	#DIV/0!	#DIV/0!	#DIV/0!	#DIV/0!	#DIV/0!	#DIV/0!	#DIV/0!	100.00%	100.00%	100.00%	#DIV/0!	#DIV/0!	#DIV/0!	#DIV/0!

$\Delta O=\pm 1$		Orientation Level															
		0	11.25	22.5	33.75	45	56.25	67.5	78.75	90	101.25	112.5	123.75	135	146.25	157.5	168.75
Intensity Level	1	0.00%	#DIV/0!	0.00%	0.00%	#DIV/0!	0.00%	#DIV/0!	#DIV/0!	100.00%	83.33%	100.00%	0.00%	100.00%	0.00%	#DIV/0!	0.00%
	2	6.56%	7.69%	0.00%	60.00%	50.00%	0.00%	20.00%	80.00%	60.00%	60.00%	48.28%	15.79%	87.50%	80.00%	56.57%	0.00%
	3	4.18%	25.49%	0.00%	66.67%	20.59%	15.56%	45.95%	86.05%	27.12%	5.60%	14.29%	35.18%	71.57%	44.26%	67.47%	0.16%
	4	22.73%	25.00%	0.00%	52.63%	0.00%	26.32%	71.43%	83.33%	22.22%	9.09%	35.00%	66.67%	75.00%	63.08%	81.25%	0.00%
	5	9.47%	64.80%	2.56%	8.33%	10.00%	33.33%	10.00%	53.33%	32.00%	4.35%	70.59%	80.00%	54.55%	27.91%	100.00%	0.00%
	6	26.09%	67.88%	8.62%	5.00%	5.56%	60.00%	16.67%	50.00%	26.67%	18.75%	57.14%	70.00%	57.14%	25.81%	100.00%	0.00%
	7	12.50%	66.28%	22.39%	0.00%	0.00%	7.69%	53.33%	57.89%	46.15%	21.43%	57.14%	78.95%	73.68%	12.50%	77.78%	#DIV/0!
	8	0.00%	81.03%	18.37%	0.00%	0.00%	7.14%	20.00%	38.46%	7.14%	25.00%	53.85%	92.31%	44.44%	20.00%	87.50%	#DIV/0!
	9	0.00%	97.06%	27.59%	0.00%	5.28%	8.57%	12.50%	30.00%	0.00%	0.00%	63.64%	96.15%	31.03%	0.00%	83.33%	#DIV/0!
	10	0.00%	94.12%	26.47%	0.00%	0.00%	0.00%	40.74%	21.43%	0.00%	0.00%	55.17%	82.14%	12.96%	2.56%	80.00%	#DIV/0!
	11	0.00%	95.00%	12.50%	0.00%	5.88%	0.00%	11.11%	0.00%	0.00%	2.00%	26.09%	72.50%	10.34%	0.00%	100.00%	#DIV/0!
	12	0.00%	66.67%	11.11%	0.00%	12.50%	0.00%	0.00%	30.00%	0.00%	6.15%	8.51%	69.77%	5.13%	0.00%	90.48%	#DIV/0!
	13	0.00%	100.00%	12.50%	0.00%	0.00%	0.00%	0.00%	10.71%	0.00%	3.85%	5.13%	47.37%	3.33%	0.53%	87.18%	0.00%
	14	0.00%	100.00%	25.00%	0.00%	0.00%	0.00%	0.00%	0.00%	0.00%	0.00%	2.78%	31.58%	6.38%	1.89%	91.82%	0.00%
	15	#DIV/0!	100.00%	100.00%	0.00%	0.00%	0.00%	0.00%	0.00%	0.00%	0.00%	0.00%	25.00%	0.00%	0.00%	84.62%	0.00%
	16	#DIV/0!	#DIV/0!	#DIV/0!	#DIV/0!	#DIV/0!	#DIV/0!	#DIV/0!	#DIV/0!	0.00%	0.00%	0.00%	#DIV/0!	#DIV/0!	#DIV/0!	#DIV/0!	#DIV/0!

$\Delta O=0, \pm 1$		Orientation Level															
		0	11.25	22.5	33.75	45	56.25	67.5	78.75	90	101.25	112.5	123.75	135	146.25	157.5	168.75
Intensity Level	1	87.50%	#DIV/0!	0.00%	100.00%	#DIV/0!	100.00%	#DIV/0!	#DIV/0!	100.00%	83.33%	100.00%	100.00%	100.00%	0.00%	#DIV/0!	100.00%
	2	100.00%	84.62%	100.00%	100.00%	100.00%	77.78%	40.00%	100.00%	100.00%	100.00%	93.10%	100.00%	87.50%	100.00%	100.00%	100.00%
	3	100.00%	64.05%	100.00%	100.00%	100.00%	97.78%	62.16%	95.35%	98.31%	100.00%	97.40%	48.24%	84.77%	95.41%	100.00%	100.00%
	4	100.00%	54.84%	100.00%	100.00%	100.00%	100.00%	92.86%	100.00%	100.00%	100.00%	95.00%	74.07%	91.67%	95.38%	100.00%	100.00%
	5	100.00%	70.40%	100.00%	100.00%	100.00%	100.00%	100.00%	100.00%	100.00%	100.00%	100.00%	80.00%	63.64%	93.02%	100.00%	100.00%
	6	100.00%	71.53%	96.55%	100.00%	100.00%	100.00%	100.00%	100.00%	100.00%	100.00%	100.00%	70.00%	76.19%	93.55%	100.00%	100.00%
	7	100.00%	67.44%	100.00%	100.00%	100.00%	100.00%	100.00%	100.00%	100.00%	100.00%	100.00%	78.95%	78.95%	96.88%	100.00%	#DIV/0!
	8	100.00%	81.03%	91.84%	100.00%	100.00%	100.00%	100.00%	100.00%	100.00%	100.00%	100.00%	92.31%	85.19%	100.00%	100.00%	#DIV/0!
	9	100.00%	97.06%	96.55%	100.00%	100.00%	100.00%	100.00%	100.00%	100.00%	100.00%	100.00%	96.15%	100.00%	100.00%	100.00%	#DIV/0!
	10	100.00%	94.12%	100.00%	100.00%	100.00%	100.00%	100.00%	100.00%	100.00%	100.00%	100.00%	100.00%	100.00%	100.00%	100.00%	#DIV/0!
	11	100.00%	95.00%	100.00%	100.00%	100.00%	100.00%	100.00%	100.00%	100.00%	100.00%	100.00%	100.00%	100.00%	100.00%	100.00%	#DIV/0!
	12	100.00%	66.67%	100.00%	100.00%	100.00%	100.00%	100.00%	100.00%	100.00%	100.00%	100.00%	100.00%	100.00%	100.00%	100.00%	#DIV/0!
	13	100.00%	100.00%	100.00%	100.00%	100.00%	100.00%	100.00%	100.00%	100.00%	100.00%	100.00%	100.00%	100.00%	100.00%	100.00%	100.00%
	14	100.00%	100.00%	100.00%	100.00%	100.00%	100.00%	100.00%	100.00%	100.00%	100.00%	100.00%	100.00%	100.00%	100.00%	100.00%	100.00%
	15	#DIV/0!	100.00%	100.00%	100.00%	100.00%	100.00%	100.00%	100.00%	100.00%	100.00%	100.00%	100.00%	100.00%	100.00%	100.00%	100.00%
	16	#DIV/0!	#DIV/0!	#DIV/0!	#DIV/0!	#DIV/0!	#DIV/0!	#DIV/0!	#DIV/0!	100.00%	100.00%	100.00%	100.00%	#DIV/0!	#DIV/0!	#DIV/0!	#DIV/0!

Table 4. Fidelity results calculated from orientation decoding by ODS unit pattern; the bit errors for  $\Delta O=0$ ,  $\Delta O=\pm 1$ , and  $\Delta O=0, \pm 1$ .

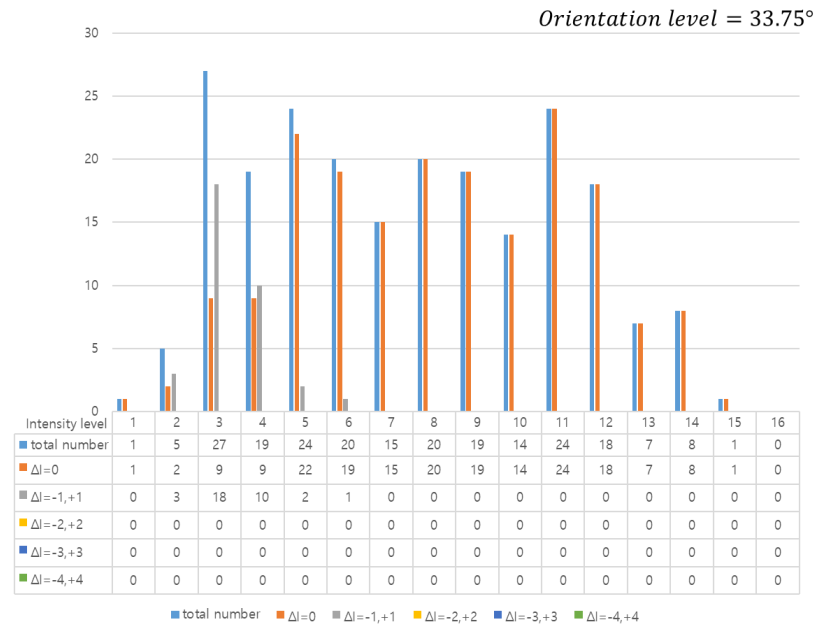
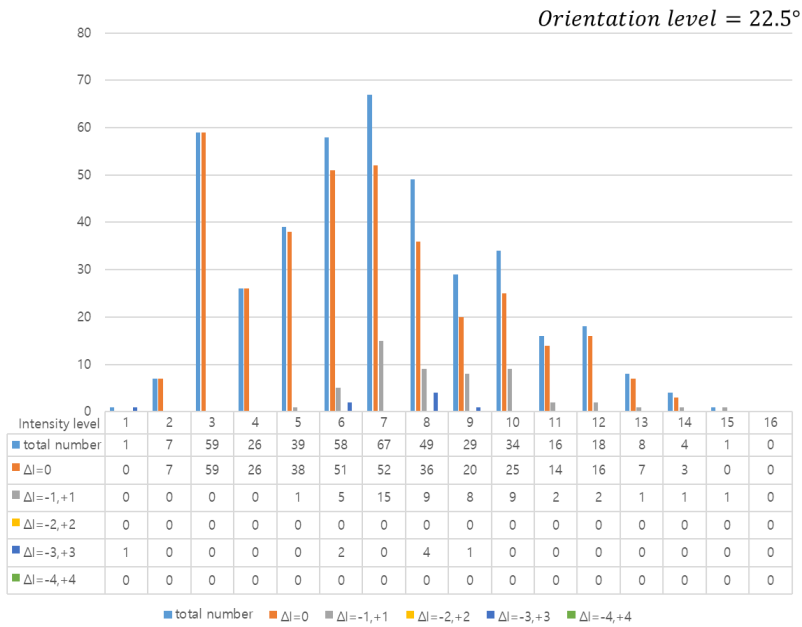
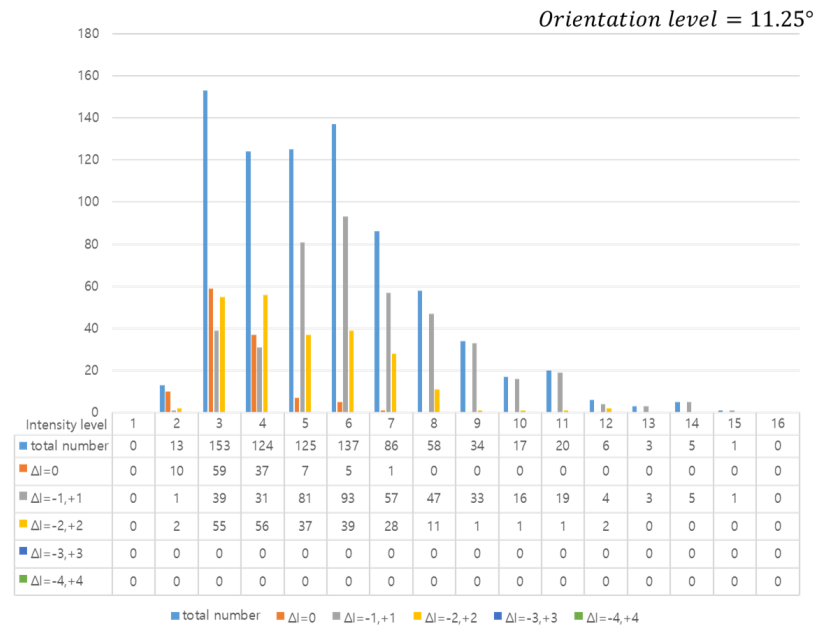
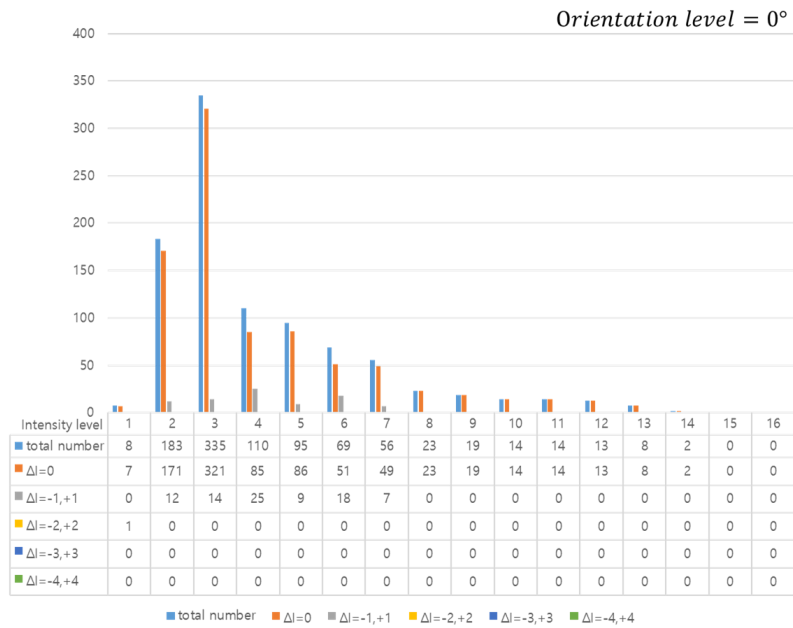


Figure 49. Histogram of retrieving results for each orientation level of orientation decoding; 0°, 11.25°, 22.5°, and 33.75°

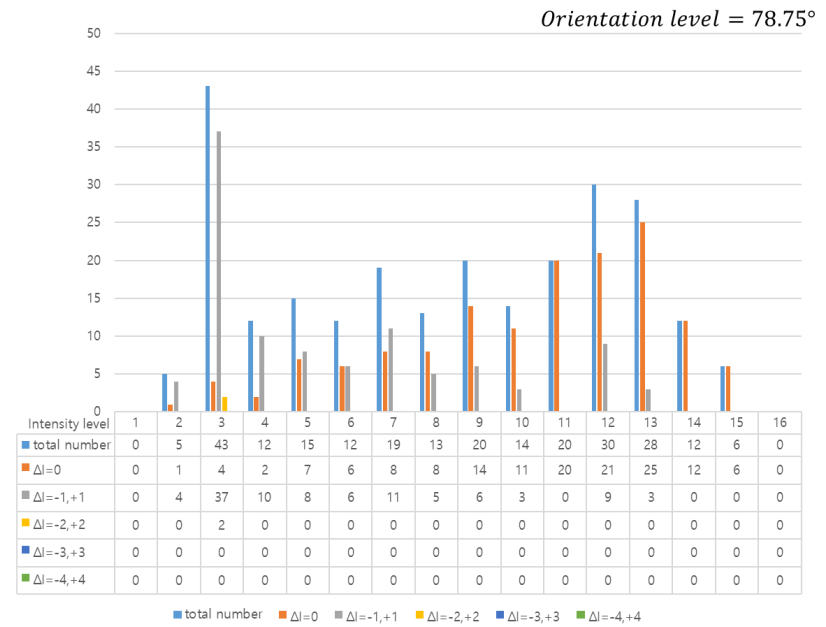
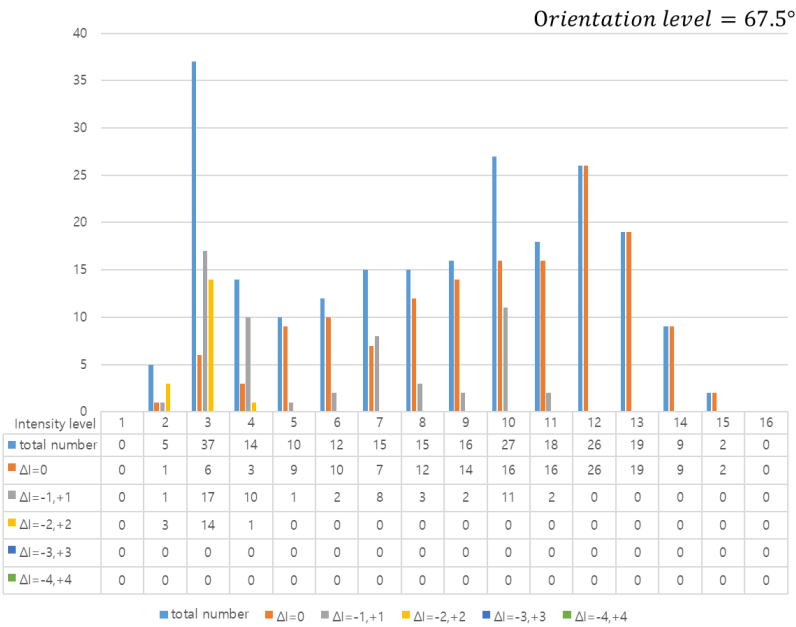
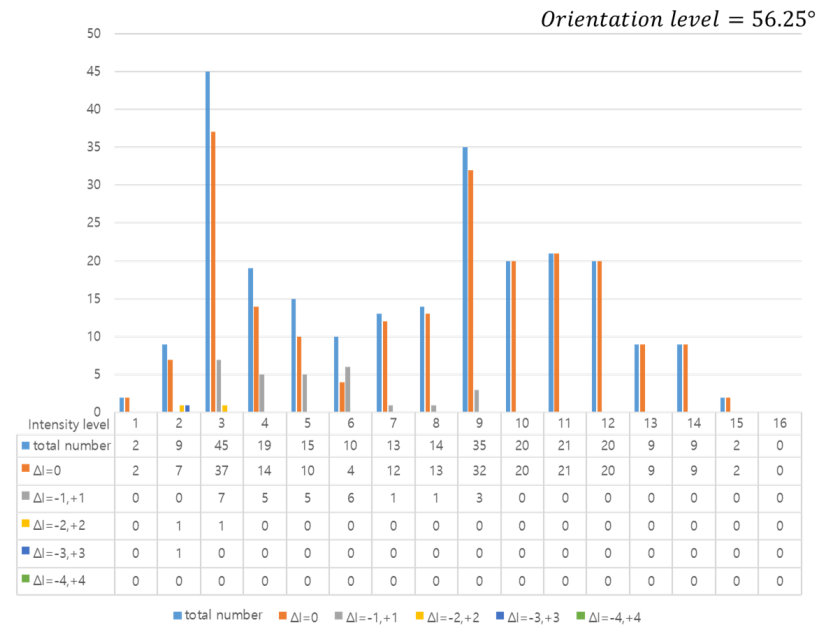
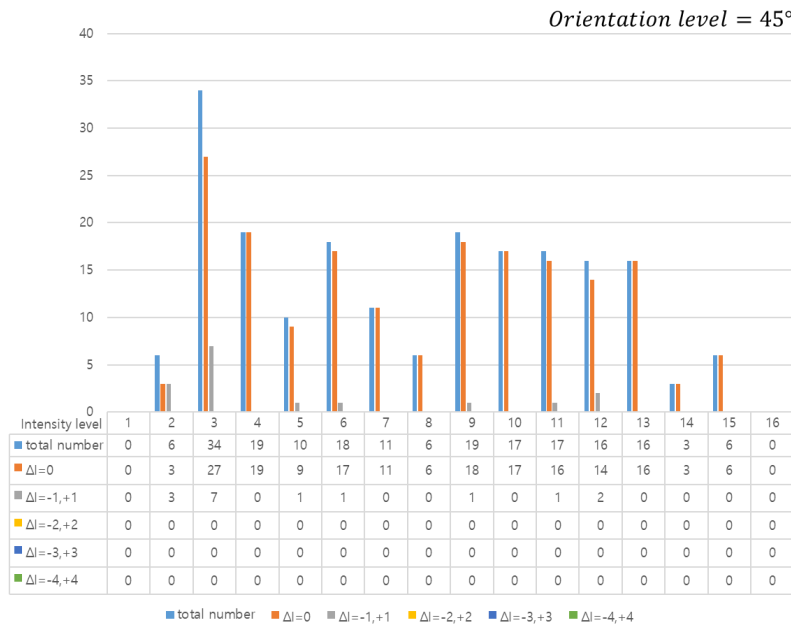


Figure 50. Histogram of retrieving results for each orientation level of orientation decoding; 45°, 56.25°, 67.5°, and 78.75°

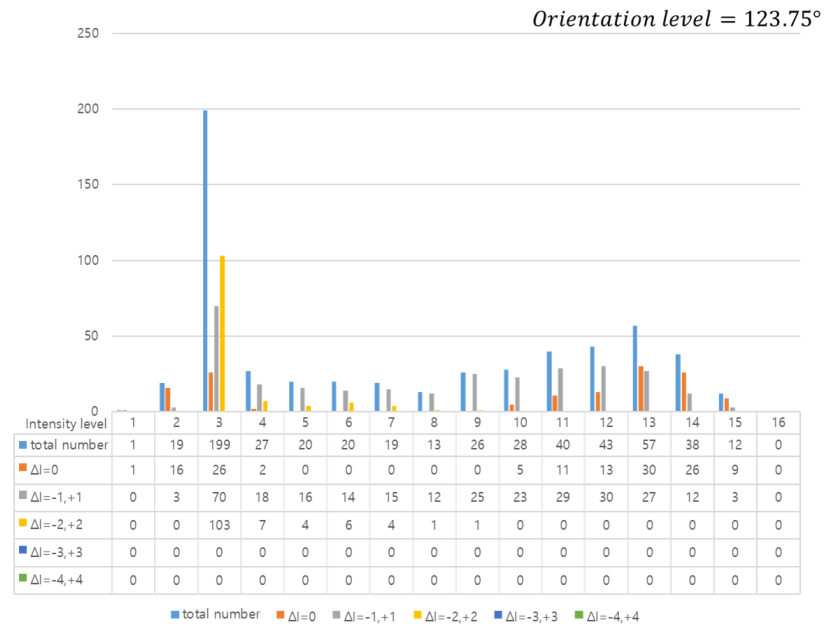
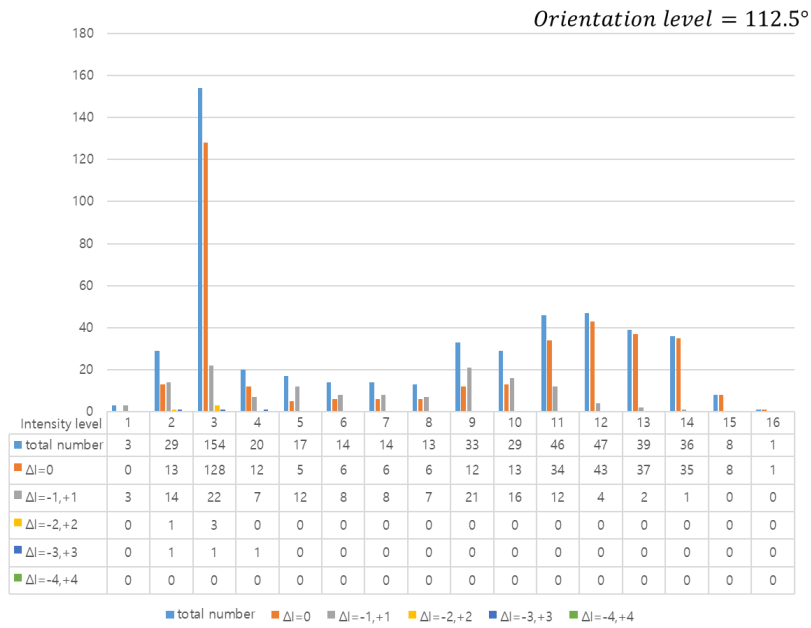
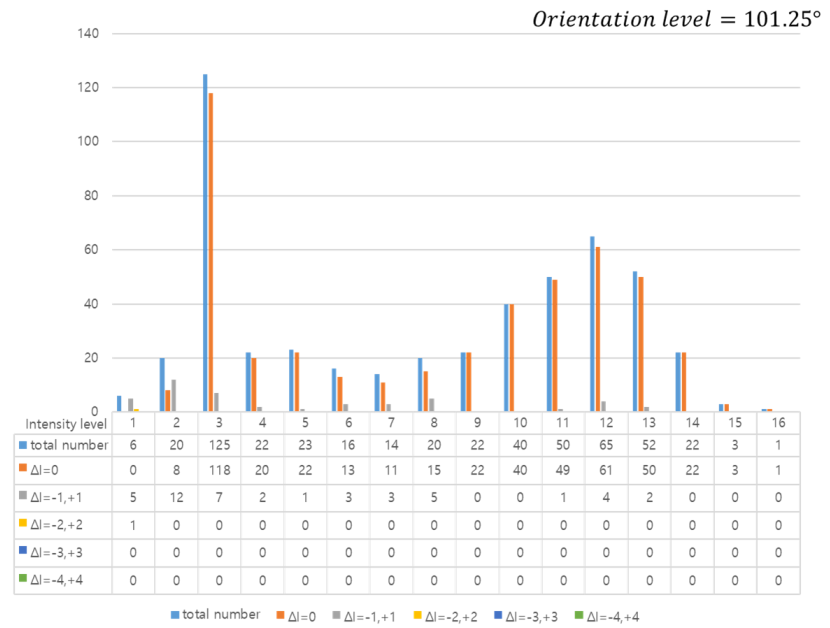
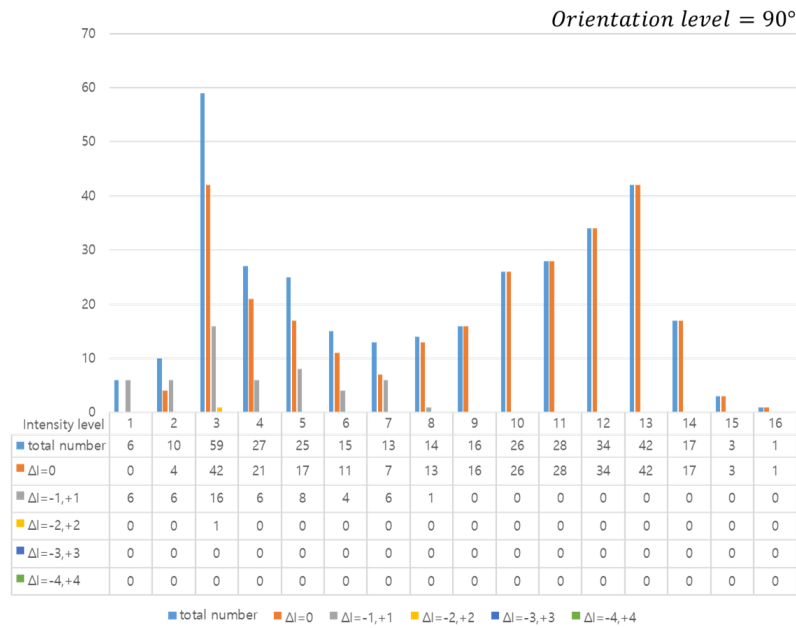


Figure 51. Histogram of retrieving results for each orientation level of orientation decoding; 90°, 101.25°, 112.5°, and 123.75°

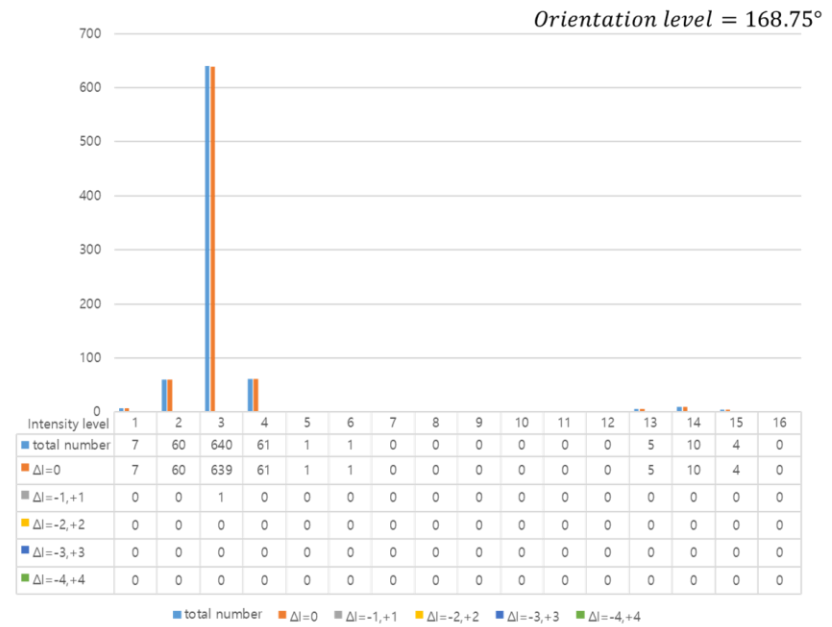
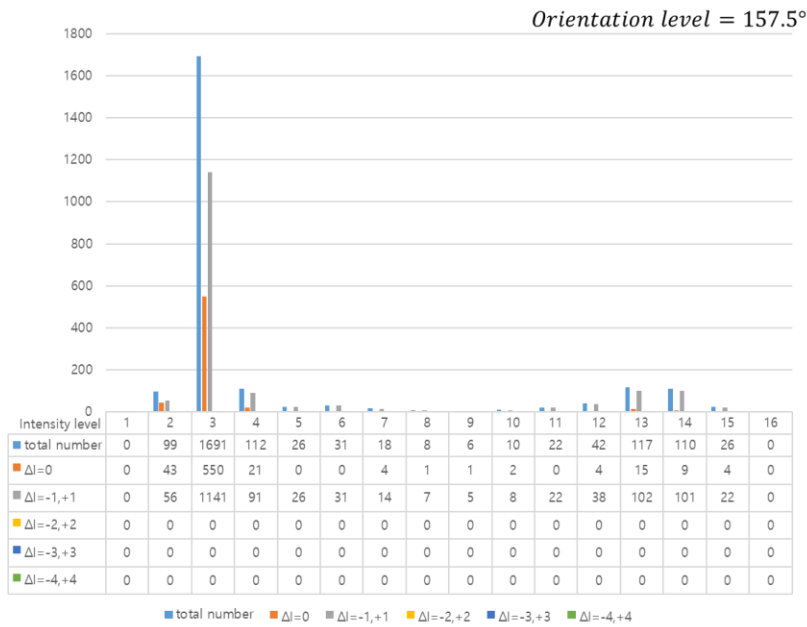
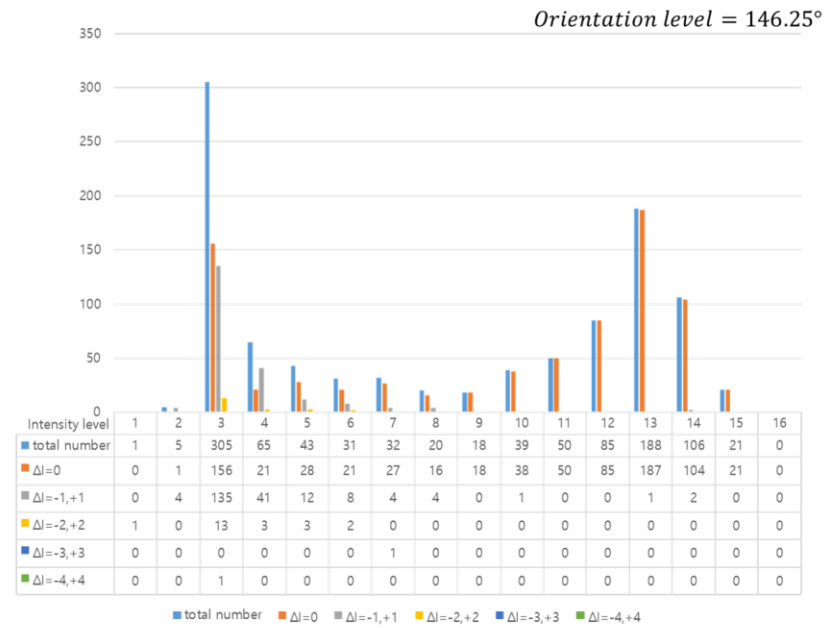
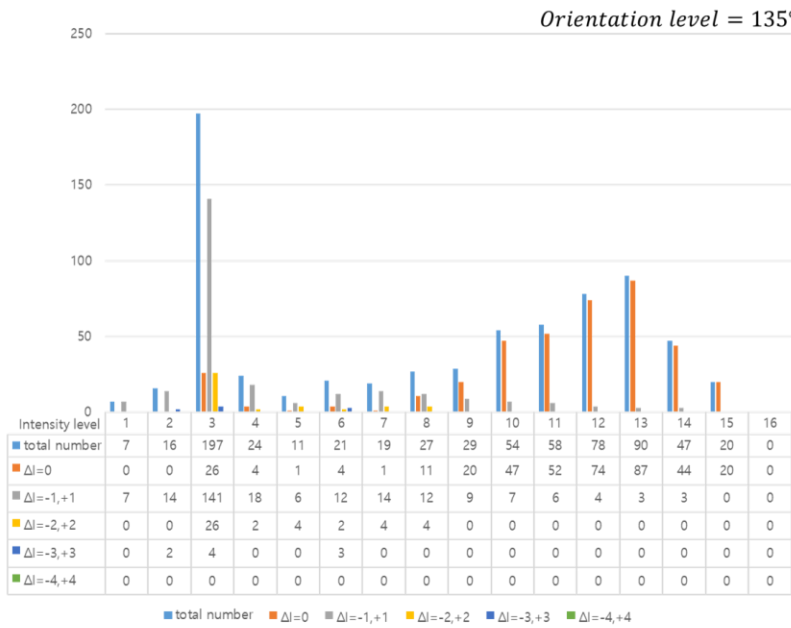


Figure 52. Histogram of retrieving results for each orientation level of orientation decoding; 135°, 146.25°, 157.5°, and 168.75°

$\Delta I=0$		Intensity Level															
		1	2	3	4	5	6	7	8	9	10	11	12	13	14	15	16
Orientation Level	0	0.00%	91.26%	19.10%	26.36%	45.26%	28.99%	42.86%	8.70%	36.84%	0.00%	28.57%	61.54%	0.00%	50.00%	#DIV/0!	#DIV/0!
	11.25	#DIV/0!	46.15%	11.11%	24.19%	0.00%	3.65%	1.16%	3.45%	8.82%	5.88%	5.00%	0.00%	0.00%	0.00%	0.00%	#DIV/0!
	22.5	0.00%	0.00%	89.83%	7.69%	0.00%	12.07%	5.97%	24.49%	48.28%	20.59%	12.50%	0.00%	50.00%	75.00%	100.00%	#DIV/0!
	33.75	0.00%	40.00%	74.07%	0.00%	75.00%	0.00%	0.00%	0.00%	94.74%	7.14%	0.00%	16.67%	0.00%	12.50%	100.00%	#DIV/0!
	45	#DIV/0!	66.67%	23.53%	0.00%	60.00%	0.00%	0.00%	0.00%	42.11%	0.00%	58.82%	62.50%	6.25%	0.00%	0.00%	#DIV/0!
	56.25	0.00%	88.89%	11.11%	5.26%	40.00%	30.00%	0.00%	28.57%	20.00%	20.00%	19.05%	75.00%	0.00%	22.22%	100.00%	#DIV/0!
	67.5	#DIV/0!	0.00%	21.62%	64.29%	0.00%	50.00%	46.67%	13.33%	6.25%	11.11%	50.00%	11.54%	73.68%	0.00%	0.00%	#DIV/0!
	78.75	#DIV/0!	40.00%	9.30%	41.67%	0.00%	0.00%	5.26%	53.85%	35.00%	28.57%	0.00%	6.67%	17.86%	75.00%	83.33%	#DIV/0!
	90	0.00%	60.00%	3.39%	48.15%	0.00%	6.67%	46.15%	21.43%	43.75%	0.00%	25.00%	23.53%	50.00%	47.06%	0.00%	0.00%
	101.25	0.00%	85.00%	2.40%	9.09%	0.00%	25.00%	7.14%	10.00%	4.55%	10.00%	18.00%	21.54%	11.54%	4.55%	66.67%	100.00%
	112.5	0.00%	100.00%	14.94%	0.00%	5.88%	50.00%	35.71%	30.77%	3.03%	0.00%	13.04%	25.53%	61.54%	19.44%	25.00%	0.00%
	123.75	0.00%	100.00%	0.50%	0.00%	0.00%	35.00%	10.53%	15.38%	11.54%	28.57%	30.00%	30.23%	17.54%	68.42%	25.00%	#DIV/0!
	135	0.00%	100.00%	18.78%	4.17%	27.27%	19.05%	5.26%	7.41%	31.03%	14.81%	29.31%	30.77%	17.78%	8.51%	30.00%	#DIV/0!
	146.25	0.00%	60.00%	17.70%	27.69%	32.56%	0.00%	25.00%	10.00%	33.33%	12.82%	58.00%	1.18%	29.79%	42.45%	14.29%	#DIV/0!
	157.5	#DIV/0!	31.31%	40.45%	48.21%	61.54%	3.23%	5.56%	12.50%	0.00%	40.00%	0.00%	0.00%	3.42%	2.73%	0.00%	#DIV/0!
	168.75	0.00%	10.00%	15.78%	13.11%	100.00%	0.00%	#DIV/0!	#DIV/0!	#DIV/0!	#DIV/0!	#DIV/0!	#DIV/0!	40.00%	0.00%	0.00%	#DIV/0!
$\Delta I=\pm 1$		Intensity Level															
		1	2	3	4	5	6	7	8	9	10	11	12	13	14	15	16
Orientation Level	0	87.50%	8.20%	79.70%	45.45%	40.00%	62.32%	16.07%	47.83%	5.26%	71.43%	50.00%	15.38%	100.00%	0.00%	#DIV/0!	#DIV/0!
	11.25	#DIV/0!	23.08%	40.52%	15.32%	6.40%	0.00%	3.49%	5.17%	8.82%	5.88%	35.00%	66.67%	0.00%	60.00%	0.00%	#DIV/0!
	22.5	0.00%	100.00%	10.17%	92.31%	35.90%	18.97%	26.87%	34.69%	37.93%	70.59%	43.75%	72.22%	25.00%	25.00%	0.00%	#DIV/0!
	33.75	100.00%	60.00%	25.93%	94.74%	8.33%	65.00%	0.00%	90.00%	5.26%	92.86%	33.33%	22.22%	28.57%	75.00%	0.00%	#DIV/0!
	45	#DIV/0!	33.33%	76.47%	42.11%	0.00%	83.33%	36.36%	16.67%	15.79%	82.35%	17.65%	18.75%	43.75%	33.33%	50.00%	#DIV/0!
	56.25	100.00%	0.00%	88.89%	15.79%	33.33%	30.00%	61.54%	21.43%	48.57%	50.00%	66.67%	15.00%	100.00%	22.22%	0.00%	#DIV/0!
	67.5	#DIV/0!	40.00%	45.95%	0.00%	80.00%	16.67%	46.67%	46.67%	12.50%	44.44%	0.00%	84.62%	15.79%	100.00%	0.00%	#DIV/0!
	78.75	#DIV/0!	0.00%	72.09%	25.00%	66.67%	25.00%	42.11%	0.00%	30.00%	28.57%	40.00%	40.00%	42.86%	16.67%	16.67%	#DIV/0!
	90	100.00%	0.00%	71.19%	7.41%	60.00%	20.00%	7.69%	64.29%	18.75%	65.38%	7.14%	76.47%	26.19%	41.18%	66.67%	100.00%
	101.25	100.00%	10.00%	89.60%	0.00%	21.74%	37.50%	35.71%	35.00%	4.55%	20.00%	24.00%	52.31%	28.85%	50.00%	0.00%	0.00%
	112.5	100.00%	0.00%	84.42%	10.00%	29.41%	14.29%	50.00%	30.77%	33.33%	6.90%	21.74%	53.19%	17.95%	63.89%	12.50%	100.00%
	123.75	100.00%	0.00%	99.50%	11.11%	30.00%	0.00%	47.37%	30.77%	42.31%	10.71%	40.00%	34.88%	49.12%	18.42%	66.67%	#DIV/0!
	135	100.00%	0.00%	79.70%	54.17%	18.18%	28.57%	26.32%	37.04%	13.79%	50.00%	36.21%	44.87%	20.00%	51.06%	20.00%	#DIV/0!
	146.25	100.00%	20.00%	70.82%	66.15%	4.65%	45.16%	34.38%	40.00%	33.33%	82.05%	16.00%	74.12%	39.36%	31.13%	57.14%	#DIV/0!
	157.5	#DIV/0!	40.40%	46.07%	44.64%	7.69%	58.06%	55.56%	37.50%	50.00%	20.00%	4.55%	9.52%	23.08%	7.27%	15.38%	#DIV/0!
	168.75	57.14%	71.67%	37.03%	83.61%	0.00%	100.00%	#DIV/0!	#DIV/0!	#DIV/0!	#DIV/0!	#DIV/0!	#DIV/0!	0.00%	30.00%	50.00%	#DIV/0!
$\Delta I=0, \pm 1$		Intensity Level															
		1	2	3	4	5	6	7	8	9	10	11	12	13	14	15	16
Orientation Level	0	87.50%	99.45%	98.81%	71.82%	85.26%	91.30%	58.93%	56.52%	42.11%	71.43%	78.57%	76.92%	100.00%	50.00%	#DIV/0!	#DIV/0!
	11.25	#DIV/0!	69.23%	51.63%	39.52%	6.40%	3.65%	4.65%	8.62%	17.65%	11.76%	40.00%	66.67%	0.00%	60.00%	0.00%	#DIV/0!
	22.5	0.00%	100.00%	100.00%	100.00%	35.90%	31.03%	32.84%	59.18%	86.21%	91.18%	56.25%	72.22%	75.00%	100.00%	100.00%	#DIV/0!
	33.75	100.00%	100.00%	100.00%	94.74%	83.33%	65.00%	0.00%	90.00%	100.00%	100.00%	33.33%	38.89%	28.57%	87.50%	100.00%	#DIV/0!
	45	#DIV/0!	100.00%	100.00%	42.11%	60.00%	83.33%	36.36%	16.67%	57.89%	82.35%	76.47%	81.25%	50.00%	33.33%	50.00%	#DIV/0!
	56.25	100.00%	88.89%	100.00%	21.05%	73.33%	60.00%	61.54%	50.00%	68.57%	70.00%	85.71%	90.00%	100.00%	44.44%	100.00%	#DIV/0!
	67.5	#DIV/0!	40.00%	67.57%	64.29%	80.00%	66.67%	93.33%	60.00%	18.75%	55.56%	50.00%	96.15%	89.47%	100.00%	0.00%	#DIV/0!
	78.75	#DIV/0!	40.00%	81.40%	66.67%	66.67%	25.00%	47.37%	53.85%	65.00%	57.14%	40.00%	46.67%	60.71%	91.67%	100.00%	#DIV/0!
	90	100.00%	60.00%	74.58%	55.56%	60.00%	26.67%	53.85%	85.71%	62.50%	65.38%	32.14%	100.00%	76.19%	88.24%	66.67%	100.00%
	101.25	100.00%	95.00%	92.00%	9.09%	21.74%	62.50%	42.86%	45.00%	9.09%	30.00%	42.00%	73.85%	40.38%	54.55%	66.67%	100.00%
	112.5	100.00%	100.00%	99.35%	10.00%	35.29%	64.29%	85.71%	61.54%	36.36%	6.90%	34.78%	78.72%	79.49%	83.33%	37.50%	100.00%
	123.75	100.00%	100.00%	100.00%	11.11%	30.00%	35.00%	57.89%	46.15%	53.85%	39.29%	70.00%	65.12%	66.67%	86.84%	91.67%	#DIV/0!
	135	100.00%	100.00%	98.48%	58.33%	45.45%	47.62%	31.58%	44.44%	44.83%	64.81%	65.52%	75.64%	37.78%	59.57%	50.00%	#DIV/0!
	146.25	100.00%	80.00%	88.52%	93.85%	37.21%	45.16%	59.38%	50.00%	66.67%	94.87%	74.00%	75.29%	69.15%	73.58%	71.43%	#DIV/0!
	157.5	#DIV/0!	71.72%	86.52%	92.86%	69.23%	61.29%	61.11%	50.00%	50.00%	60.00%	4.55%	9.52%	26.50%	10.00%	15.38%	#DIV/0!
	168.75	57.14%	81.67%	52.81%	96.72%	100.00%	100.00%	#DIV/0!	#DIV/0!	#DIV/0!	#DIV/0!	#DIV/0!	#DIV/0!	40.00%	30.00%	50.00%	#DIV/0!

Table 5. Fidelity results calculated from intensity decoding by ODS unit pattern; the bit errors for  $\Delta I=0$ ,  $\Delta I=\pm 1$ , and  $\Delta I=0, \pm 1$ .

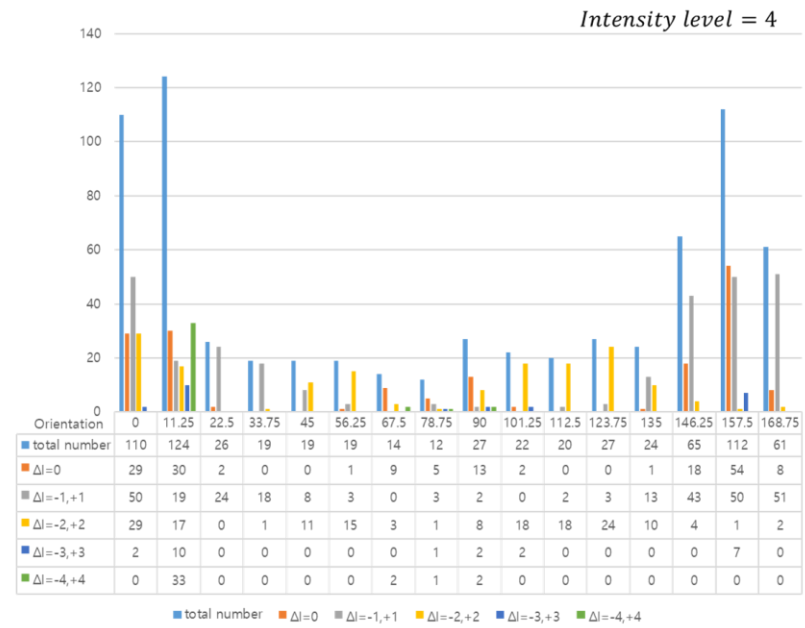
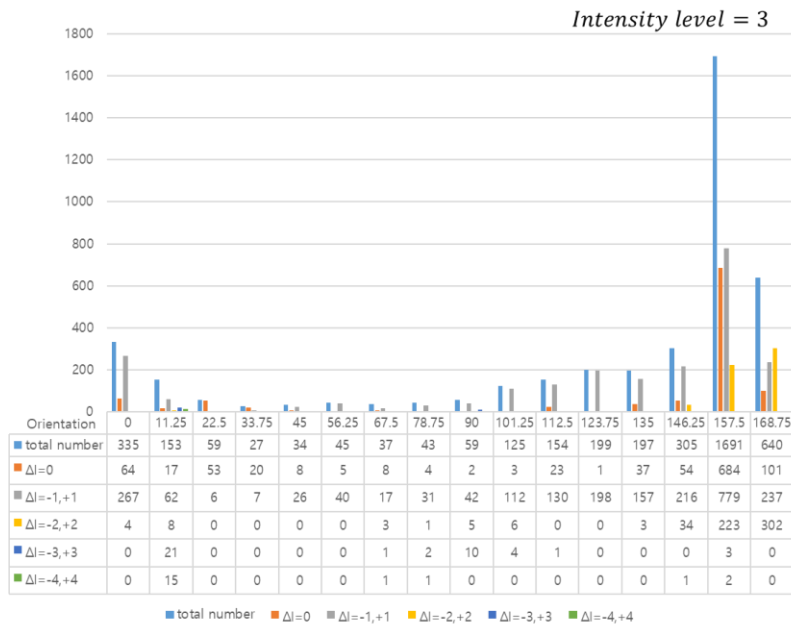
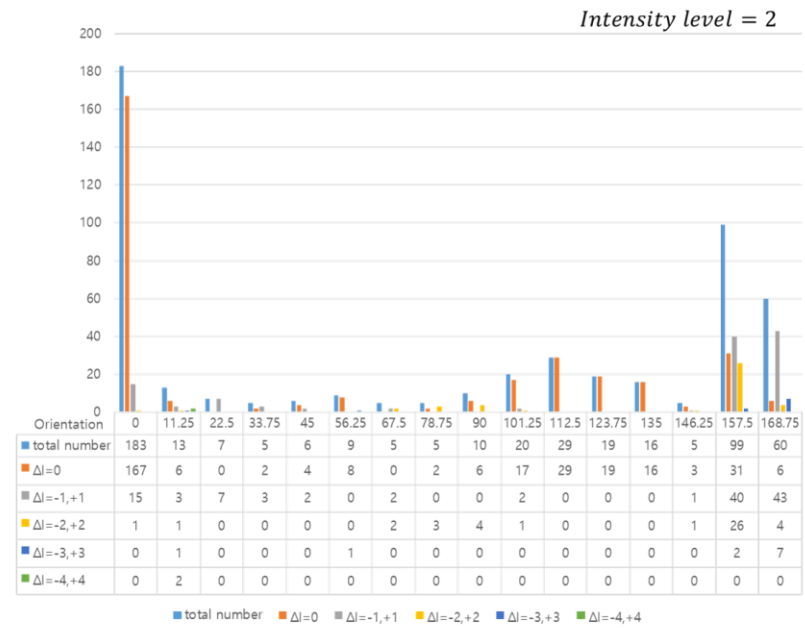
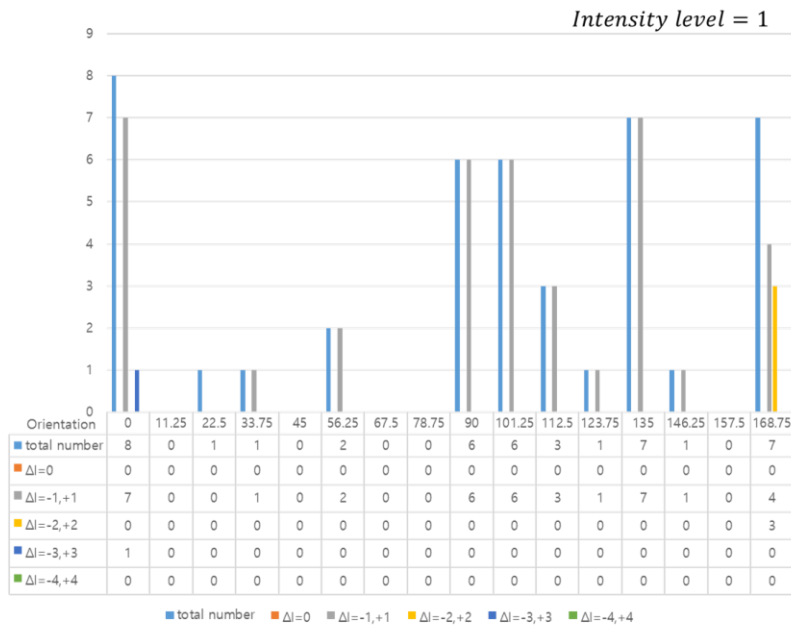


Figure 53. Histogram of retrieving results for each intensity level of intensity decoding; 1, 2, 3, and 4

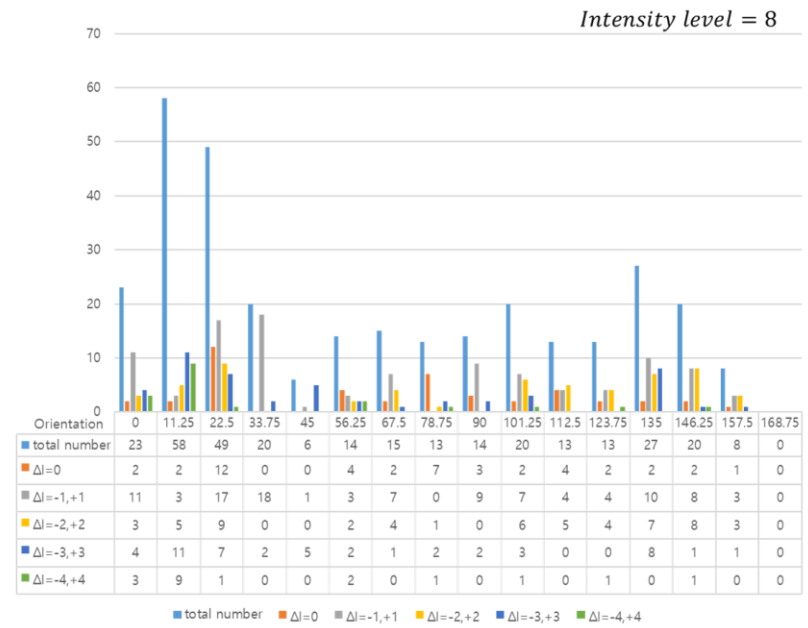
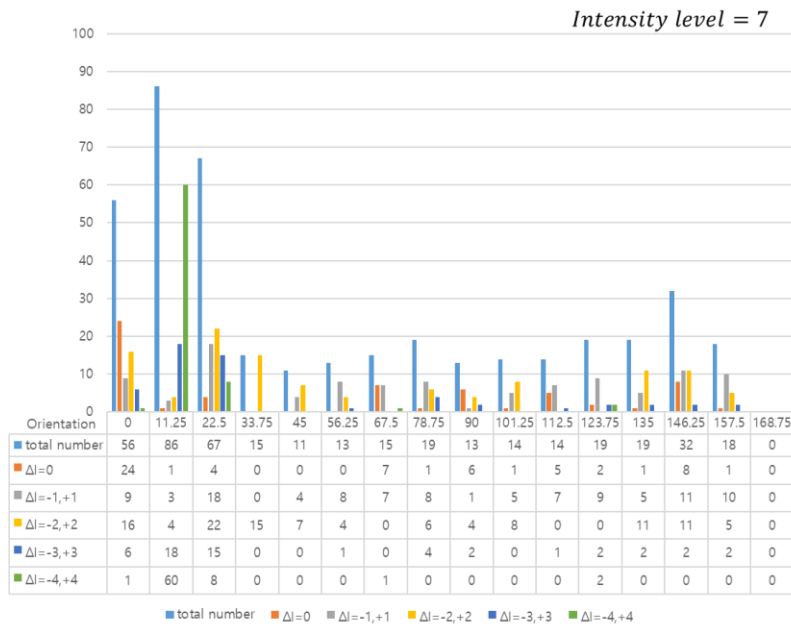
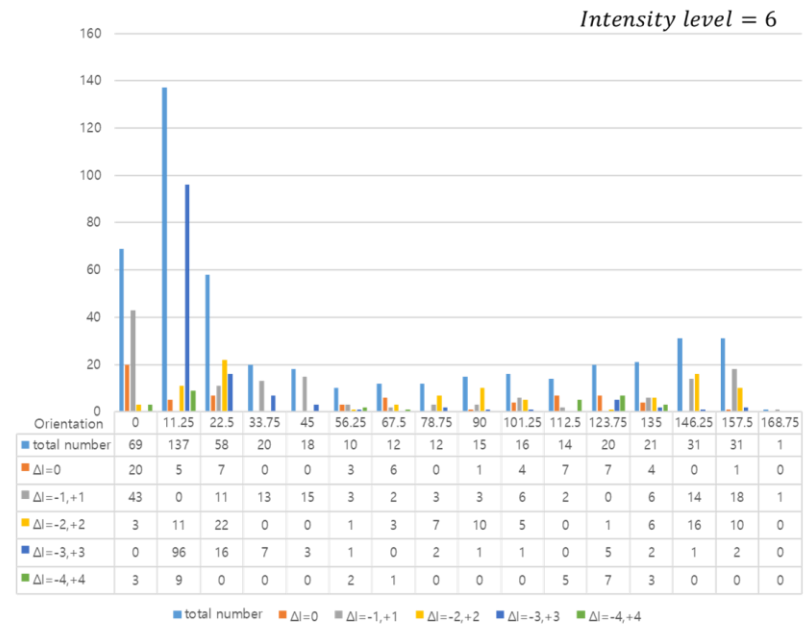
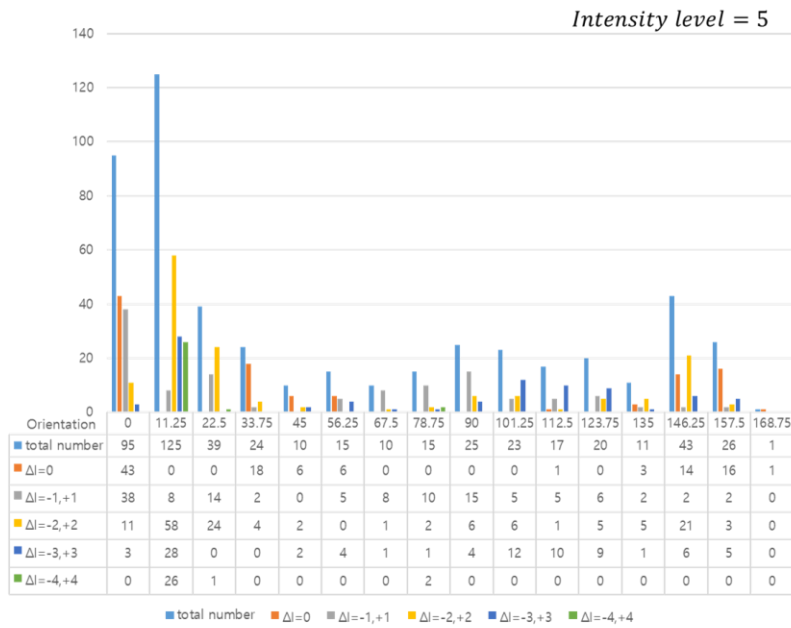


Figure 54. Histogram of retrieving results for each intensity level of intensity decoding; 5, 6, 7, and 8

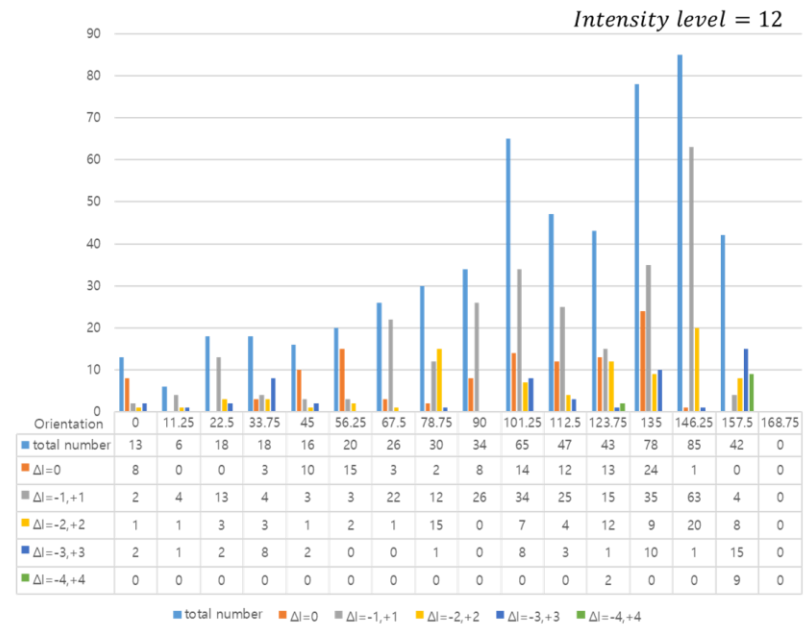
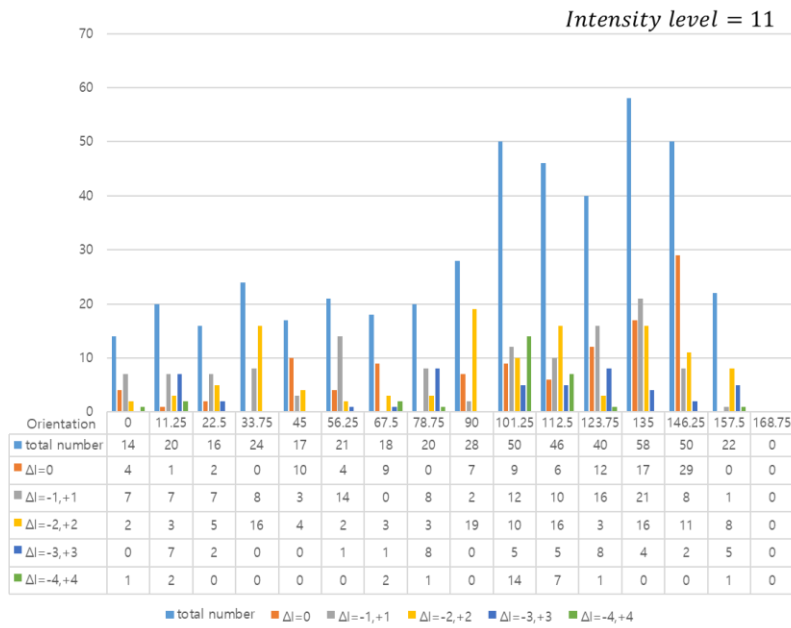
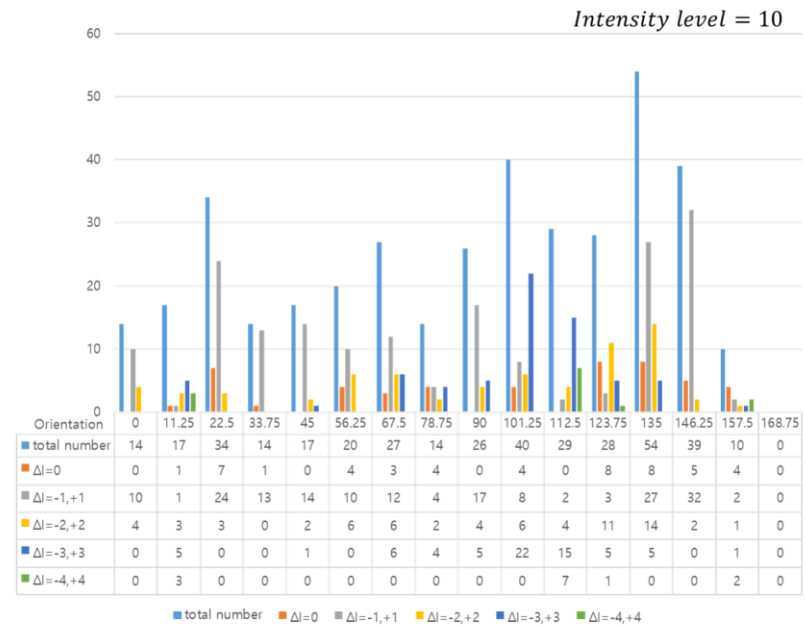
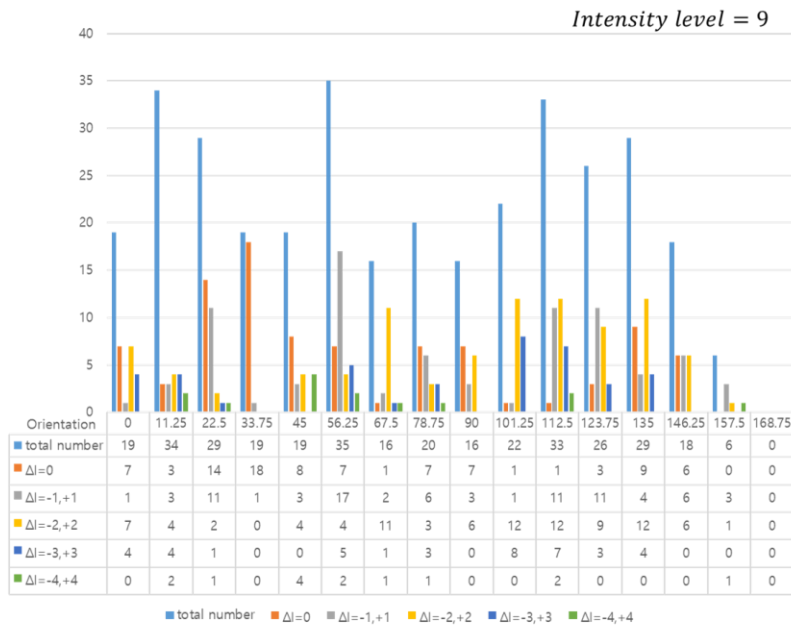


Figure 55. Histogram of retrieving results for each intensity level of intensity decoding; 9, 10, 11, and 12

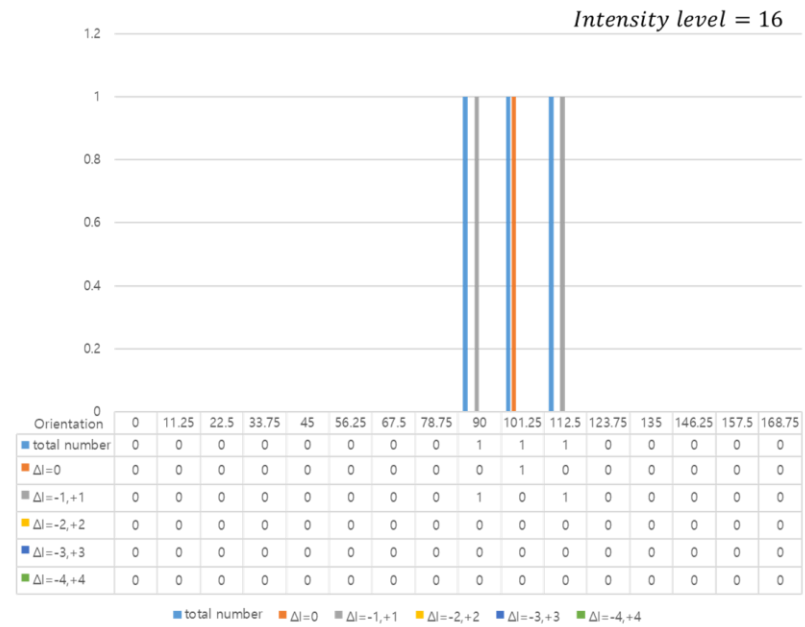
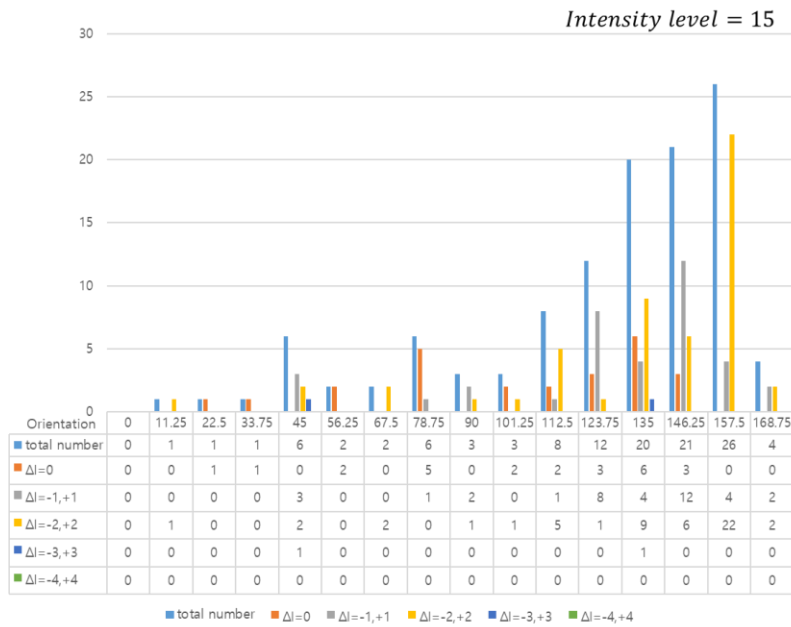
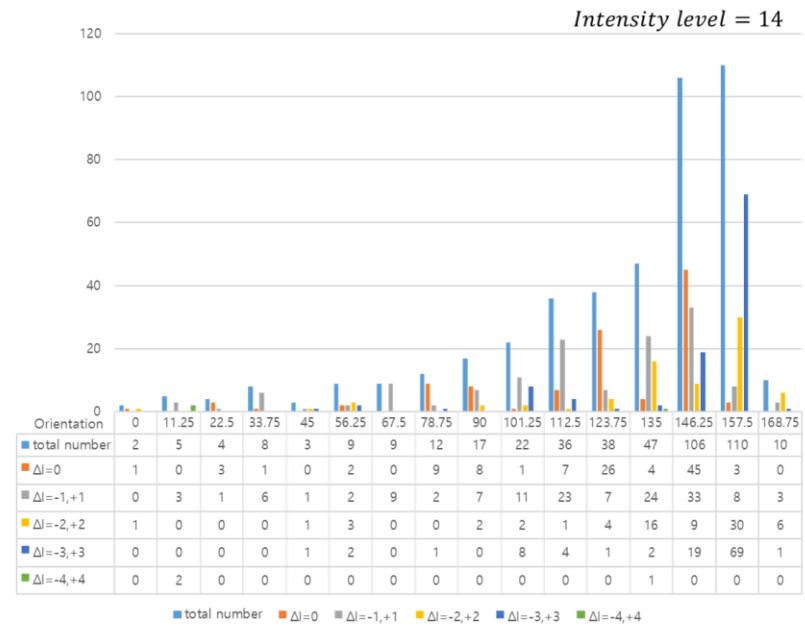
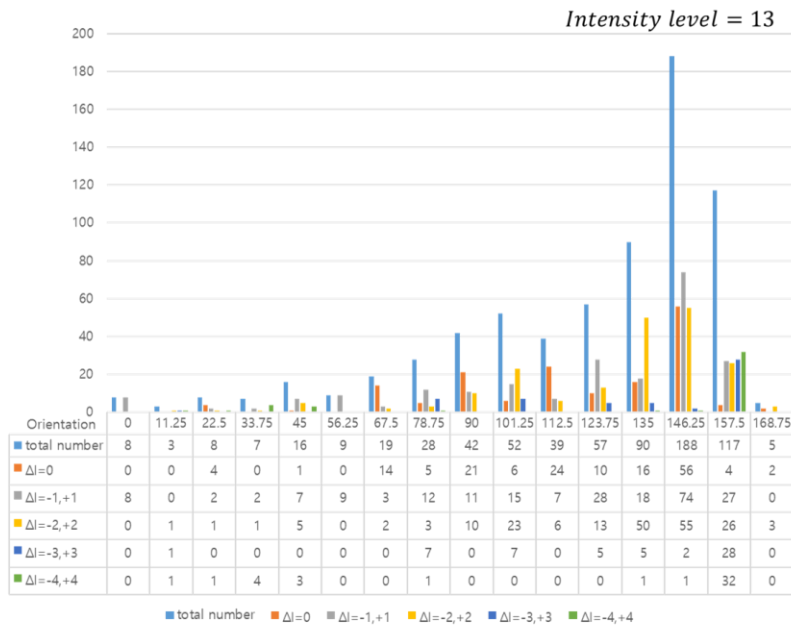


Figure 56. Histogram of retrieving results for each intensity level of intensity decoding; 13, 14, 15, and 16

## 5. 6 Reading process with 64 levels: 8 levels for fluorescence intensity and 8 levels for orientation of ellipse

As shown in Section 5.5, including two adjacent levels improves the accuracy of decoding while correlatively accepting to reduce the number of both orientation and intensity encoding levels, reducing thus the reading level resolution. Therefore, Figure 57(a) and Figure 57(b) represent the decoding of Figure 47(c) while considering only  $2^3 = 8$  ellipse orientation levels and  $2^3 = 8$  fluorescence intensity levels. The reading fidelity obtained from orientation direction and fluorescence intensity levels was 85% and 47%, respectively. The 3-bit orientation readout errors showed 15% 1-bit error and no higher-bit error. The 3-bit orientation readout error showed 43% 1-bit error and 10% 2-bit (or more) error. Figure 57 (c) and Figure 57(d) display the level difference between the original and retrieved images with respect to orientation angle and laser irradiance. Figure 57(e) shows the histogram of the level difference between original and decoded levels for the orientation angle ( $\Delta O'$ ). The accuracy increased from 85% to 99.82% if adjacent levels of  $\Delta O' = \pm 1$  was included. Figure 57(f) indicates the histogram of the level difference between original and the decoded levels for the fluorescence intensity ( $\Delta I'$ ). The accuracy increased from 47% to 90.15% when including adjacent level of  $\Delta I' = \pm 1$ .

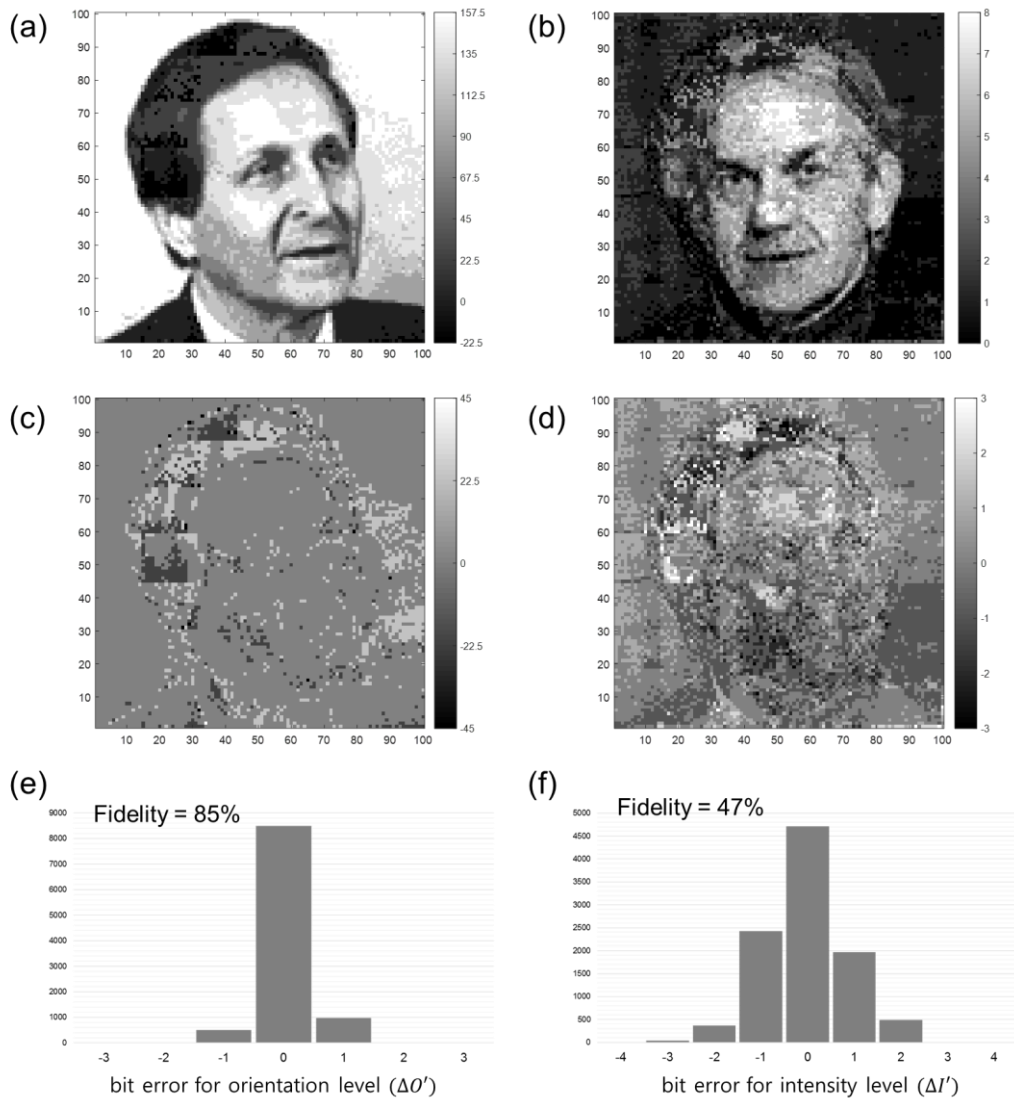


Figure 57. (a) Retrieved image from the initial image in Figure 47(a); (b) Retrieved image from the initial image in Figure 47(b); (c) Level difference between Figure 47(a) and 25(a); (d) Level difference between Figure 47(b) and 25(b); (e) Histogram of the level difference between original and decoded levels for the orientation direction; (f) Histogram of the level difference between original and decoded levels for the fluorescence intensity.

Table 6 shows the summary of the writing/reading accuracy. In the case of orientation, reading accuracy remains about 60.5% when decoded for the 16 levels. It is increased from

60.5% to 85.0% when decoded at 8 levels. For the fluorescence intensity, the reading accuracy increases accordingly from 25.1% to 47.1%. Considering simultaneously both irradiance and orientation degrees of freedom, the overall 8-bit readout ( $2^4 \times 2^4 = 2^8 = 256$  levels) has led to information coding (inscription and readout processes) with a fidelity of 14.24%. Similarly, the overall 6-bit readout ( $2^3 \times 2^3 = 2^6 = 64$  levels) has led to information coding (inscription and readout processes) with a fidelity of 43.66%. By considering (i) a fluorescence microscope with a better response homogeneity, (ii) a laser source with a better stabilized pulse train and (iii) by managing to reduce any intrinsic laser astigmatism and/or any experimental misalignment between the laser and the SLM, there is no doubt that accuracy can be improved even further. Indeed, any orientation and/or intensity error that may directly be encoded in the calibration matrix systematically leads to subsequent artificial additional retrieving error, which degrades the fidelity of the overall process.

Method	Orientation Level Retrieval		Intensity Level Retrieval		Overall Level Retrieval	
	$\Delta O = 0$	$\Delta O = 0, \pm 1$	$\Delta I = 0$	$\Delta I = 0, \pm 1$	$\Delta O = 0$ and $\Delta I = 0$	$\Delta O = 0, \pm 1$ and $\Delta I = 0, \pm 1$
16 x 16 Level Writing → 16 x 16 Level Reading	60.54%	95.25%	25.14%	68.11%	14.24%	66.30%
16 x 16 Level Writing → 8 x 8 Level Reading	85.00%	99.82%	47.14%	90.15%	43.66%	90.98%

Table 6. Summary of the writing/reading accuracy

For a more in-depth analysis, Table 7, Table 8, Figure 58, Figure 59, Figure 60, and Figure 61 show the results of each orientation / intensity level for 64 unit patterns. Table 7, Figure 58, and Figure 59 are the results for orientation downgrade-decoding, and Table 8, Figure 60, and Figure 61 are the results for intensity downgrade-decoding. In Table 7, in

the case of  $\Delta O'=0$  compared to 4-bit decoding, it has improved results but still has poor retrieved results for certain orientations ( $0^\circ$ ,  $112.5^\circ$ ,  $135^\circ$ ). Downgrade-decoding results for each orientation / intensity can be found in histogram with the following detailed analysis. Number of patterns used, retrieving result, and errors.

$\Delta O'=0$		Orientation level							
		0	22.5	45	67.5	90	112.5	135	157.5
Intensity level	1	92.65%	92.86%	88.24%	30.00%	57.14%	90.38%	24.14%	100.00%
	2	73.13%	100.00%	94.87%	39.62%	97.00%	61.00%	61.59%	100.00%
	3	35.45%	98.58%	92.45%	71.43%	92.41%	57.75%	67.92%	100.00%
	4	32.74%	97.35%	100.00%	75.81%	98.36%	64.41%	82.65%	100.00%
	5	39.29%	98.96%	98.90%	88.31%	100.00%	63.79%	100.00%	100.00%
	6	50.94%	100.00%	95.95%	91.49%	100.00%	85.23%	100.00%	100.00%
	7	55.56%	100.00%	100.00%	95.59%	100.00%	90.59%	98.61%	100.00%
	8	0.00%	100.00%	100.00%	100.00%	100.00%	90.48%	100.00%	100.00%

$\Delta O'=-1,+1$		Orientation level							
		0	22.5	45	67.5	90	112.5	135	157.5
Intensity level	1	7.35%	0.00%	5.88%	70.00%	42.86%	9.62%	68.97%	0.00%
	2	26.87%	0.00%	5.13%	60.38%	3.00%	39.00%	37.56%	0.00%
	3	64.55%	0.00%	7.55%	28.57%	7.59%	42.25%	29.25%	0.00%
	4	67.26%	0.00%	0.00%	24.19%	1.64%	35.59%	17.35%	0.00%
	5	60.71%	0.00%	1.10%	11.69%	0.00%	36.21%	0.00%	0.00%
	6	49.06%	0.00%	4.05%	8.51%	0.00%	14.77%	0.00%	0.00%
	7	44.44%	0.00%	0.00%	4.41%	0.00%	9.41%	1.39%	0.00%
	8	100.00%	0.00%	0.00%	0.00%	0.00%	9.52%	0.00%	0.00%

$\Delta O'=-1, 0, +1$		Orientation level							
		0	22.5	45	67.5	90	112.5	135	157.5
Intensity level	1	100.00%	92.86%	94.12%	100.00%	100.00%	100.00%	93.10%	100.00%
	2	100.00%	100.00%	100.00%	100.00%	100.00%	100.00%	99.15%	100.00%
	3	100.00%	98.58%	100.00%	100.00%	100.00%	100.00%	97.17%	100.00%
	4	100.00%	97.35%	100.00%	100.00%	100.00%	100.00%	100.00%	100.00%
	5	100.00%	98.96%	100.00%	100.00%	100.00%	100.00%	100.00%	100.00%
	6	100.00%	100.00%	100.00%	100.00%	100.00%	100.00%	100.00%	100.00%
	7	100.00%	100.00%	100.00%	100.00%	100.00%	100.00%	100.00%	100.00%
	8	100.00%	100.00%	100.00%	100.00%	100.00%	100.00%	100.00%	100.00%

Table 7. Fidelity results calculated from orientation downgrade-decoding by ODS unit pattern; the bit errors for  $\Delta O'=0$ ,  $\Delta O'=\pm 1$ , and  $\Delta O'=0, \pm 1$ .

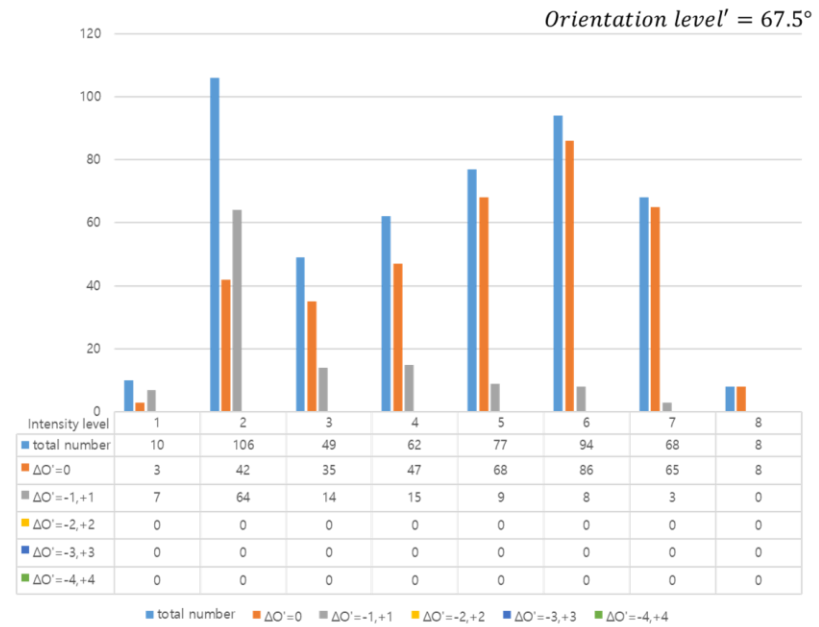
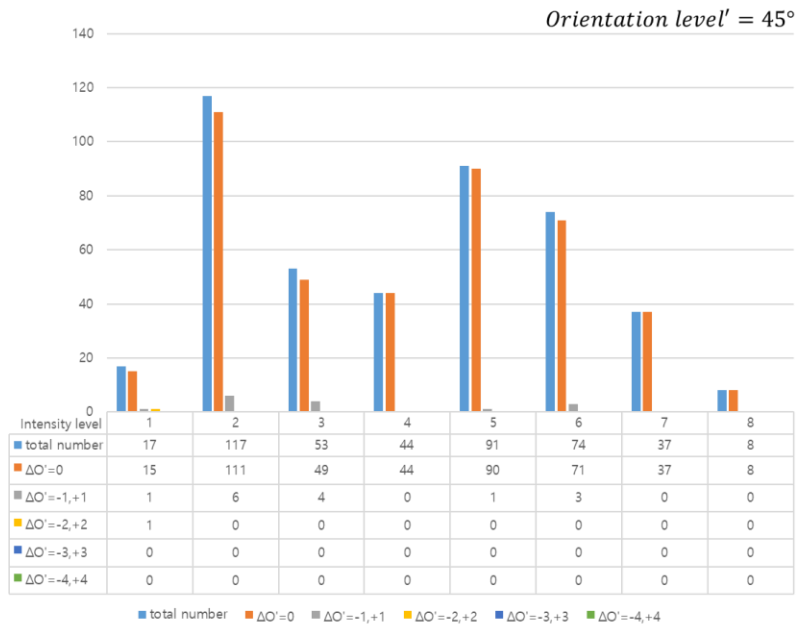
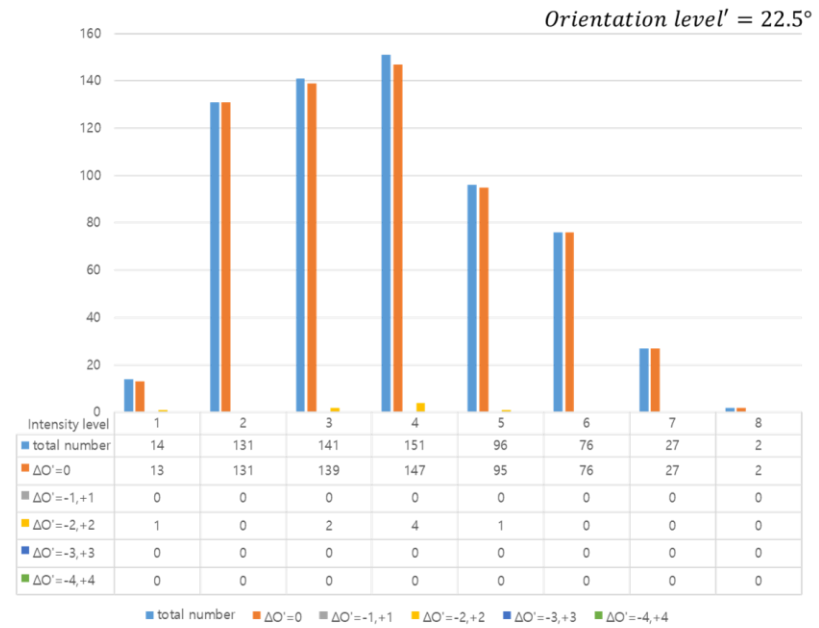
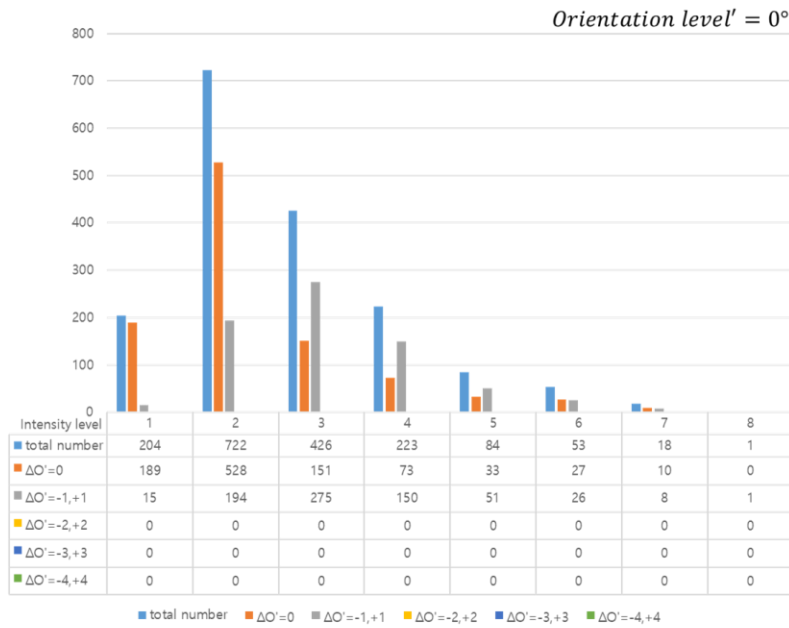


Figure 58. Histogram of retrieving results for each orientation level of orientation downgrade-decoding; 0°, 22.5°, 45°, and 67.5°

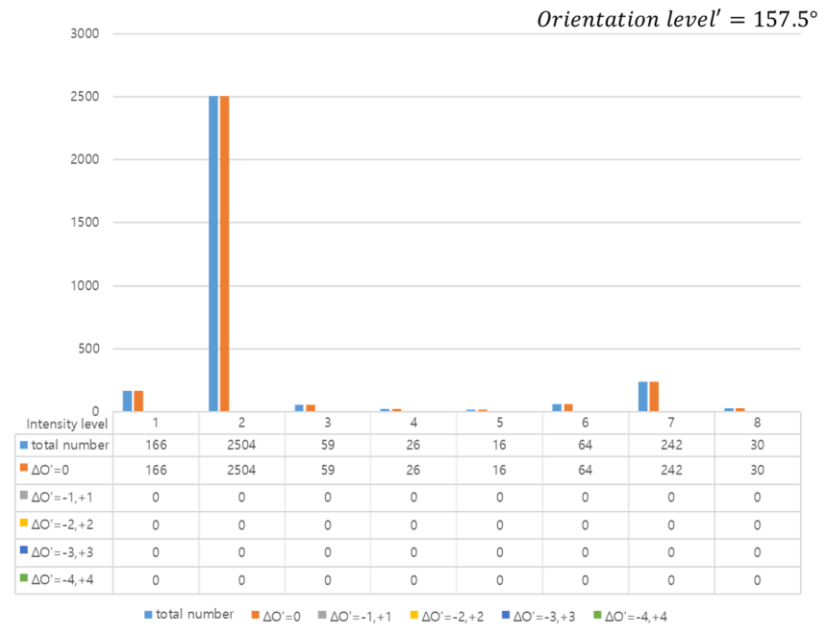
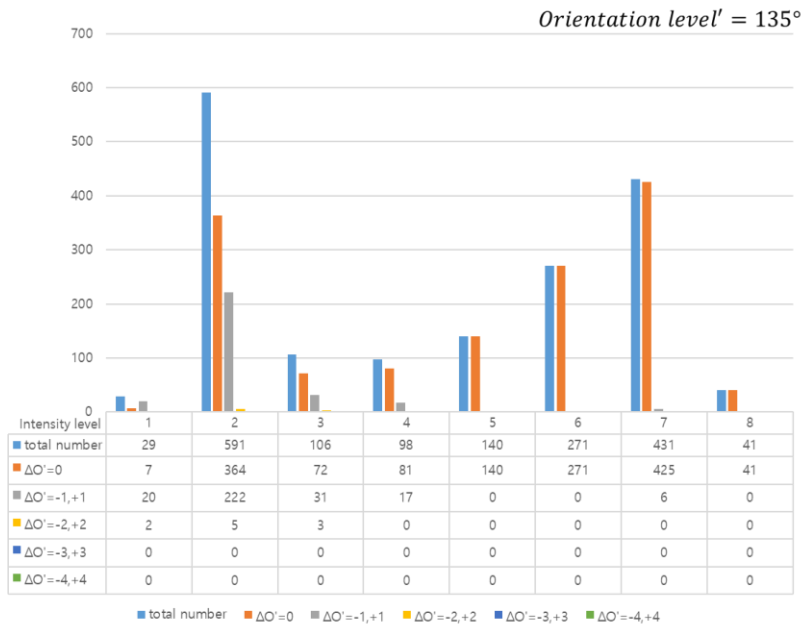
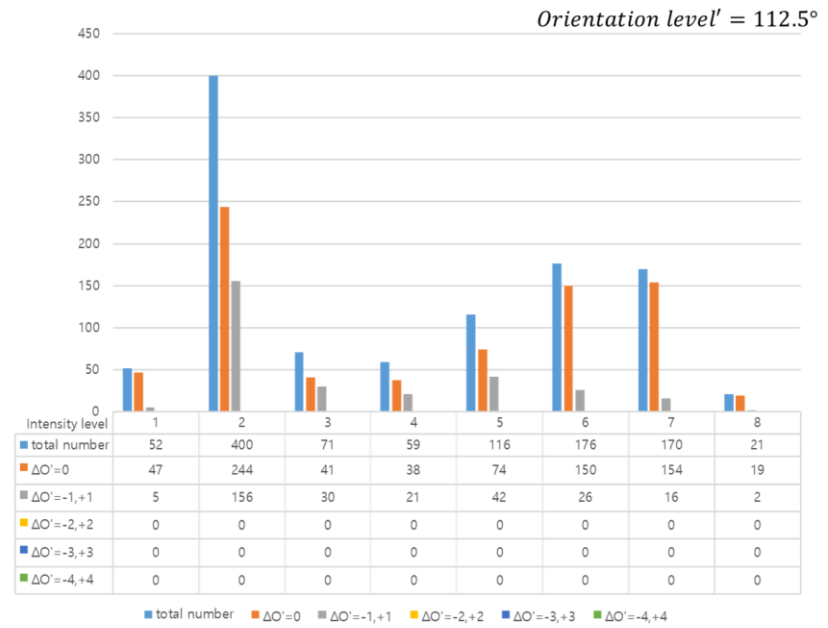
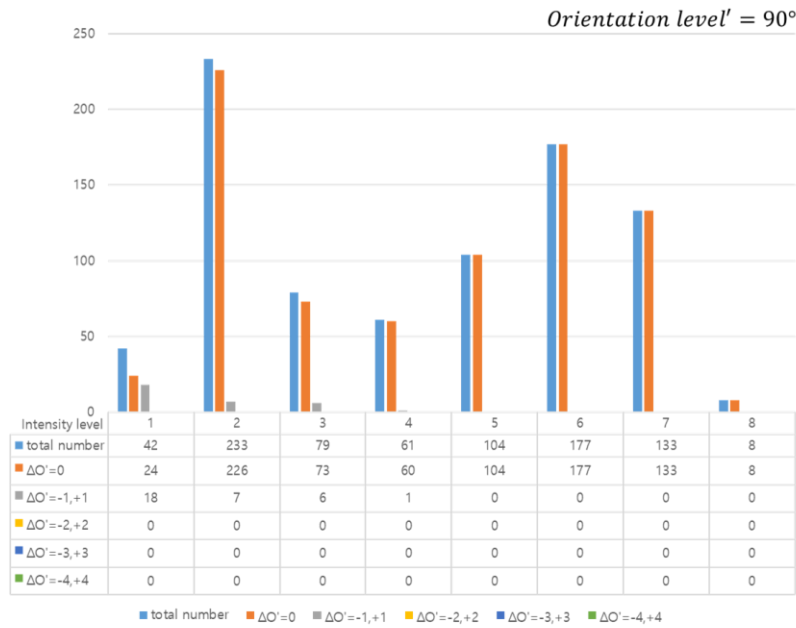


Figure 59. Histogram of retrieving results for each orientation level of orientation downgrade-decoding; 90°, 112.5°, 135°, and 157.5°

$\Delta l'=0$		Intensity level							
		1	2	3	4	5	6	7	8
Orientation level	0	88.24%	34.63%	26.76%	17.49%	23.81%	41.51%	22.22%	0.00%
	22.5	21.43%	91.60%	32.62%	21.19%	76.04%	15.79%	48.15%	100.00%
	45	82.35%	21.37%	56.60%	34.09%	43.96%	72.97%	13.51%	62.50%
	67.5	20.00%	60.38%	28.57%	53.23%	29.87%	35.11%	67.65%	62.50%
	90	83.33%	17.17%	17.72%	36.07%	23.08%	53.67%	34.59%	50.00%
	112.5	100.00%	7.25%	35.21%	37.29%	15.52%	42.61%	60.59%	57.14%
	135	93.10%	48.73%	26.42%	39.80%	40.71%	54.61%	53.36%	34.15%
	157.5	24.70%	71.73%	52.54%	46.15%	43.75%	0.00%	14.88%	20.00%

$\Delta l'=-1,+1$		Intensity level							
		1	2	3	4	5	6	7	8
Orientation level	0	10.29%	50.83%	50.00%	26.46%	39.29%	39.62%	55.56%	100.00%
	22.5	71.43%	8.40%	60.28%	61.59%	21.88%	82.89%	29.63%	0.00%
	45	11.76%	78.63%	28.30%	54.55%	48.35%	27.03%	70.27%	25.00%
	67.5	70.00%	22.64%	59.18%	30.65%	58.44%	51.06%	20.59%	37.50%
	90	16.67%	80.26%	65.82%	49.18%	66.35%	32.20%	59.40%	50.00%
	112.5	0.00%	92.75%	21.13%	40.68%	63.79%	43.75%	33.53%	42.86%
	135	6.90%	51.10%	68.87%	52.04%	59.29%	42.44%	42.92%	63.41%
	157.5	69.88%	27.92%	44.07%	50.00%	25.00%	40.63%	42.98%	80.00%

$\Delta l'=-1, 0, +1$		Intensity level							
		1	2	3	4	5	6	7	8
Orientation level	0	98.53%	85.46%	76.76%	43.95%	63.10%	81.13%	77.78%	100.00%
	22.5	92.86%	100.00%	92.91%	82.78%	97.92%	98.68%	77.78%	100.00%
	45	94.12%	100.00%	84.91%	88.64%	92.31%	100.00%	83.78%	87.50%
	67.5	90.00%	83.02%	87.76%	83.87%	88.31%	86.17%	88.24%	100.00%
	90	100.00%	97.42%	83.54%	85.25%	89.42%	85.88%	93.98%	100.00%
	112.5	100.00%	100.00%	56.34%	77.97%	79.31%	86.36%	94.12%	100.00%
	135	100.00%	99.83%	95.28%	91.84%	100.00%	97.05%	96.29%	97.56%
	157.5	94.58%	99.64%	96.61%	96.15%	68.75%	40.63%	57.85%	100.00%

Table 8. Fidelity results calculated from intensity downgrade-decoding by ODS unit pattern; the bit errors for  $\Delta l'=0$ ,  $\Delta l'=\pm 1$ , and  $\Delta l'=0, \pm 1$ .

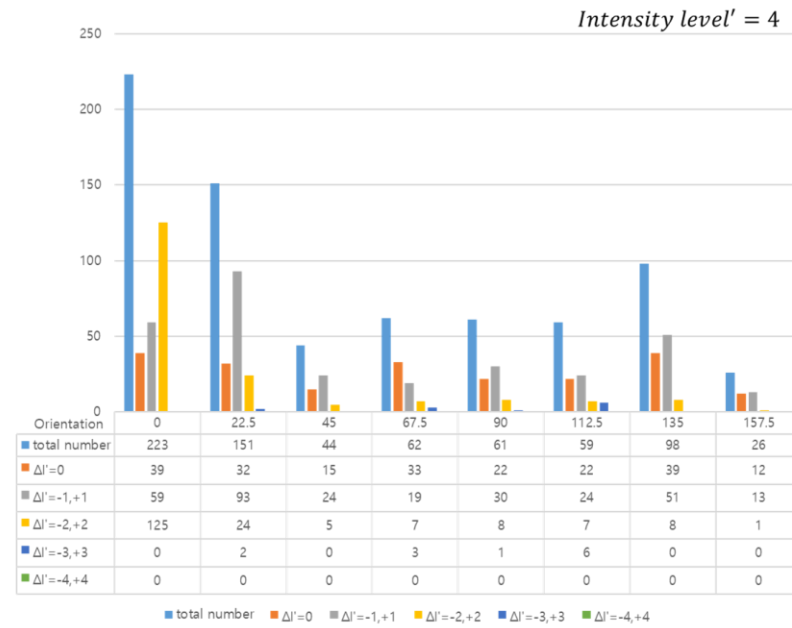
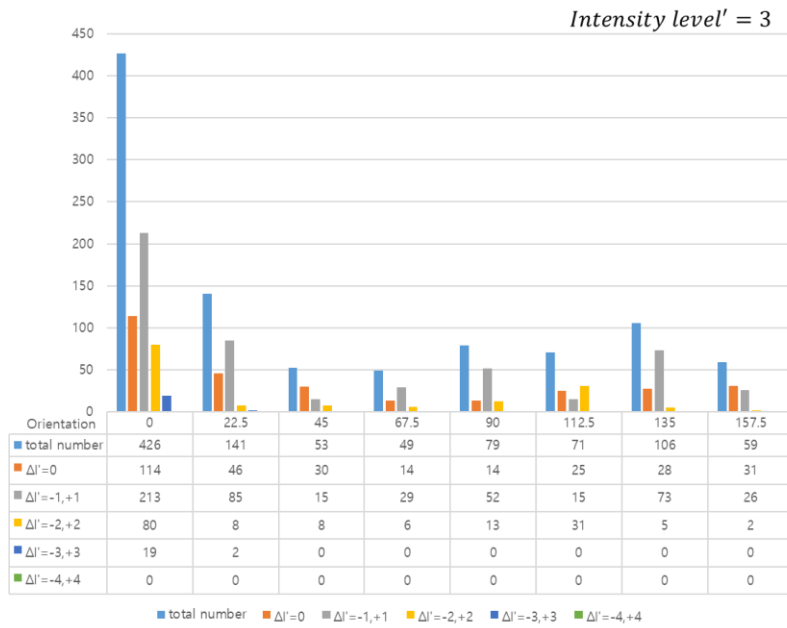
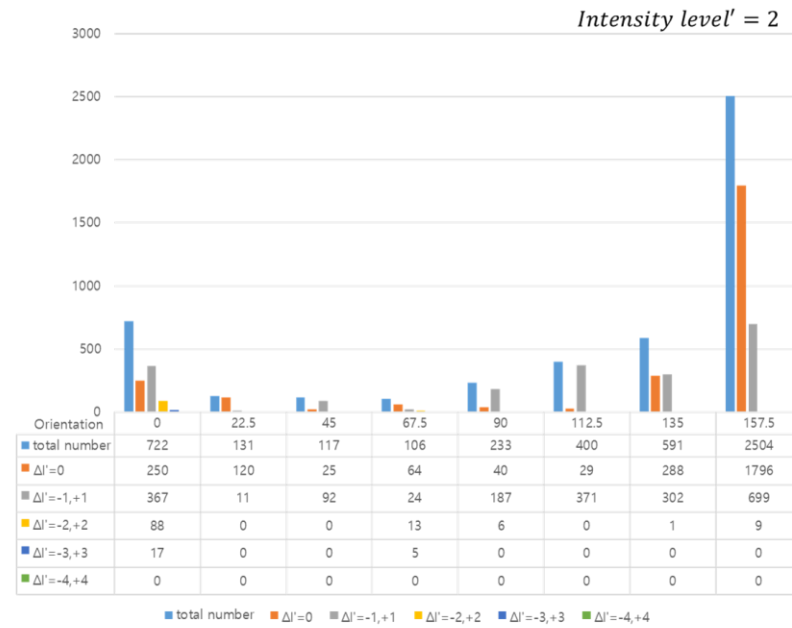
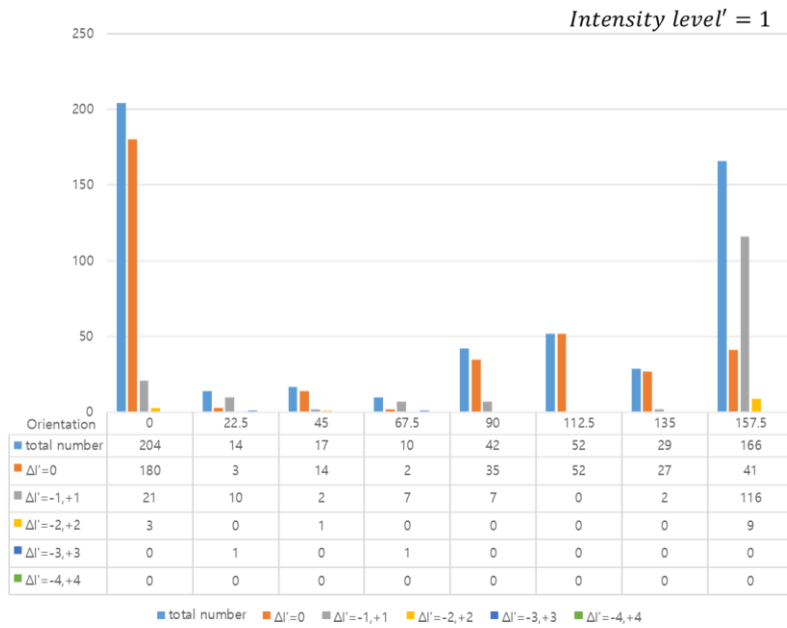


Figure 60. Histogram of retrieving results for each intensity level of intensity downgrade-decoding; 1, 2, 3, and 4

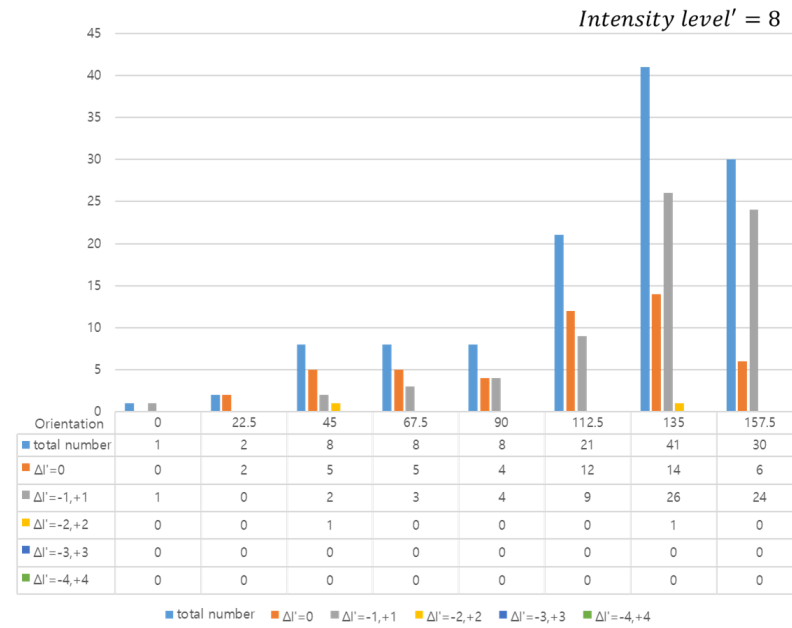
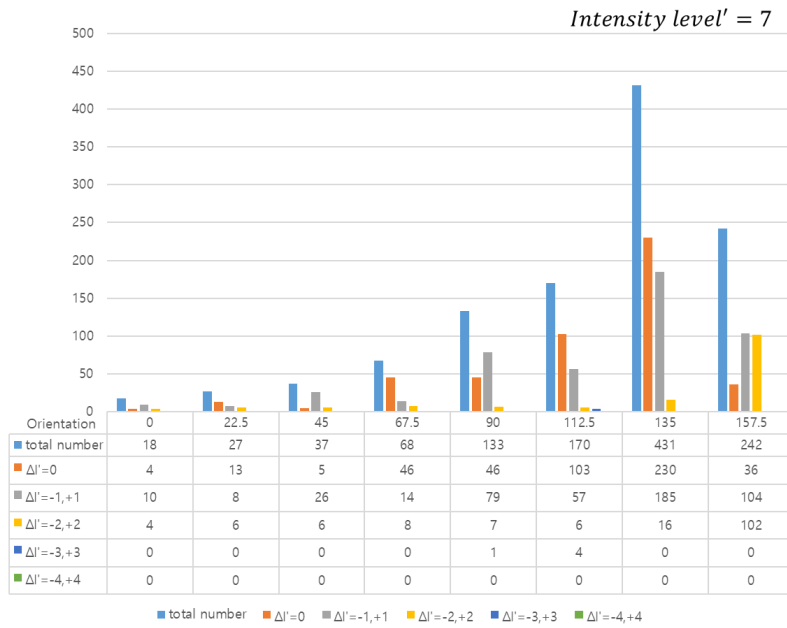
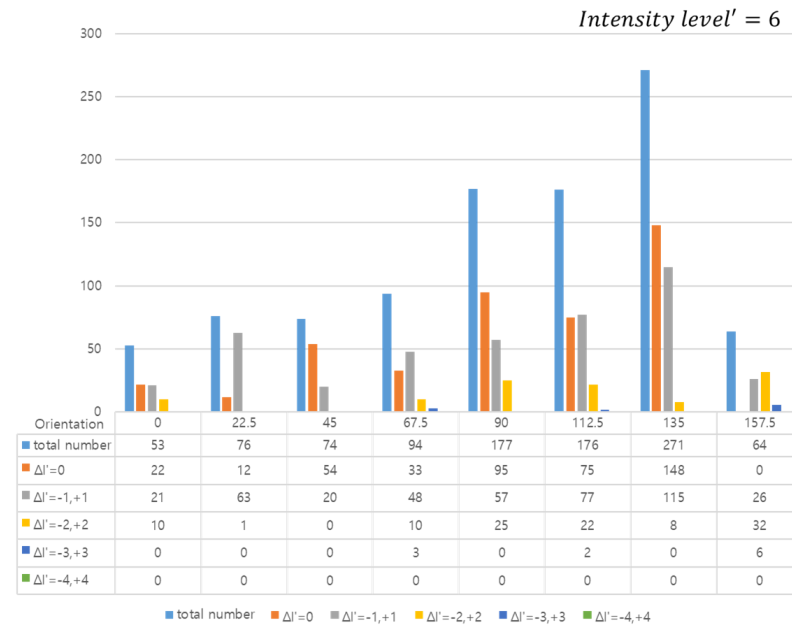
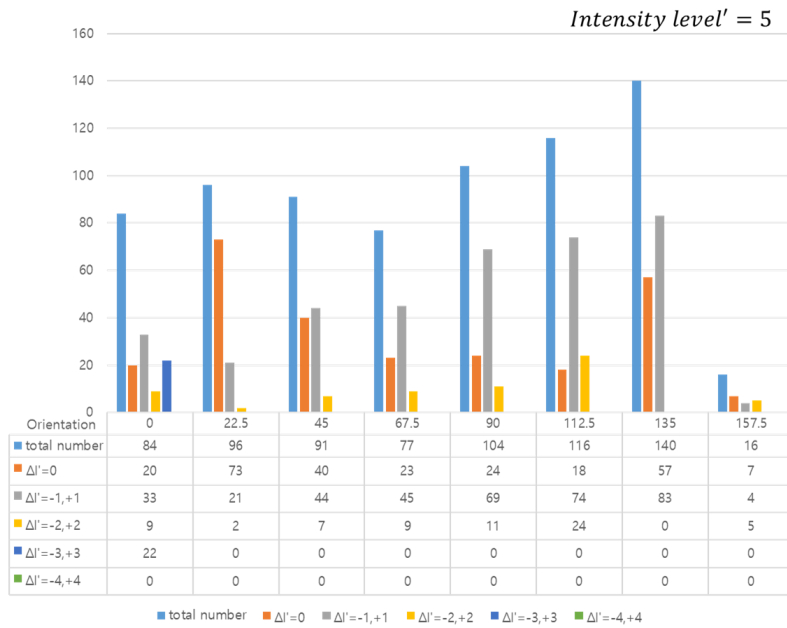


Figure 61. Histogram of retrieving results for each intensity level of intensity downgrade-decoding; 5, 6, 7, and 8

## 5. 7 Calculation for optical data storage density

The storage capacity of optical data storage was estimated by measuring the intensity profile of basic storage unit. Figure 62(a) is the fluorescence image measured by  $236 \times 236$  pixels for an area of  $7.6 \mu\text{m} \times 7.6 \mu\text{m}$ . Figure 62(b) and Figure 62(c) represent the intensity cross-section profiles of basic storage units along the y and x axes, respectively. From these two profiles, we can find that at least  $5 \mu\text{m} \times 5 \mu\text{m}$  space is required to prevent overlapping from adjacent patterns. Figure 62(d) shows an intensity profile measured at 500 nm intervals on the z axis near the tangential focal plane. The fluorescence intensity depth distribution has a Gaussian distribution and shows the strongest signal at the focal plane. To eliminate crosstalk completely, a  $20 \mu\text{m}$  gap is required between layers.

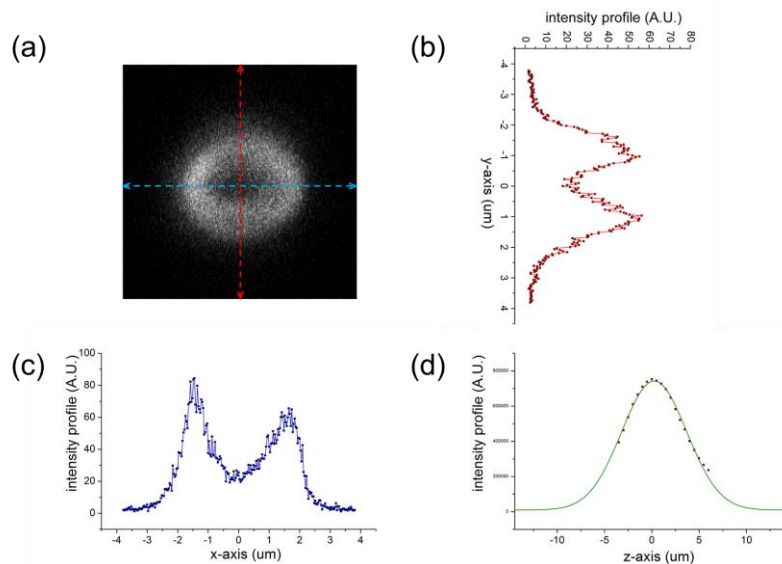


Figure 62. (a) An image of unit pattern fabricated by using type A DLW; (b) the profile of fluorescence intensity along the y-axis (short axis of ellipse); (c) the profile of fluorescence intensity along the x-axis (long axis of ellipse); (d) the profile of fluorescence intensity and Gaussian fitting along the z-axis(depth) at  $z = 0$  focal plane

Figure 63 shows the experiment result Royon performed with a 40x, 0.75 NA objective lens in the same experimental setup. In his result, there is no crosstalk between layers, and the information is well kept [76]. In our case, a storage capacity of 8 bits (4 bits for intensity, 4 bits for orientation) can be fabricated in a volume of  $5\ \mu\text{m} \times 5\ \mu\text{m} \times 20\ \mu\text{m}$ . Thus, a storage density of  $14.9\ \text{Gb}/\text{cm}^3$  can be reasonably expected to be obtained in the current experimental conditions, while performing laser structuring with an air objective. Furthermore, while considering tighter-focusing conditions with oil microscope objectives ( $100\times$ ,  $\text{NA} = 1.3$ ) we have observed elsewhere symmetrical circular patterns with diameters of  $0.8\ \mu\text{m}$  and thicknesses of  $4\ \mu\text{m}$ . With a  $5\ \mu\text{m} \times 5\ \mu\text{m}$  dedicated surface for an individual encoding unit (without lateral reading overlap) and  $10\ \mu\text{m}$  gap in depth between two layers, one could even access a storage density of  $119.2\ \text{Gb}/\text{cm}^3$  while laser structuring with an oil objective. This higher OSD density still needs to be demonstrated with the proposed approach, especially by showing that the ability of anamorphic beam caustic shaping is still maintained at such tight focusing.

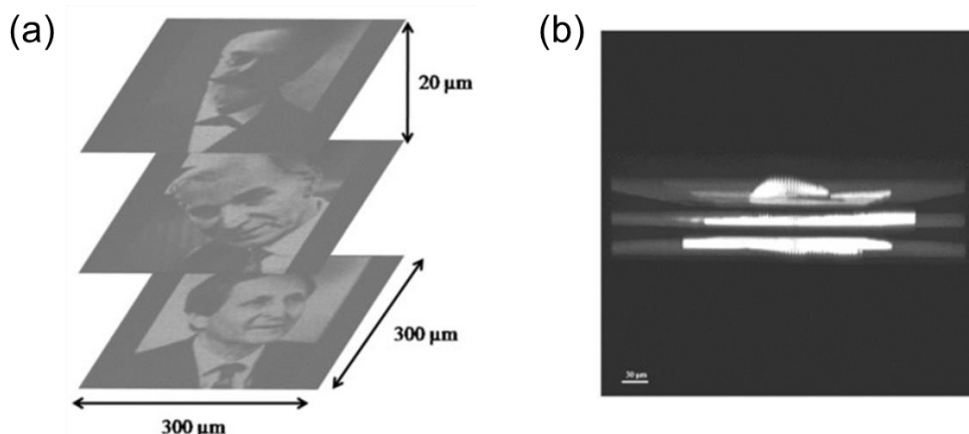


Figure 63. Royon's experimental data written at  $20\ \mu\text{m}$  intervals between layers to overcome crosstalk [76].

## 5. 8 Conclusion

We have demonstrated 5D optical data storage encoded in orientated type A DLW modifications in the silver containing Zinc-phosphate glass by using a relatively low laser irradiance (with very high number of pulses with sub-100 nJ pulse energies) compared to conventional DLW (with low number of pulses at the  $\mu\text{J}$  pulse energy level). Five dimensions were achieved by adding the orientation of ellipse pattern and fluorescence intensity to 3D position. The ellipse pattern was created by anamorphic focusing, and the orientation was adjusted to 16 levels by employing SLM. In addition, AOM device was used to adjust the femtosecond laser irradiance of 16 levels.

Two different images were embedded simultaneously on the same plane of silver containing glasses by type A DLW. In particular, a  $100\times 100$  pixel image in the format of 4-bit bitmap was used for 5D recording by employing 16 levels of ellipse orientation and 16 levels of laser irradiance. At the same time, a calibration matrix was fabricated separately nearby the DLW image to allow for the readout process. The two different original images of 4-bit bitmap format were successfully restored. The corresponding reading fidelities of 60.5% and 25.1% were obtained for the orientation direction and fluorescence intensity levels, respectively. In addition, it is shown that the reading accuracy can be greatly improved to 85.0% and 47.1% when 3-bit bitmap format was applied. The experimentally-obtained fidelity appears relevant for image storage and readout, but progress with respect to fidelity are still needed while considering hexadecimal information coding. Still, these results demonstrate the proof-of-concept of the proposed approach, which is 5-dimension multi-level optical data storage. Therefore, we believe that data storage densities up to 14.9

Gb/cm<sup>3</sup> (using a NA = 0.75 air objective) and up to 119.2 Gb/cm<sup>3</sup> (using a NA = 1.3 oil objective) can be achieved by using our proposed technique for the next-generation permanent recording.



## Chapter 6. Conclusion

This paper is a study of a new type of direct laser writing, so-called as type Argentum DLW, in silver containing zinc phosphate glasses by using femtosecond pulse laser. The characteristics of this new type DLW were studied, and it was confirmed that this technique can be utilized in one-dimensional, two-dimensional, three-dimensional, and five-dimensional.

When silver-containing zinc phosphate glasses are irradiated with femtosecond laser pulses, ring-shaped  $\text{Ag}_m^{x+}$  clusters are formed due to non-linear absorption. The fluorescence properties of the silver cluster induced by this type are different from those of the original glass, and the refractive index is also different. Although there is a difference depending on the composition ratio, when excitation using a 405nm laser, the induced cluster emits a fluorescence signal from 450nm to 650nm. And for the samples used in this experiment, the refractive index varies from  $2.7 \times 10^{-3}$  to  $5.1 \times 10^{-3}$  according to the injection irradiance.

The correlative description of laser-induced silver redistribution in terms of chemical micro-probe, NSOM and numerical modeling have been reported for the first time. The results significantly strengthen the understanding of material modifications in such glasses in a non-thermal interaction regime. In particular, it has been found that the spatial distribution of species in silver-containing glasses produced by femtosecond laser irradiation has a significant effect on chemical etching selectivity. This should help for future

development of nanoscale surface chemical patterning, such as for 2D photonics crystal applications.

The Y-shaped beam splitters, 2D structures made by using type A direct laser writing (DLW), was fabricated and its performance was measured. It was confirmed that a waveguide of a general shape in which the refractive index of the core is larger than that of cladding can be produced through type A DLW. Since the type A DLW always induces positive refractive index changes from  $2.7 \times 10^{-3}$  to  $5.1 \times 10^{-3}$ , it is very suitable for making waveguide. A symmetric Y-junction and various asymmetric Y-junctions were designed and fabricated using double line waveguides, and the output ratios were measured according to the transition of the inject position. It was confirmed that the output ratio could be from 96%-4% to 57%-43% due to the different irradiance in the process of writing between the upper branch and lower branch. So DLW in silver containing zinc phosphate glasses can be utilized easily and quickly to fabricate the desired type of optical device with only the writing process.

Finally, by researching 5D optical data storage using type A DLW, the scope of application was further expanded. We have demonstrated 5D optical data storage encoded in orientated type A DLW modifications by using a relatively low laser irradiance (with very high number of pulses with sub-100 nJ pulse energies) compared to conventional DLW (with low number of pulses at the  $\mu\text{J}$  pulse energy level). Five dimensions were achieved by adding the orientation of ellipse pattern and fluorescence intensity to 3D position. The ellipse pattern was created by anamorphic focusing, and the orientation was adjusted to 16 levels by employing SLM. In addition, AOM device was used to adjust the femtosecond laser irradiance of 16 levels.

Two different images were embedded simultaneously on the same plane of silver containing glasses by type A DLW. In particular, a 100×100 pixel image in the format of 4-bit bitmap was used for 5D recording by employing 16 levels of ellipse orientation and 16 levels of laser irradiance. At the same time, a calibration matrix was fabricated separately nearby the DLW image to allow for the readout process. The two different original images of 4-bit bitmap format were successfully restored. The corresponding reading fidelities of 60.5% and 25.1% were obtained for the orientation direction and fluorescence intensity levels, respectively. In addition, it is shown that the reading accuracy can be greatly improved to 85.0% and 47.1% when 3-bit bitmap format was applied. The experimentally-obtained fidelity appears relevant for image storage and readout, but progress with respect to fidelity are still needed while considering hexadecimal information coding. Still, these results demonstrate the proof-of-concept of the proposed approach, which is 5-dimension multi-level optical data storage. Therefore, we believe that data storage densities up to 14.9 Gb/cm<sup>3</sup> (using a NA = 0.75 air objective) and up to 119.2 Gb/cm<sup>3</sup> (using a NA = 1.3 oil objective) can be achieved by using our proposed technique for the next-generation permanent recording.

In conclusion, the fluorescence characteristics of type A DLW in silver containing zinc phosphate glasses were studied, and its utility as a multi-dimension application was confirmed. We believe this technology has great potential for nano-scale patterning in semiconductor and fabrication of micro-scale optical devices.



## Bibliography

1. K. O. Hill, Y. Fujii, D. C. Johnson, and B. S. Kawasaki, "Photosensitivity in optical fiber waveguides: Application to reflection filter fabrication," *Appl. Phys. Lett.* **32**(10), 647–649 (1978).
2. K. M. Davis, K. Miura, N. Sugimoto, and K. Hirao, "Writing waveguides in glass with a femtosecond laser," *Opt. Lett.* **21**(21), 1729 (1996).
3. C. B. Schaffer, A. Brodeur, and E. Mazur, "Laser-induced breakdown and damage in bulk transparent materials induced by tightly focused femtosecond laser pulses," *Meas. Sci. Technol.* **12**(11), 1784–1794 (2001).
4. B. C. Stuart, M. D. Feit, S. Herman, A. M. Rubenchik, B. W. Shore, and M. D. Perry, "Nanosecond-to-femtosecond laser-induced breakdown in dielectrics," *Phys. Rev. B* **53**(4), 1749–1761 (1996).
5. M. T. Gale, "Fabrication of continuous-relief micro-optical elements by direct laser writing in photoresists," *Opt. Eng.* **33**(11), 3556 (1994).
6. T. Gissibl, S. Thiele, A. Herkommer, and H. Giessen, "Two-photon direct laser writing of ultracompact multi-lens objectives," *Nat. Photonics* **10**(8), 554–560 (2016).
7. N. Tsutsumi, J. Hirota, K. Kinashi, and W. Sakai, "Direct laser writing for micro-optical devices using a negative photoresist," *Opt. Express* **25**(25), 31539 (2017).
8. M. Nawrot, Ł. Zinkiewicz, B. Włodarczyk, and P. Wasylczyk, "Transmission phase gratings fabricated with direct laser writing as color filters in the visible," *Opt. Express* **21**(26), 31919 (2013).
9. H. Wei and S. Krishnaswamy, "Direct Laser Writing Polymer Micro-Resonators for Refractive Index Sensors," *IEEE Photonics Technol. Lett.* **28**(24), 2819–2822 (2016).
10. W. Gao, N. Singh, L. Song, Z. Liu, A. L. M. Reddy, L. Ci, R. Vajtai, Q. Zhang, B. Wei, and P. M. Ajayan, "Direct laser writing of micro-supercapacitors on hydrated graphite oxide films," *Nat. Nanotechnol.* **6**(8), 496–500 (2011).
11. G. Viskadourous, D. Konios, E. Kymakis, and E. Stratakis, "Direct laser writing of flexible graphene field emitters," *Appl. Phys. Lett.* **105**(20), (2014).
12. M. F. El-Kady and R. B. Kaner, "Direct Laser Writing of Graphene Electronics," *ACS Nano* **8**(9), 8725–8729 (2014).
13. S. Luo, P. T. Hoang, and T. Liu, "Direct laser writing for creating porous graphitic structures and their use for flexible and highly sensitive sensor and sensor

- arrays," *Carbon* N. Y. **96**, 522–531 (2016).
14. R. Kumar, R. Savu, E. Joanni, A. R. Vaz, M. A. Canesqui, R. K. Singh, R. A. Timm, L. T. Kubota, and S. A. Moshkalev, "Fabrication of interdigitated micro-supercapacitor devices by direct laser writing onto ultra-thin, flexible and free-standing graphite oxide films," *RSC Adv.* **6**(88), 84769–84776 (2016).
  15. E. Blasco, J. Müller, P. Müller, V. Trouillet, M. Schön, T. Scherer, C. Barner-Kowollik, and M. Wegener, "Fabrication of Conductive 3D Gold-Containing Microstructures via Direct Laser Writing," *Adv. Mater.* **28**(18), 3592–3595 (2016).
  16. J. Fischer, G. Von Freymann, and M. Wegener, "The materials challenge in diffraction-unlimited direct-laser-writing optical lithography," *Adv. Mater.* **22**(32), 3578–3582 (2010).
  17. B. Harke, P. Bianchini, F. Brandi, and A. Diaspro, "Photopolymerization inhibition dynamics for sub-diffraction direct laser writing lithography," *ChemPhysChem* **13**(6), 1429–1434 (2012).
  18. A. Žukauskas, I. Matulaitiene, D. Paipulas, G. Niaura, M. Malinauskas, and R. Gadonas, "Tuning the refractive index in 3D direct laser writing lithography: Towards GRIN microoptics," *Laser Photonics Rev.* **9**(6), 706–712 (2015).
  19. A. Selimis, V. Mironov, and M. Farsari, "Direct laser writing: Principles and materials for scaffold 3D printing," *Microelectron. Eng.* **132**, 83–89 (2015).
  20. T. Bückmann, N. Stenger, M. Kadic, J. Kaschke, A. Frölich, T. Kennerknecht, C. Eberl, M. Thiel, and M. Wegener, "Tailored 3D mechanical metamaterials made by dip-in direct-laser-writing optical lithography," *Adv. Mater.* **24**(20), 2710–2714 (2012).
  21. Y. Cao, Z. Gan, B. Jia, R. A. Evans, and M. Gu, "High-photosensitive resin for super-resolution direct-laser-writing based on photoinhibited polymerization," *Opt. Express* **19**(20), 19486 (2011).
  22. K. C. Phillips, H. H. Gandhi, E. Mazur, and S. K. Sundaram, "Ultrafast laser processing of materials: a review," *Adv. Opt. Photonics* **7**(4), 684 (2015).
  23. K. Sugioka, "Progress in ultrafast laser processing and future prospects," *Nanophotonics* **6**(2), 393–413 (2017).
  24. L. Jonušauskas, D. Gailevičius, L. Mikoliunaite, D. Sakalauskas, S. Šakirzanovas, S. Juodkazis, and M. Malinauskas, "Optically clear and resilient free-form  $\mu$ -optics 3D-printed via ultrafast laser lithography," *Materials (Basel)*. **10**(1), 1–18 (2017).
  25. M. Vaezi, H. Seitz, and S. Yang, "A review on 3D micro-additive manufacturing technologies," *Int. J. Adv. Manuf. Technol.* **67**(5–8), 1721–1754 (2013).
  26. S. Nolte, F. Schrepel, and F. Dausinger, *Ultrashort Pulse Laser Technology. Laser Sources and Applications* (2016).

27. J. Kupersztych and M. Raynaud, "Anomalous multiphoton photoelectric effect in ultrashort time scales," *Phys. Rev. Lett.* **95**(14), 1–4 (2005).
28. Y. Petit, S. Danto, T. Guérineau, A. A. Khalil, A. Le Camus, E. Fargin, G. Duchateau, J. Bérubé, R. Vallée, and Y. Messaddeq, "On the femtosecond laser-induced photochemistry in silver-containing oxide glasses : mechanisms , related optical and physico-chemical properties , and technological applications," *Adv. Opt. Technol.* **7**(5), 291–309 (2018).
29. S. M. Eaton, G. Cerullo, and R. Osellame, *Femtosecond Laser Micromachining* (2012), **123**.
30. N. Marquestaut, Y. Petit, A. Royon, P. Mounaix, T. Cardinal, and L. Canioni, "Three-Dimensional Silver Nanoparticle Formation Using Femtosecond Laser Irradiation in Phosphate Glasses: Analogy with Photography," *Adv. Funct. Mater.* **24**(37), 5824–5832 (2014).
31. R. Espiau De Lamaestre, H. Béa, H. Bernas, J. Belloni, and J. L. Marignier, "Irradiation-induced Ag nanocluster nucleation in silicate glasses: Analogy with photography," *Phys. Rev. B - Condens. Matter Mater. Phys.* **76**(20), 1–18 (2007).
32. J. Choi, M. Bellec, A. Royon, K. Bourhis, G. Papon, T. Cardinal, L. Canioni, and M. Richardson, "Three-dimensional direct femtosecond laser writing of second-order nonlinearities in glass," *Opt. Lett.* **37**(6), 1029 (2012).
33. M. Bellec, A. Royon, B. Bousquet, K. Bourhis, M. Treguer, T. Cardinal, M. Richardson, and L. Canioni, "Beat the diffraction limit in 3D direct laser writing in photosensitive glass," *Opt. Express* **17**(12), 10304 (2009).
34. A. Royon, Y. Petit, G. Papon, M. Richardson, and L. Canioni, "Femtosecond laser induced photochemistry in materials tailored with photosensitive agents," *Opt. Mater. Express* **1**(5), 866 (2011).
35. A. Royon, K. Bourhis, L. Béchou, T. Cardinal, L. Canioni, and Y. Deshayes, "Durability study of a fluorescent optical memory in glass studied by luminescence spectroscopy," *Microelectron. Reliab.* **53**(9–11), 1514–1518 (2013).
36. G. Papon, Y. Petit, N. Marquestaut, A. Royon, M. Dussauze, V. Rodriguez, T. Cardinal, and L. Canioni, "Fluorescence and second-harmonic generation correlative microscopy to probe space charge separation and silver cluster stabilization during direct laser writing in a tailored silver-containing glass," *Opt. Mater. Express* **3**(11), 1855 (2013).
37. K. Mishchik, Y. Petit, E. Brasselet, A. Royon, T. Cardinal, and L. Canioni, "Patterning linear and nonlinear optical properties of photosensitive glasses by femtosecond structured light," *Opt. Lett.* **40**(2), 201 (2015).
38. E. Smetanina, B. Chimier, Y. Petit, N. Varkentina, E. Fargin, L. Hirsch, T. Cardinal, L. Canioni, and G. Duchateau, "Modeling of cluster organization in metal-doped oxide glasses irradiated by a train of femtosecond laser pulses," *Phys. Rev. A*

- 93**(1), 1–15 (2016).
39. O. L. ANDERSON and D. A. STUART, "Calculation of Activation Energy of Ionic Conductivity in Silica Glasses by Classical Methods," *J. Am. Ceram. Soc.* **37**(12), 573–580 (1954).
  40. P. Atkins and J. de Paula, *Physical Chemistry for the Life Sciences* (W.H. Freeman & Company, 2011).
  41. A. Abou Khalil, J.-P. Bérubé, S. Danto, T. Cardinal, Y. Petit, L. Canioni, and R. Vallée, "Comparative study between the standard type I and the type A femtosecond laser induced refractive index change in silver containing glasses," *Opt. Mater. Express* **9**(6), 2640 (2019).
  42. M. Bellec, A. Royon, K. Bourhis, J. Choi, B. Bousquet, M. Treguer, T. Cardinal, J. J. Videau, M. Richardson, and L. Canioni, "3D Patterning At the Nanoscale of Fluorescent Emitters in Glass," *J. Phys. Chem. C* **114**(37), 15584–15588 (2010).
  43. A. Abou Khalil, J.-P. Bérubé, S. Danto, J.-C. Desmoulin, T. Cardinal, Y. Petit, R. Vallée, and L. Canioni, "Direct laser writing of a new type of waveguides in silver containing glasses," *Sci. Rep.* **7**(1), 11124 (2017).
  44. M. Malinauskas, A. Žukauskas, S. Hasegawa, Y. Hayasaki, V. Mizeikis, R. Buividas, and S. Juodkasis, "Ultrafast laser processing of materials: from science to industry," *Light Sci. Appl.* **5**(8), e16133 (2016).
  45. M. Shimizu, M. Sakakura, S. Kanehira, M. Nishi, Y. Shimotsuma, K. Hirao, and K. Miura, "Formation mechanism of element distribution in glass under femtosecond laser irradiation," *Opt. Lett.* **36**(11), 2161 (2011).
  46. T. T. Fernandez, M. Sakakura, S. M. Eaton, B. Sotillo, J. Siegel, J. Solis, Y. Shimotsuma, and K. Miura, "Bespoke photonic devices using ultrafast laser driven ion migration in glasses," *Prog. Mater. Sci.* **94**, 68–113 (2018).
  47. K. Bourhis, A. Royon, M. Bellec, J. Choi, A. Fargues, M. Treguer, J. J. Videau, D. Talaga, M. Richardson, T. Cardinal, and L. Canioni, "Femtosecond laser structuring and optical properties of a silver and zinc phosphate glass," *J. Non. Cryst. Solids* **356**(44–49), 2658–2665 (2010).
  48. H. Ahn, J. Kim, D.-K. Kim, E. Lee, D.-S. Shin, H. Doh, and S.-H. Park, "High-resolution temporal and spatial photoluminescence measurement of a multiple-quantum-well structure at room temperature," **7214**(February 2009), 721403-721403–8 (2009).
  49. K. Bourhis, A. Royon, G. Papon, M. Bellec, Y. Petit, L. Canioni, M. Dussauze, V. Rodriguez, L. Binet, D. Caurant, M. Treguer, J. J. Videau, and T. Cardinal, "Formation and thermo-assisted stabilization of luminescent silver clusters in photosensitive glasses," *Mater. Res. Bull.* **48**(4), 1637–1644 (2013).
  50. J. C. Desmoulin, Y. Petit, L. Canioni, M. Dussauze, M. Lahaye, H. M. Gonzalez, E.

- Brasselet, and T. Cardinal, "Femtosecond laser structuring of silver-containing glass: Silver redistribution, selective etching, and surface topology engineering," *J. Appl. Phys.* **118**(21), (2015).
51. N. Marquestaut, Y. Petit, A. Royon, P. Mounaix, T. Cardinal, and L. Canioni, "Three-Dimensional Silver Nanoparticle Formation Using Femtosecond Laser Irradiation in Phosphate Glasses: Analogy with Photography," *Adv. Funct. Mater.* **24**(37), 5824–5832 (2014).
  52. B. Da Costa Fernandes, M. Pfiffer, P. Cormont, and J. Neauport, "Understanding the effect of wet etching on damage resistance of surface scratches," *Sci. Rep.* **8**(1), 1–9 (2018).
  53. M. Dussauze, V. Rodriguez, A. Lipovskii, M. Petrov, C. Smith, K. Richardson, T. Cardinal, E. Fargin, and E. I. Kamitsos, "How does thermal poling affect the structure of soda-lime glass?," *J. Phys. Chem. C* **114**(29), 12754–12759 (2010).
  54. N. Varkentina, M. Dussauze, A. Royon, M. Ramme, Y. Petit, and L. Canioni, "High repetition rate femtosecond laser irradiation of fused silica studied by Raman spectroscopy," *Opt. Mater. Express* **6**(1), 79–90 (2016).
  55. N. Ganesh, W. Zhang, P. C. Mathias, E. Chow, J. A. N. T. Soares, V. Malyarchuk, A. D. Smith, and B. T. Cunningham, "Enhanced fluorescence emission from quantum dots on a photonic crystal surface," *Nat. Nanotechnol.* **2**(8), 515–520 (2007).
  56. A. M. Streltsov and N. F. Borrelli, "Study of femtosecond-laser-written waveguides in glasses," *J. Opt. Soc. Am. B* **19**(10), 2496 (2002).
  57. J. W. Chan, T. R. Huser, S. H. Risbud, and D. M. Krol, "Modification of the fused silica glass network associated with waveguide fabrication using femtosecond laser pulses," *Appl. Phys. A Mater. Sci. Process.* **76**(3), 367–372 (2003).
  58. D. J. Little, M. Ams, P. Dekker, G. D. Marshall, and M. J. Withford, "Mechanism of femtosecond-laser induced refractive index change in phosphate glass under a low repetition-rate regime," *J. Appl. Phys.* **108**(3), (2010).
  59. J. W. Chan, T. Huser, S. Risbud, and D. M. Krol, "Structural changes in fused silica after exposure to focused femtosecond laser pulses," *Opt. Lett.* **26**(21), 1726 (2001).
  60. C. B. Schaffer, J. F. García, and E. Mazur, "Bulk heating of transparent materials using a high-repetition-rate femtosecond laser," *Appl. Phys. A Mater. Sci. Process.* **76**(3), 351–354 (2003).
  61. V. Prajzler, R. Mastera, and J. Spirkova, "Large core three branch polymer power splitters," *Radioengineering* **24**(4), 885–891 (2015).
  62. N. Syafiqah Mohamed-Kassim, A. A. Ehsan, M. H. M. Yusoff, and M. K. Abd-Rahman, "Fabrication and simulation of multimode symmetrical and asymmetrical

- Y-junction optical power splitters," 2010 Int. Conf. Photonics, ICP2010 1–5 (2010).
63. E. Walker and P. M. Rentzepis, "A new dimension," *Nat. Photonics* **2**(7), 406–408 (2008).
  64. T. Watanabe, M. Shiozawa, E. Tatsu, S. Kimura, M. Umeda, T. Mine, Y. Shimotsuma, M. Sakakura, M. Nakabayashi, K. Miura, and K. Watanabe, "A driveless read system for permanently recorded data in fused silica," *Jpn. J. Appl. Phys.* **52**(9 PART3), (2013).
  65. M. Gu, X. Li, and Y. Cao, "Optical storage arrays: A perspective for future big data storage," *Light Sci. Appl.* **3**(March), (2014).
  66. J. H. Strickler and W. W. Webb, "Three-dimensional optical data storage in refractive media by two-photon point excitation," *Opt. Lett.* **16**(22), 1780 (1991).
  67. P. Zijlstra, J. W. M. Chon, and M. Gu, "Five-dimensional optical recording mediated by surface plasmons in gold nanorods," *Nature* **459**(7245), 410–413 (2009).
  68. M. Beresna, M. Gecevičius, P. G. Kazansky, T. Taylor, and A. V. Kavokin, "Exciton mediated self-organization in glass driven by ultrashort light pulses," *Appl. Phys. Lett.* **101**(5), (2012).
  69. J. Zhang, R. Drevinskas, A. Patel, M. Beresna, P. Kazansky, A. Cerkauskaite, M. Beresna, R. Drevinskas, A. Patel, J. Zhang, and M. Gecevičius, "Eternal 5D data storage by ultrafast laser writing in glass," *Laser-based Micro-and Nanoprocessing X, Int. Soc. Opt. Photonics* **9736**(2016), 97360U (2016).
  70. S. Alasfar, M. Ishikawa, Y. Kawata, C. Egami, O. Sugihara, N. Okamoto, M. Tsuchimori, and O. Watanabe, "Polarization-multiplexed optical memory with urethane–urea copolymers," *Appl. Opt.* **38**(29), 6201 (1999).
  71. X. Ouyang, Y. Xu, Z. Feng, W. Tang, Y. Cao, and X. Li, "Polychromatic and polarized multilevel optical data storage," *Nanoscale* **11**(5), 2447–2452 (2019).
  72. A. C. Pearson, S. Jamieson, M. R. Linford, B. M. Lunt, and R. C. Davis, "Oxidation of graphene "bow tie" nanofuses for permanent, write-once-read-many data storage devices," *Nanotechnology* **24**(13), (2013).
  73. A. H. N. Melo and M. A. Macêdo, "Permanent data storage in ZnO thin films by filamentary resistive switching," *PLoS One* **11**(12), 1–10 (2016).
  74. Shane M. Eaton, G. Cerullo, and R. Osellame, *Femtosecond Laser Micromachining* (2008), **111**.
  75. Y. Petit, C.-H. Park, J.-M. Mok, E. Smetanina, B. Chimier, G. Duchateau, T. Cardinal, L. Canioni, and S.-H. Park, "Ultrashort laser induced spatial redistribution of silver species and nano-patterning of etching selectivity in silver-containing glasses," *Opt. Express* **27**(10), 13675 (2019).

76. A. Royon, K. Bourhis, M. Bellec, G. Papon, B. Bousquet, Y. Deshayes, T. Cardinal, and L. Canioni, "Silver clusters embedded in glass as a perennial high capacity optical recording medium," *Adv. Mater.* **22**(46), 5282–5286 (2010).
77. J. A. Davis, H. M. Schley-seebold, and D. M. Cottrell, "Anamorphic optical systems using programmable spatial light modulators," *Appl. Opt.* **31**(29), 6185–6186 (1992).



## Résumé

Au cours des 30 dernières années, alors que la largeur d'impulsion des lasers a été réduite et que les lasers haute puissance ont été développés, des recherches sur l'interaction entre le photon et les matériaux utilisant des lasers femtosecondes ont été activement menées. La haute densité d'énergie des lasers pulsés femtosecondes permet des processus de photoionisation non linéaire de plusieurs manières selon. Cet article rapporte une étude d'une écriture laser directe de type Argentum dans des verres de phosphate de zinc contenant de l'argent en induisant une déformation d'absorption non linéaire d'impulsions laser femtoseconde. Lorsque des verres de phosphate de zinc contenant de l'argent sont irradiés avec des impulsions laser femtoseconde, des amas en forme d'anneau se forment en raison d'une absorption non linéaire. Les propriétés de fluorescence et l'indice de réfraction de l'amas d'argent induit par cette déformation sont différents de ceux du verre d'origine.

Des comparaisons simultanées de microsondes chimiques, de NSOM et de modélisation numérique ont été utilisées pour analyser la distribution des espèces d'argent induite par laser. Les résultats renforcent considérablement la compréhension des modifications matérielles de ces verres dans un régime d'interaction non thermique. En particulier, il a été constaté que la distribution spatiale des espèces dans des verres contenant de l'argent produits par irradiation laser femtoseconde a un effet significatif sur la sélectivité de la gravure chimique.

Les séparateurs de faisceau en forme de Y, des structures 2D fabriquées à l'aide de DLW de type A, ont été fabriqués et leurs performances ont été mesurées. Il a été confirmé qu'un guide d'onde de forme générale dans laquelle l'indice de réfraction du noyau est plus grand que celui du revêtement peut être produit par le biais d'un DLW de type A. Étant donné que le DLW de type A induit toujours des changements d'indice de réfraction positifs de  $2,7 \times 10^{-3}$  à  $5,1 \times 10^{-3}$ , il est très approprié pour fabriquer un guide d'onde. Une jonction Y symétrique et diverses jonctions Y asymétriques ont été conçues et fabriquées à l'aide de guides d'ondes à double ligne, et les rapports de sortie ont été mesurés en fonction de la transition de la position d'injection. Il a été confirmé que le ratio de sortie pourrait être de 96% -4% à 57% -43% en raison de l'irradiance différente dans le processus d'écriture entre la branche supérieure et la branche inférieure. Ainsi, les verres DLW en argent contenant du phosphate de zinc peuvent être utilisés facilement et rapidement pour fabriquer le type de dispositif optique souhaité avec uniquement le processus d'écriture.

Enfin, en recherchant le stockage optique de données 5D (ODS) à l'aide de DLW de type A, le champ d'application a été élargi. Nous avons démontré le stockage optique de données 5D encodé dans des modifications orientées DLW de type A en utilisant un rayonnement laser relativement faible par rapport au DLW conventionnel. Cinq dimensions ont été obtenues en ajoutant l'orientation du motif d'ellipse et l'intensité de fluorescence à la position 3D. Le motif d'ellipse a été créé par mise au point anamorphique, et l'orientation a été ajustée à 16 niveaux en utilisant SLM. De plus, un dispositif AOM a été utilisé pour régler l'irradiance laser femtoseconde de 16 niveaux.

Pour confirmer la possibilité du 5D ODS proposé, deux images différentes ont été simultanément intégrées dans une image par DLW de type A. Et les deux images originales différentes au format bitmap 4 bits ont été restaurées avec succès. Les fidélité de lecture correspondantes de 60,5% et 25,1% ont été obtenues pour la direction d'orientation et les niveaux d'intensité de fluorescence, respectivement. De plus, il est démontré que la précision de lecture peut être considérablement améliorée à 85,0% et 47,1% lorsque le format bitmap 3 bits a été appliqué. En utilisant la technologie proposée, nous avons atteint une densité de données maximale de  $14,9 \text{ Gb} / \text{cm}^3$ , et nous pensons que des densités de stockage de données allant jusqu'à  $119,2 \text{ Gb} / \text{cm}^3$  (en utilisant  $\text{NA} = 1,3$  cible pétrolière) peuvent être atteintes.

En conclusion, les caractéristiques de fluorescence du DLW de type A dans des verres de phosphate de zinc contenant de l'argent ont été étudiées et son utilité en tant qu'application multidimensionnelle a été confirmée. Nous pensons que cette technologie a un grand potentiel pour la structuration à l'échelle nanométrique dans les semi-conducteurs et la fabrication de dispositifs optiques à micro-échelle.



## 국 문 요 약 (Abstract in Korean)

### 극초단 고출력 레이저를 이용한 다차원 비선형 Direct Laser Writing 및 특성 평가 연구

지난 30년간 극초단 고출력 레이저가 개발되고 연구됨에 따라, femtosecond 펄스 레이저를 이용한 photon과 물질간의 상호작용에 대한 연구가 활발히 이루어지고 있다. 높은 에너지 밀도를 가지는 femtosecond 레이저 펄스는 물질의 특성에 따라 다양한 메커니즘으로 비선형 광이온화를 가능케한다. 이 논문은 femtosecond laser pulse를 은 이온을 함유한 황화 아연 유리에 조사함으로써, 비선형 흡수 변형을 유도하는 type A Direct Laser Writing (DLW)에 관한 특성 및 응용에 관한 연구를 보고한다.

이 샘플에 femtosecond laser pulse train을 조사하면, 비선형 흡수로 인한 은 이온의 재배치과정을 통해 ring의 형태를 가지는 cluster를 형성한다. 이렇게 형성된 cluster는 기존의 유리 샘플과는 다른 fluorescence 특성과 refractive index를 가지게 된다. Chemical micro probe, near-field scanning optical microscopy (NSOM), 수치 계산을 동시에 비교하여 은 이온들의 분포를 분석하였다. 이를 통해 유리 샘플과 같은 non-thermal interaction regime에서 물질의 변형에 대한 이해를 높일 수 있다. 특히 femtosecond laser로 유도된 은 이온 종의 공간적 분포가 Chemical etching selectivity에 미치는 영향 분석하였다.

Type A DLW을 통해 만들어진 2차원 구조물인 Y형태의 beam splitter를 제작하고, 그 성능을 측정하였다. 이러한 방법으로 만들어진 광도파관은 일반적인 형태의 광도파관이 가지는 core 물질의 refractive index가 cladding의 refractive index보다 높은 특징을 가진다. 조사되는 레이저 세기와 쓰기 속도에 따라 다르지만,  $2.7 \times 10^{-3}$  에서  $5.1 \times 10^{-3}$  의 positive refractive index 변화를 가지고, 이는

광도파관으로 활용하기에 적당하다. 대칭적 Y-junction, 비대칭적 Y-junction을 설계, 제작하고 그 성능을 비교하였다. Type A DLW은 레이저 beam이 focusing되는 voxel의 외곽부분에만 silver cluster를 남기기 때문에, 2차원 구조에서는 두 줄의 writing patter을 남긴다. 이렇게 만들어진 광도파관은 입사 coupling이 굉장히 크기 때문에 입사 위치에 따른 beam splitter의 output을 측정하였다. 각기 다른 레이저 세기로 upper branch와 lower branch를 만든 비대칭적 Y-junction은 57%-43%에서 96%-4%까지의 beam splitting 성능을 가진다. 이렇게 은 이온을 함유한 황화 아연 유리에 Direct Laser Writing방식으로 2차원 구조물을 제작하면 높은 구조적 자유도를 가지고 빠르게 제작할 수 있기 때문에, micro-size 광학부품을 제작하는데 유용하다.

2차원에서 확장하여, 5차원 광학적 정보 저장(5D Optical Data Storage; 5D ODS)에 대한 연구를 하여 type A DLW의 활용성을 더욱 높일 수 있음을 확인하였다. Type A DLW은 기존 다른 그룹의 5D ODS 연구에서 사용된 레이저 세기보다 낮은 레이저 세기를 활용할 수 있다는 강점을 가진다. 5차원은 기존의 공간적 3차원에 타원 패턴의 방향 그리고 형광 세기를 더해 주어 구현하였습니다. 타원 패턴은 symmetrical focusing이 아닌 anamorphic focusing을 하여 유도하였고, 방향은 Spatial Light Modulator (SLM)의 holographic mask를 회전시켜 16단계로 변화시켰다. 형광 세기는 Writing pattern을 제작할 때, Acousto-Optic Modulator (AOM)를 사용하여 레이저의 세기를 조절하여 16단계로 변화시켰다.

이렇게 제안된 5D ODS의 가능성을 확인하기 위해, 서로 다른 2개의 사진을 타원의 방향, 형광 세기로 나타낼 수 있도록 변환하고, 이를 하나의 writing 이미지가 동시에 내포하도록 제작하였다. 이렇게 제작된 이미지를 4-bit 형식으로 디코딩하여 원래의 정보를 다시 얻었다. 타원의 방향에 포함된 정보는 60.5%의 정확도, 형광 세기에 포함된 정보는 25.1%의 정확도로 복원되었다. 그리고 정확도를 높이기 위해 3-bit 형식으로 디코딩하였을 때는 각각 85.0%, 47.1%의 정확도로 복원되었다. Type A DLW을 이용한 5D ODS는 14.9 Gb/cm<sup>3</sup>의 최대 저장 밀도를 가지고,

좀 더 높은 Numerical Aperture를 가지는 Objective lens를 사용하면 최대 119.2 Gb/cm<sup>3</sup>까지 저장 밀도를 증가시킬 수 있다.

종합적으로 이 논문은 은 이온이 함유된 황화 아연 유리에 femtosecond laser pulse를 이용한 Direct Laser Writing의 특성을 연구하고, 다차원 응용에 대한 연구 결과를 보여준다. 우리는 이 기술이 반도체 분야에서 nano-size의 patterning, micro-size의 광학 부품 분야 등에 폭 넓게 활용될 것이라 전망한다.

Key words: 레이저 직접 가공, 펨토세컨드 레이저, A 유형 DLW, 광도파관, 5차원 광학 저장 장치, 레이저 패터닝, 레이저 리소그래피